Search for Charged Strangelets in Pb–Pb Collisions at $158 \cdot A$ GeV/c

Inauguraldissertation
der Philosophisch-naturwissenschaftlichen Fakultät
der Universität Bern

vorgelegt von
Reiner Klingenberg
von der Bundesrepublik Deutschland

Leiter der Arbeit: Prof. Dr. K. Pretzl
Laboratorium für Hochenergiephysik

Search for Charged Strangelets in $\mathrm{Pb}-\mathrm{Pb}$ Collisions at $158 \cdot A\,\mathrm{GeV}/c$

Inauguraldissertation
der Philosophisch-naturwissenschaftlichen Fakultät
der Universität Bern

vorgelegt von
Reiner Klingenberg
von der Bundesrepublik Deutschland

Leiter der Arbeit: Prof. Dr. K. Pretzl

Laboratorium für Hochenergiephysik

Von der Philosophisch-naturwissenschaftlichen Fakultät angenommen

Bern, den 21. März 1996 Der Dekan

Prof. Dr. Hp. Pfander

Abstract

Results of Pb − Pb collisions at $p_{\text{lab}} = 158 \cdot A\,\text{GeV}/c$ are presented. Data was taken during the lead beam period 1994 at CERN by the NA52 collaboration (NEWMASS). It uses the secondary beam line H6 of the SPS as a focusing spectrometer, which is equipped with time of flight counters, multiwire proportional chambers, Čerenkov counters and a calorimeter to identify secondary particles.

At magnetic rigidities $p/Z = \pm 100$ and $\pm 200\,\text{GeV}/c$ about 10^{11} interactions were investigated in respect to a new particle search (*Strangelets*).

None of the registered and reconstructed events gives any convincing hint for the production of charged, heavy particles in the mass range up to $120\,\text{GeV}/c^2$ and life times of at least $1.2\,\mu$s. An upper limit of

$$10^{-7}\,\frac{\text{barn}}{\text{GeV}^2}c^3$$

for the differential production cross section at zero degree production angle at both polarities can be drawn.

Es werden Resultate über die Teilchenproduktion in Pb − Pb-Ionenwechselwirkungen bei $p_{\text{lab}} = 158 \cdot A\,\text{GeV}/c$ vorgestellt. Diese basieren auf einer Datennahme während der Bleistrahlperiode 1994 am CERN im Rahmen des Experimentes NA52 (NEWMASS). Dieses benutzt die Sekundärstrahlführung H6 des SPS als fokussierendes Spektrometer, ergänzt um Szintillationszählern zur Flugzeitmessung, Vieldraht-Proportionalkammern, Čerenkov-Zählern und einem Kalorimeter zur Teilchenidentifizierung.

Bei magnetischen Rigiditäten $p/Z = \pm 100$ und $\pm 200\,\text{GeV}/c$ sind etwa je 10^{11} Wechselwirkungen in Hinblick auf die Produktion von bisher unbekannten Teilchen (*Strangelets*) untersucht worden.

In keinem der aufgezeichneten und rekonstruierten Ereignissen läßt sich ein überzeugender Hinweis für die Produktion von geladenen, schweren Teilchen im Massenbereich bis zu $120\,\text{GeV}/c^2$ und Lebensdauern oberhalb $1.2\,\mu$s finden. Als obere Schranke kann ein Wert kleiner als

$$10^{-7}\,\frac{\text{barn}}{\text{GeV}^2}c^3$$

für den differentiellen Produktionswirkungsquerschnitt bei einem Produktionswinkel von Null Grad bei beiden Polaritäten angegeben werden.

Contents

List of Figures

List of Tables

Introduction

The discovery of strangelets has long been advertised as an ultimate signature for the quark-gluon plasma (QGP) formation in ultrarelativistic heavy ion collisions. Strangelets could be formed from the QGP via a strangeness distillation process [Liu84, Greiner88, Greiner91]. Their discovery would have profound implications beyond the confirmation of the QGP formation: it would establish the existence of strange quark matter (SQM) [Witten84, Farhi84, Berger87] in nature, thus lending strong support to astrophysical and cosmological hypotheses on the role of SQM in the universe. If SQM were absolutely stable, it would represent a new, as yet unobserved ground state of matter.

Several experimental searches for strangelets in cosmic rays [Saito90] and for strangelet production in heavy ion collisions have been carried out at the AGS in Brookhaven, and are still ongoing at present using gold ions accelerated to 11.6 GeV/c per nucleon [Barrette90, Rotondo91, Crawford91, Rotondo95, Beavis95]. At CERN, where higher beam energies are available, a search with sulphur ions was completed in 1992 [Volken94, Borer94]. A recent review is given in ref. [Kumar95].

During the 1994 Pb-period at CERN, the NA52 collaboration took data to search for positively and negatively charged strangelets resulting from lead-on-lead collisions at an incident beam momentum of $158 \cdot A$ GeV/c. Preliminary results have been already presented [Dittus95].

This thesis describes the analysis and discusses the results achieved from the data sampled during the 1994 Pb-period.

Basic ideas about production models for strangelets and their hypothetical stability are discussed (chapter 1), before a description of the detector setup and some performance characteristics are presented in chapter 2. A simulation of the beam line acceptance and comparison with measurements is put forward in chapter 3. General data treatment and calibration of the electronic channels is described in chapter 4. An overview over the observed incident and secondary particle rates is given in chapter 5. Analysis and results concerning the strangelet search and production rates of antiprotons and antideuterons are discussed in chapters 6 and 7. Chapter 8 summarizes the results and gives a comparison to the predictions of a production model for strangelets.

Chapter 1

Physics motivation

Some ideas about the possible existence of strangelets are given. Their (meta)stability in the framework of the MIT bag model and possible decay modes and lifetime estimates are discussed. A production mechanism of strangelets in heavy ion collisions is presented, including a production probability estimate for a spectrometer experiment which can be compared to the achieved results of NA52.

1.1 Ideas about strangelets

Multiquark states or hadrons with large baryon numbers $A > 1$, which contain similar amounts of up, down and strange quarks are called droplets of strange quark matter or strangelets. Up to now these are only hypothetical states which can be predicted by theoretical considerations but which have not been observed doubtless in nature or in experiments.

The known particles which are found in nature or produced in collision experiments can be classified into leptons and hadrons according to the standard model of particle physics. All particles are subject to gravitational and electroweak interactions. The latter force is conveyed by photons and massive vector bosons $W^{\pm}$ and Z^0. According to the standard model the leptons and the vector bosons are regarded as elementary particles. In contrast to that, hadrons are composed objects consisting of quarks, which are subject to a further force, the strong interaction, which is conveyed by gluons. Quarks and gluons are carrying colour charges. The confinement character of the strong force prohibits the isolated existence of single quarks, but they can cluster in pairs or small groups, which have a net zero colour charge. The only known quark ensembles are mesons and baryons. The former consists of a quark-antiquark pair, while the latter are composed of three quarks. Groups with a larger number of quarks are not known, but clusters of baryons like nuclei are well established in nature. There is no physical principle known which excludes the existence of larger baryons. These hypothetical states are also called quark matter, since their elementary ingredients are the quarks themselves.

To answer the possible existence of quark matter one has to investigate their stability against radioactive decays. With simple arguments involving the Pauli exclusion principle, the stability of quark matter states may be achieved by introducing the strange quark: usually one is speaking of strange quark matter. Strangelets themselves are regarded as droplets of strange quark matter. Their possible masses may lie between the masses of light nuclei $A > 1$ and neutron stars $A \approx 10^{57}$.

First ideas about the existence of such states of matter were published by A. Bodmer in 1971 under the title "Collapsed Nuclei" [Bodmer71]. According to those ideas collapsed nuclei have a higher density than ordinary nuclei and may have also a lower energy level. The spontaneous decay of nuclei into these collapsed states is inhibited by a saturation barrier which prolongs their lifetimes to more than 10^{31} sec. This corresponds to about 10^{14} times the age of the universe. Furthermore, it is presumed that such collapsed states have been created in the initial extremely hot and dense stages of the universe and part of them may still exist in certain regions.

Considerations about the creation of quark matter during the expansion of the early universe have later been picked up by E. Witten [Witten84]. According to that scenario a first order phase transition from deconfined quarks and gluons to confined hadrons allows the creation of bubbles of low temperature in coexistence with the hot phase. In the course of the expansion the bubbles are enlarged and clustered and only small regions of high temperature are remaining. They consist of a large fraction of the baryonic matter in states of quark matter.

Another cosmological production scheme can be found in conjunction with neutron stars, objects which are bound by gravitational forces. Under larger pressure nuclear matter may be converted to a two flavour quark matter which gets a higher stability through the reaction ud $\rightleftharpoons$ us in strange quark matter. A Coulomb barrier free absorption of neutrons can even enlarge the regions of quark matter [Witten84].

Quark matter in the context of cosmology is one candidate for dark matter. The existence of quark matter in cosmic rays is one interpretation of "Centauro" events. In these the collision of primary cosmic particles with the atmosphere leads to fragments of hundreds of baryons, which is an expected fate of a colliding droplet of quark matter [Bjorken79].

1.2 Stability and decay of strangelets

As a basic argument for the possible stability of strange quark matter the Pauli exclusion principle for fermions is used. In a two flavour state consisting of many quarks the introduction of a third degree of freedom "strangeness" allows a lowering of its Fermi level (*cf.* Fig. 1.1). Typical Fermi levels of quark states with nuclear density are 300 to $350\,\mathrm{MeV}/c^2$, while the mass of the strange quark with about 100 to $300\,\mathrm{MeV}/c^2$ may be lower. A similar argument does not hold for the forth flavour, since its mass with 1.0 to $1.6\,\mathrm{GeV}/c^2$ is too high to postulate "charmlets". Furthermore one should remember that addition of strangeness does not help to stabilize nuclear matter because hyperons are heavier than nonstrange baryons.

A striking consequence of the introduction of strange quarks in systems compared to nuclear matter is their relative low charge to mass ratio. Usually one parameterizes the charge to baryon number ratio for systems with equal numbers of up and down quarks as

$$\frac{Z}{A} = \frac{1 - f_s}{2} \tag{1.1}$$

where f_s is the number of strange quarks per baryon. With an increase of the strange quark fraction strangelets become neutral or even negatively charged.

Quantitative answers about the stability of strange quark matter are discussed for example in the framework of the MIT bag model, which describes hadronic states as a Fermi gas of quarks which are bound in a potential (*i. e.* the bag). Parameters of this model are

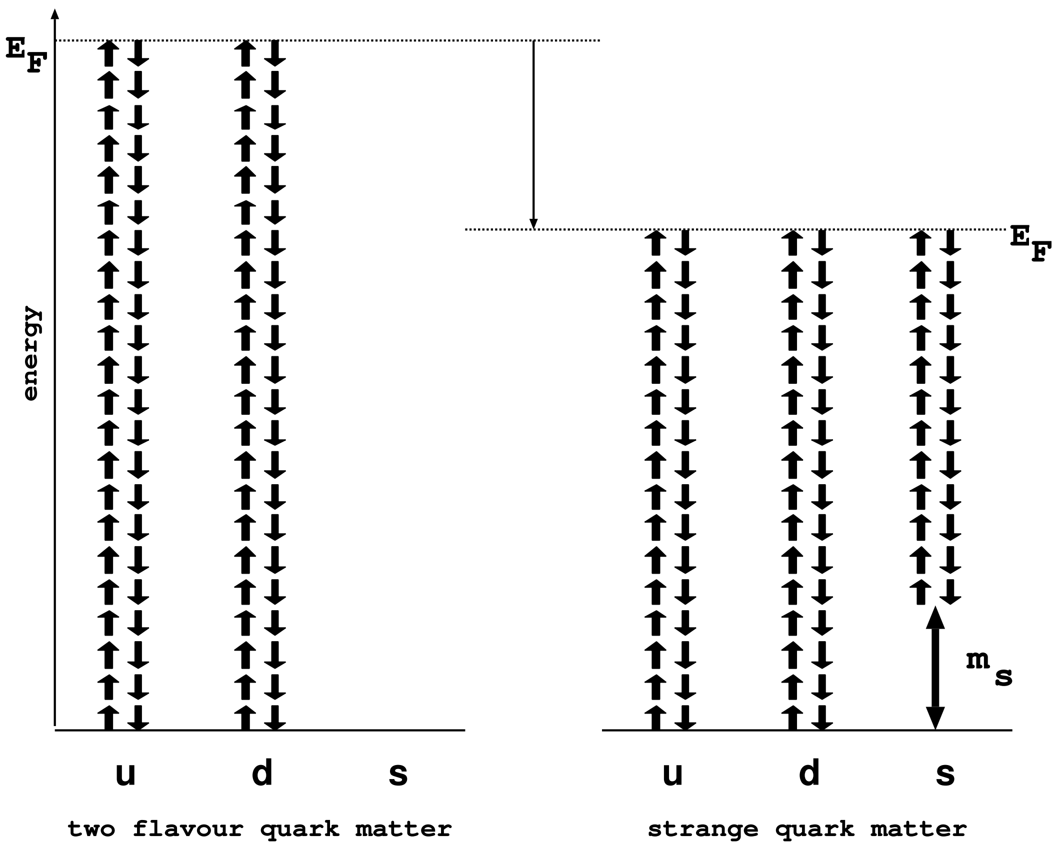

Figure 1.1: It is conceivable that the Fermi energy of strange quark matter is lower than that of a two flavour system.

- α_c, the coupling of the strong interaction between the quarks,
- m_s, the mass of the strange quark, while the masses of up and down quarks are usually neglected,
- B, the bag constant, which provides the confinement of the quarks within the potential.

The latter parameter can be interpreted as an external pressure onto the quarks. The MIT bag model has been applied for example for the description and parameterization of known hadrons [DeGrand75]. Masses, charge radii and magnetic moments can be well reproduced with a unique set of parameters.

The critical value which can be calculated in the framework of such a model is the energy per baryon in a multiquark system, which decides about the decay into nucleons. The actual parameters for quark matter are unknown and thus one has got larger varieties in choosing values to achieve results about stability. But qualitative answers derived from the bag model suppose that it is more likely to have large stable quark systems than smaller ensembles, since in the latter ones destabilizing surface effects have to be taken into account. In contrast to that calculations show that shell structure effects may lead to a stabilization of small droplets [Gilson93]. Negatively charged strangelets are only assumed to be stable if the strange quark mass is rather low. The existence of stable negatively charged strangelets would have the apocalyptic characteristic to transform nuclear matter into quark matter by emission of energy since no Coulomb barrier hinders the absorption of positively charged matter.

Many authors have published calculations about quark matter systems using the MIT bag model with various parameters. Apart from a small parameter set which allows absolute stability of strange quark matter ($B^{1/4} \leq 150\,\mathrm{MeV}$, $m_s \leq 170\,\mathrm{MeV}$) in a larger region metastability is favoured within this model ($B^{1/4} \leq 190$, $m_s \leq 180\,\mathrm{MeV}$, *cf.* [Koch91]).

In one of the first approaches Chin and Kerman [Chin79] derived the result that strangelets might be metastable. They discussed possible decay modes and gave a first lifetime estimate. Later this approach was reconsidered by P. Koch [Koch91]. The relevant decay mode for metastable strangelets are the strangeness changing weak processes

$$\mathrm{s} \quad \rightarrow \quad \mathrm{u} + \mathrm{e}^- + \overline{\nu_\mathrm{e}} \tag{1.2}$$

and

$$\mathrm{s} + \mathrm{u} \quad \rightleftharpoons \quad \mathrm{d} + \mathrm{u} \tag{1.3}$$

with lifetimes $10^{-5} \ldots 10^{-4}$ sec. The key point to get life times which are longer than those of other weak processes is the Pauli blocking, *i. e.* the transition $\mathrm{s} \rightarrow \mathrm{u}$ is hindered in quark matter with occupied up quark states. A comprehensive discussion of radioactive decays of SQM can be found *e. g.* in [Berger87].

1.3 Production of strangelets in heavy ion collisions

A possible experimental environment to produce multiquark states in the laboratory are relativistic collisions of heavy ions.

1.3.1 Phases of matter and the quark-gluon plasma

In heavy ion collisions one wants to create a hot and dense phase of the strongly interacting quarks and gluons, the quark-gluon plasma. It is believed that such a phase of matter was existing in the early universe (*cf.* [Witten84]), before in later steps of hadronization and nucleosynthesis finally nuclear matter could be created. Fig. 1.2 displays the historical evolution of the universe.

The phases of matter and their conditions of existence are described by the nuclear equation of state, which one wants to derive from the experimental investigations. The commonly believed scenario for nuclear matter is rendered as a phase diagram in Fig. 1.3.

Besides the nuclear matter, corresponding to a liquid phase, one hopes to reach the quark-gluon plasma by increasing density and temperature. Strangelets have got comparable densities like a quark-gluon plasma, but are existing at low temperatures with strangeness as stabilizing degree of freedom.

1.3.2 Creation of strangelets via a quark-gluon plasma

A possible creation for strangelets as remnants of a cooled QGP is described via a strangeness distillation process [Liu84, Greiner88, Greiner91].

Figure 1.2: Temperature of the universe has been falling since the big bang. During the first microsecond, all matter is thought to have existed as quark-gluon plasma [Gutbrod91].

Figure 1.3: Picture of different phases of hadronic matter [Gutbrod91].

A large amount of gluons and $q\bar{q}$ pairs including $s\bar{s}$ pairs are created during the heavy ion collision. The high density of quarks and gluons allows to create the deconfined phase (QGP). It might favour a further creation of $s\bar{s}$ pairs via quark pair annihilation $q\bar{q} \rightarrow s\bar{s}$ and gluon fusion $gg \rightarrow s\bar{s}$. The net strangeness of the whole system is always kept at zero. But the initial abundance of up and down quarks allows a preferred confinement of antistrange quarks to kaons ($K^+(u\bar{s})$, $K^0(d\bar{s})$). Thus, a separation of strangeness remaining in the QGP and antistrangeness in a hadron phase takes place. In addition, rapid kaon emission leads to a finite net strangeness of the expanding hadron and quark system. The emission of pions and kaons cools the quark phase, which condenses into (meta)stable droplets of strange quark matter. In this sense strangelets can be regarded as remnants of a cooled QGP and are therefore a signature for the creation of the deconfined phase.

Figure 1.4: Creation of strangelets via a quark-gluon plasma.
(a) Evaporation of K^+ and K^0 carries antistrangeness away and cools the QGP .
(b) A hadron gas phase (HG) surrounds the quark-gluon plasma.
(c) Either a (meta)stable strangelet or nucleons and hyperons, remain.

1.3.3 Coalescence picture for the strangelet production

It should be noted that also alternative production mechanisms for strangelets can come into question.

Baltz *et al.* describe *e. g.* a strange cluster formation in relativistic heavy ion collisions [Baltz95]. They are using a coalescence picture for the creation of hypernuclei in heavy ion collisions. In a further step these hypernuclei might decay into more stable strangelet states.

1.4 Quantitative predictions for the production probability

Crawford *et al.* use the calculations of Liu and Shaw [Liu84] to derive absolute production probabilities for strangelets via a quark-gluon plasma in heavy ion collisions [Crawford92, Crawford93]. Basically the production probability is factorized in four independent steps:

- the formation of a quark-gluon drop itself;
- its fragmentation into smaller droplets, accompanied with the kaon emission;
- the building up of a drop with a certain mass and charge, which are the characteristic observables in heavy ion experiments for particle identification;
- the cooling of an excited strangelet to its ground state.

Incorporated in these calculations are results of measurements of strangeness production measured in heavy ion experiments. For Pb−Pb interactions at the SPS accelerator of CERN with a center of mass energy of $\sqrt{s} = 17 \cdot A\,\mathrm{GeV}$ the production probabilities for various baryon and charge numbers are given [Crawford93]. In Fig. 1.5 the values for strangelets with mean lifetimes larger than $2 \cdot 10^{-7}$ sec and baryonic numbers 20, 30 and 40 are displayed.[1]

According to these calculations it is most likely to produce light, positively charged strangelets.

1.5 Experimental consequences

According to the quantitative prediction for the production probability of strangelets in Pb−Pb collisions at the CERN-SPS one needs an experimental environment to detect a rare particle species with a sensitivity of 10^{-9} or better. In a focusing spectrometer setup with a limited phase space acceptance one has to investigate a multiple of 10^9 interactions. Assuming that the strangelets are produced preferentially with low mean transverse momentum and near midrapidity, *i. e.* the center of mass rapidity of the colliding nuclei, one has to investigate particle spectra near zero degree production angle of secondary particle momenta

$$p = m \cdot c \cdot \sinh y_{\mathrm{cm}} \approx 9 \cdot m \cdot c \qquad (y_{\mathrm{cm}} = 2.9) \tag{1.4}$$

by choosing beam line rigidities $p/|Z|$ between 50 and $200\,\mathrm{GeV}/c$ to be able to detect particles with a characteristic high mass to charge range of 5 to $20\,\mathrm{GeV}/c^2$. Particle identification capabilities are necessary to measure the characteristic m/Z ratio.

[1]The authors are discussing two different surface contributions. Here, only the numbers resulting from the lower surface contribution leading to higher production probabilities are reprinted.

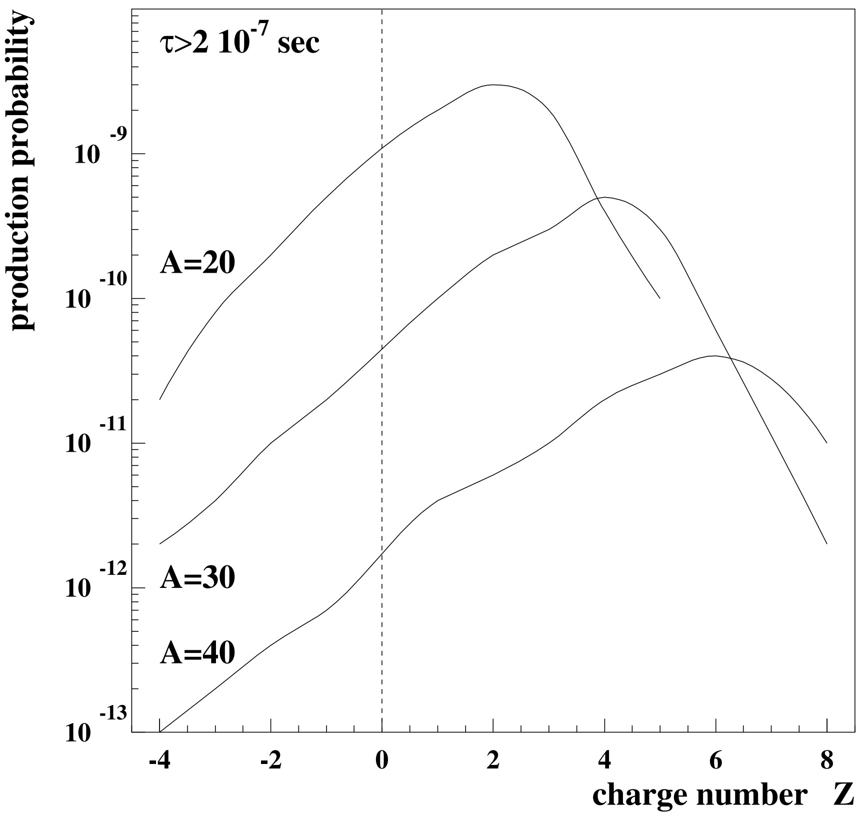

Figure 1.5: Prediction of production probabilities for strangelets according to Crawford *et al.* in Pb−Pb interactions at $\sqrt{s} = 17{\cdot}A\,\mathrm{GeV}$ [Crawford93].

Once, strangelet candidates have been established one needs a second generation of experiments in order to exploit the quantum numbers of the new states, *e. g.* by measuring the strangeness contents via secondary interactions. Liu and Shaw suggested the characteristic decay into hyperons to prove the strangeness character [Liu84].

Chapter 2

Experimental method

The goal of the NA52 experiment is to identify strangelet candidates by means of their proposed low charge to mass ratio. In this chapter the experimental setup and the particle identification possibilities of the individual detector components are described.

2.1 Overview

The NA52 apparatus (Fig. 2.1) makes use of the existing H6 beam line at CERN. It is a single particle, double-bend focusing spectrometer transmitting charged particles within a momentum bite of 2.8% selectable for rigidities $p/|Z|$ between 5 and 200 GeV/c. It is operated at a production angle of 0^o and has a solid angle acceptance of 2.2 μsr.

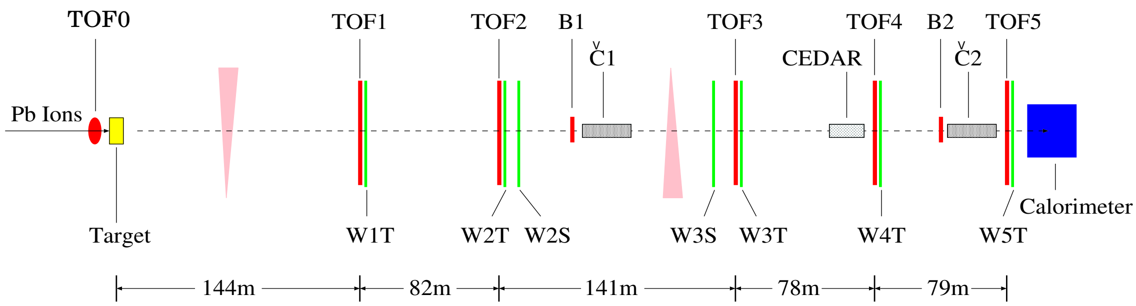

Figure 2.1: The NA52 setup. The upstream part of the detector includes particle tracks until TOF3 ($t_{\rm lab} \gtrsim 1.2\,\mu$s), the downstream trigger until TOF5 ($t_{\rm lab} \gtrsim 1.7\,\mu$s).

Particles are identified by their mass and charge, which are determined with the help of time of flight and energy loss measurements in eightfold segmented scintillator hodoscopes. Five such hodoscopes (TOF1-5) are placed at different positions along the beam line and have a time resolution of about 100 ps. Multiwire proportional chambers (W1T-W5T,W2S,W3S) are used to track particles through the beam line. They are used to identify multiparticle events and allow a phase space reconstruction of the produced and transported secondaries.

The read-out of the detector is subdivided into two parts with individual triggers and data acquisition systems. Each trigger consists of the coincidence between an unsegmented scintillator counter and a TOF hodoscope (B1·TOF2, B2·TOF4). Threshold Čerenkov counters (Č1,Č2) are used to veto and/or tag light particles. The upstream part of the detector (up to TOF3, *cf.* Fig. 2.1) requires a life time $t_{\rm lab} \gtrsim 1.2\,\mu$s for a particle to be detected, inclusion of the downstream trigger up to TOF5 increases this limit to about $1.7\,\mu$s. For particle species with short mean life time a corresponding fraction $\exp(-t_{\rm lab}/\tau\gamma)$ is registered by the triggers.

A differential Čerenkov counter (CEDAR) and a segmented hadron calorimeter add further particle identification capabilities and redundancy to the measurement.

Incident lead ions are detected just in front of the lead target with a 0.4 mm thick, fourfold segmented quartz Čerenkov counter. It allows to count the number of incident projectiles and provides precise timing information in the TOF measurement.

2.2 Ion source and acceleration at CERN

An electron cyclotron resonance source produces the lead ions [Hasenroth95]: Lead gas is ionized by the aid of electrons from an incandescent electrode sited in the centre of a cyclotron. It provides $^{208}\mathrm{Pb}^{27+}$ at $2.5 \cdot A$ keV. A RFQ accelerates these ions to $250 \cdot A$ keV and a linac to $4.2 \cdot A$ MeV. A stripper increases the ionization state to 53+ before the ions are further accelerated in the PS booster and Proton Synchrotron (PS) to $4.25 \cdot A$ GeV [Blas95]. A second stripper (0.5 mm Al) removes the remaining electrons and the Super Proton Synchrotron (SPS) accelerates $^{208}\mathrm{Pb}^{82+}$ to $160 \cdot A$ GeV or $400 \cdot Z$ GeV [Faugier95]. The ions are extracted over a 5 sec long spill to different experiments. The acceleration and extraction cycle is repeated with a period of 19.2 sec.

The acceleration mechanism (*e. g.* the revolution time of $5\,\mu$s in the Proton Synchrotron) introduces a time structure of the extracted lead ions. A parameterization of the actual measured spill structure at the target T4 is summarized in section 5.1. About $5 \cdot 10^7$ ions were available per cycle in 1994, when for the first time the lead beam was delivered at CERN.

2.3 Target area and beam line

The NA52 experiment uses the lead ions steered to the target station T4, located at the North Area of the Super Proton Synchrotron.

Central part of the NA52 detector is the H6 beam line. It is a single particle, focusing spectrometer transporting secondary particles from the target, which is located in front of the H6 beam line, over a distance of up to 540 m down to the hadron calorimeter. Magnetic rigidities are selectable between 5 and 200 GeV/c within a momentum bite of $\frac{\Delta p}{p} \equiv \delta = 2.8\%$ accepting particles in a solid angle of $2.5\,\mathrm{mrad} \times 0.9\,\mathrm{mrad} = 2.2\,\mu\mathrm{sr}$. A detailed description of the beam optics, simulation of the beam line acceptance and a tentative comparison to measurements is presented in chapter 3, p. 29. As a result the combined solid angle and momentum acceptance of the beam line is $\Delta\Omega\delta = 4\,\mu\mathrm{sr}\%$ valid at high momenta $p_{\rm lab} \geq 100\,\mathrm{GeV}/c$.

Standard equipment of the target area, usually used for experiments with incident protons consists of a target box housing, a remotely controlled target ladder with various beryllium and copper targets. The incident particle flux is measured with the help of secondary emission chambers.

For the investigations of the Pb−Pb collisions this target area has been extended. The target box itself provides the possibility to choose a 40 mm lead target. In front of this a quartz Čerenkov counter, an additional target ladder with lead targets between 0.5 and 16 mm thickness, and a fourfold scintillation counter to measure particle multiplicities have been installed. A schematic drawing of this arrangement is shown in Fig. 2.2.

Figure 2.2: Schematic drawing of the target area: incident lead ions are registered by the help of a fourfold segmented quartz Čerenkov counter before they might undergo an interaction in one of the choosable thin targets (0, 0.5, 2 4 or 16 mm thickness) on the target ladder or in the thick target of 40 mm.

For the strangelet search only the targets of 16 and 40 mm thickness were chosen and the information from the interaction counter was ignored in the analysis.

2.4 Quartz Čerenkov counter

The quartz Čerenkov counter is segmented into four quadrants. It has got a thickness of 0.4 mm and a diameter of 13 mm, and registers the incident lead ions via the Čerenkov effect. The fully ionized lead ions ($Z = 82$), while passing through the counter, polarize the surrounding atoms in the quartz material and they radiate light. From each segment the produced Čerenkov light is guided through quartz fibers to XP2020Q photomultipliers. Their amplified signals are transfered with the aid of an optical transmission system over a distance of about 300 m to optical receivers and the read-out electronics. Some more technical details of this optical link are described in section 2.4.1. The achieved double pulse resolution of about 7 ns of the combined link "photomultiplier - amplifier - optical transmission - optical receiver" is used to determine the systematic miscounting of incident lead ions. The corresponding simulation based on the measured spill structure and intensity is discussed in section 5.1, p. 57.

2.4.1 Optical link

The schematic drawing of the optical link is shown in Fig. 2.3.

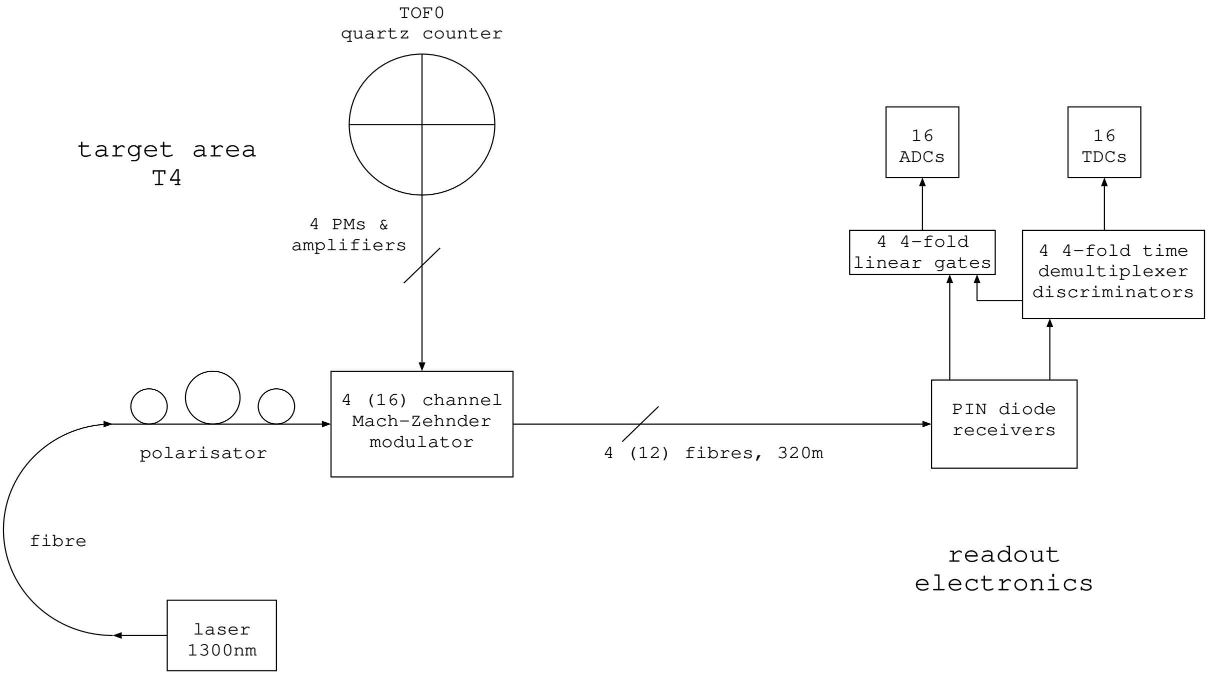

Figure 2.3: Optical link between the target and the experimental area.

It transmits the four analog signals of the quartz Čerenkov counter over a cable distance of 320 m to the read-out electronics.

The heart of the transmission is a multichannel Mach-Zehnder modulator. This device provides the amplitude modulation of monochromatic linear polarized light. Here, a laser with a wave length of 1.3 μm and 20 mW light power is used. Fig. 2.4 shows a schematic drawing of one modulation channel.

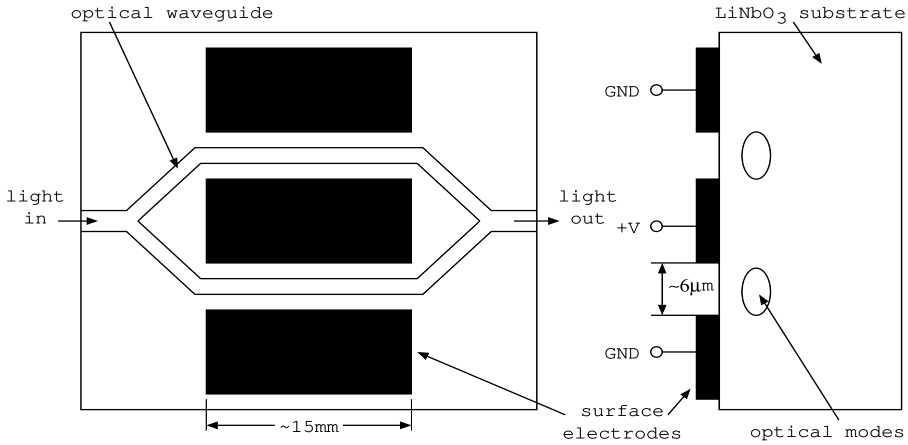

Figure 2.4: Structure of a Mach-Zehnder interferometer realized as a $LiNbO_3$ electro-optic intensity modulator. A figure redrawn from [Stefanini91]

The incoming light is splitted into two paths, traversing a distance of a few millimeters and recombined. The two distinct paths represent different optical path lengths. By applying different external voltages to the electro-optical sensitive material the path length difference is changed and the resulting interference at the recombination point can be tuned between constructive and deconstructive interference. Fig. 2.5 shows an example of the transfer characteristic of one test channel.

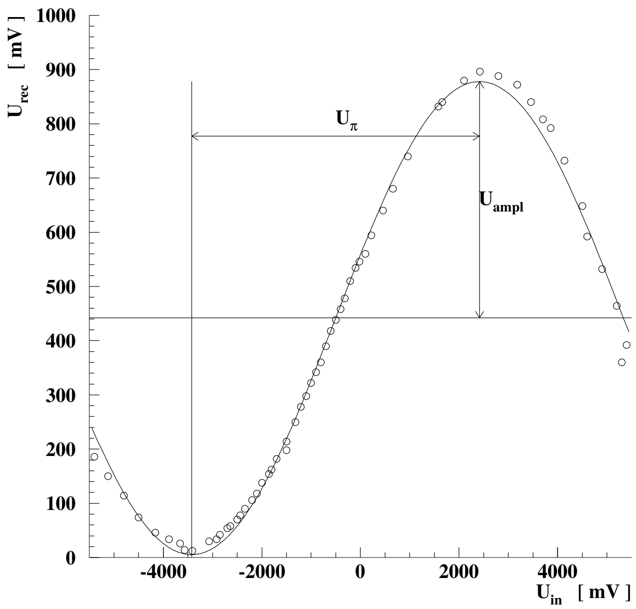

Figure 2.5: Transfer characteristic of a Mach-Zehnder interferometer

The measured points can be approximated by the graph of the mapping

$$U_{in} \quad \mapsto \quad U_{rec} = U_{ampl} \cdot \left[1 + \sin\left(\frac{\pi \cdot U_{in}}{U_\pi} - \phi \right) \right] \tag{2.1}$$

The voltage U_{rec} is measured with a PIN-diode receiver. This voltage is proportional to the transmitted light power. A typical light modulation power is $100\,\mu$W. U_π characterizes the periodicity of the interference method: If the voltage is changed by U_π the path length difference is changed by one half of the wavelength. The phase angle ϕ depends on the fabrication tolerances between the two light paths: Even if no external voltage is applied a certain phase difference might already be visible; it usually changes from channel to channel.

For the analog transfer of signals the nearly linear flank of the transfer characteristic has been chosen. The working point can be selected by applying a voltage U_{bias} in addition to the signal: $U_{in} = U_{bias} + U_{signal}$.

The transfer of a test PM pulse and its possible deformation has been checked. Fig. 2.6 compares in- and output signals including the complete chain, where both signals have been scaled to the same height. No obvious deformation has been observed.

Typical signal to noise values of 20 to 50 over the transmission chain could be achieved, where drifts could not be prevented due to variations in the polarization plane of the light.

Figure 2.6: Comparison of a PM pulse in front of and behind the optical link. Both signals have been scaled to the same pulse height to compare their shapes. No obvious distortion of the transmitted signal is visibel.

The polarization is subject to the torsion of the fibres and smallest movements (*e. g.* due to temperature variations) influence the working characteristics of the modulator.

The final bias voltages and gains of the amplifiers have been chosen in a way to transmit maximum signal heights which are equal to three simultaneous lead ions in a single quartz segment.

2.4.2 Double pulse resolution

The double pulse resolution of nearby PM pulses transmitted over the whole chain has been measured for the use with constant fraction discriminators. Fig. 2.7 shows the result of that measurement.

The functionality of the constant fraction discriminator is simulated by splitting the photomultiplier signal into two: The first is attanuated ($-6\,\mathrm{dB} \hat{=} 50\%$) and the second is delayed ($2.5\,\mathrm{ns}$). The zero crossing of the difference of both signals defines the discrimination point.

Two photomultiplier pulses close in time melt into one another and only one zero crossing can be detected. But if the time distance of both pulse is larger than about $7\,\mathrm{ns}$ the discriminator can distinguish them.

a.

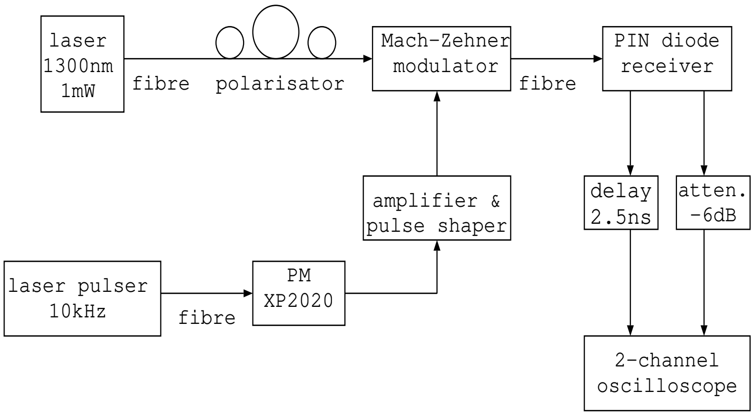

b.

Figure 2.7: Measurement of the double pulse resolution for the use with constant fraction discriminators: a. The schematic drawing. b. The result seen on the oscilloscope.
Shown are the delayed (2.5 ns) and attanuated (-6 dB) components of two photomultiplier signals with a time distance of 7 ns. Still two zero crossings of the difference between delayed and attanuated signal can be detected.

2.4.3 Read-out electronics

The electrical signal from a PIN diode receiver is splitted into two signal paths. One path is digitized by a fourfold time demultiplexer discriminator. A sequence of incoming signals is distributed onto four output lines, each carrying one forth of the incoming rate. Besides the timing registration of the digitized signals by time-to-digital converters (TDC), linear gates are driven, which allow to distribute the corresponding second path as an analog signal onto four analog-to-digital converters (ADC). With this mechanism one can read up to four individual pulse height and timing informations within one trigger. The total gate length of the TDCs is 80 ns, while the global ADC gate length is 120 ns. The linear gates reduce the effective gate length to 20 ns for the registration of an individual signal.

In case of more than four lead ions per read-out cycle the timing of the first four signals is registered but pulse height information of the additional lead ions is integrated on top of the first four ions.

The TDCs allow a single time measurement per channel with a precision of 50 ps. A wider look over 2.55 μs with less time resolution (10 ns) into the structure of the traversing lead ions can be done by so called *future-past registers*, which are driven in parallel to the TDCs. Per read-out cycle and channel they provide up to 255 timing informations. These registers have been adjusted in a way to show the lead ion structure 2 μs before and 0.5 μs after a trigger has initiated the read-out cycle.

2.5 Time of flight planes

Five time of flight hodoscopes are placed at different positions along the beam line (*cf.* Fig. 2.1, p. 10). Each hodoscope covers a sensitive area of $10 \times 10\,\mathrm{cm}^2$ using BICRON 404 scintillator material. Such an area is segmented into eight vertical slats with widths of 20 - 12 - 10 - 8 - 8 - 10 - 12 - 20 mm. This segmentation reduces the observed particle rate in the inner slats compared to a slat arrangement where all of them have equal widths. TOF1, 3 and 5 use scintillator slabs of 1 cm thickness, in TOF2 and TOF4 the thickness is 0.5 cm. Long bended light guides transport the light to the two inch photomultipliers Hamamatsu H1949. A whole plane has a size of about $1 \times 2\,\mathrm{m}^2$, *cf.* Fig. 2.8.

The time resolution for TOF1, 3 and 5 is about 85 ps and 110 ps for TOF2 and 4.

The analog signals of the TOF hodoscopes are fed into analog-to-digital converters (ADC) FERA 4300(A). In addition the analog signals are digitized by home made constant fraction discriminators. They have been optimized for minimal time walk effects. Principles of operation and performance for time of flight purpose have been described by F. Stoffel [Stoffel92]. The discriminated signals are fed into time-to-digital converters (TDC). They are realized in the combination of a time-to-charge converter (TFC) and an ADC. The nominal conversion factor is 50 ps/ `cnt` and time delays up to 80 ns seconds can be covered. In addition the discriminated signals from each channel of a TOF hodoscope are also registered by future-past registers to measure the time structure of secondary particles in the beam line.

The ADC information can be used to determine the charge of the traversing particle which is proportional to the square root of the measured ADC values. The high voltage of the photomultipliers have been adjusted in a way, so that an energy loss of one `mip`[1]; corresponds to 120 mV at 50 Ω. This allows to measure energy deposits of up to 25 `mip` with the used ADC modules.

2.6 Multiwire proportional chambers

At seven positions along the beam line multiwire proportional chambers are installed (W1T-W5T, W2S-W3S, *cf.* Fig. 2.1). Each of them covers a sensitive area of about $10 \times 10\,\mathrm{cm}^2$. A gas mixture of 75% argon and 25% isobutane is used.

[1] `mip` is an abbriviation for **m**inimum **i**onizing **p**article. 1 `mip` is the minimum energy loss of a singly charged particle due to ionization.

Figure 2.8: Drawing of a time of flight hodoscope

Each chamber consists of either two or three planes. A plane consists of 96 parallel wires stretched perpendicular to the beam axis. The chambers W2S and W3S are placed within the spectrometer section and have two planes to measure horizontal and vertical particle coordinates, while the chambers W1T-W5T are mounted a few centimeters behind the time of flight planes and have in addition to x and y a plane turned by 45^0 (v). In each plane three adjacent wires are read out by a common amplifier, so that an effective resolution of 3 mm is achieved. Only the position information is available, neither pulse height, nor timing information is provided.

2.7 Čerenkov counters

Two different types of Čerenkov counters are used to identify secondary particles in the beam line: two gas pressurized threshold counters (Č1, Č2) and one differential counter (CEDAR, *cf.* Fig. 2.1).

2.7.1 Threshold Čerenkov counter

A schematic view of one threshold Čerenkov counter is shown in Fig. 2.9.

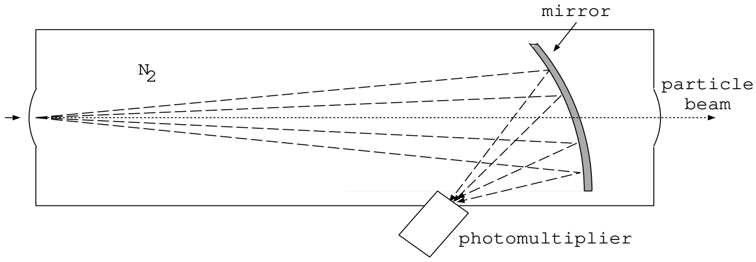

Figure 2.9: A schematic drawing of a gas pressurized threshold Čerenkov counter

It has got a sensitive length of 10 m and uses nitrogen as radiator. By varying its gas pressure (30 mbar$\lesssim\mathcal{P}\lesssim$2 bar) one can choose the threshold velocity to distinguish between slow and fast, or at a fixed momentum, between heavy and light particles. The threshold velocity β_t is inverse to the refractive index n of the gas, and the density of the gas is proportional to $(n^2-1)/(n^2+2)$. Thus, the threshold pressures $\mathcal{P}$ for a particle with mass m at a momentum p is given by

$$\mathcal{P} = \frac{(m/p)^2}{(m/p)^2+3}\cdot\mathcal{P}_K \tag{2.2}$$

$$\text{with}\quad \mathcal{P}_K = \frac{n_0^2+2}{n_0^2-1}\cdot\mathcal{P}_0 \approx 5000\,\text{bar} \tag{2.3}$$

where $n_0 = 1+3\cdot10^{-4}$, the refraction index of nitrogen at normal pressure $\mathcal{P}_0 = 1013$ mbar and temperature of 20 °C [PDG94]. Fig. 2.10 shows the corresponding curves $\mathcal{P}$ *vs.* p/Z for some indicated particles.

The number ϕ of produced photoelectrons for a particle with mass m is given by

$$\phi = \phi_0\cdot\frac{m_t^2-m^2}{p^2+m_t^2} = \phi_0\cdot\frac{\frac{3\mathcal{P}}{\mathcal{P}_K-\mathcal{P}}-\left(\frac{mc}{p}\right)^2}{1+\frac{3\mathcal{P}}{\mathcal{P}_K-\mathcal{P}}} \tag{2.4}$$

for a threshold pressure $\mathcal{P}$ or threshold mass m_t at momentum p. For pressure settings where the detectable particle spectrum is far away from the threshold, *i. e.* $(mc/p)^2 \ll (m_tc/p)^2 = 3\mathcal{P}/(\mathcal{P}_K-\mathcal{P})$, Eq. (2.4) can be simplified to

$$\phi = \phi_0\cdot\frac{3\mathcal{P}}{\mathcal{P}_K} \tag{2.5}$$

If ϕ is distributed according to a Poisson statistics, the detection inefficiency ϵ

$$\epsilon = e^{-\phi} \tag{2.6}$$

decreases exponentially with increasing pressure. The slope of the decrease is proportional to ϕ_0, which describes the general detector performance. It increases proportionally with the length of the radiator material; typical literature values for threshold Čerenkov counters are 90 cm^{-1} [PDG94].

The actually achieved performance of the Čerenkov counters in a limited pressure region has been measured using data from Pb$-$Pb interactions at a rigidity setting of

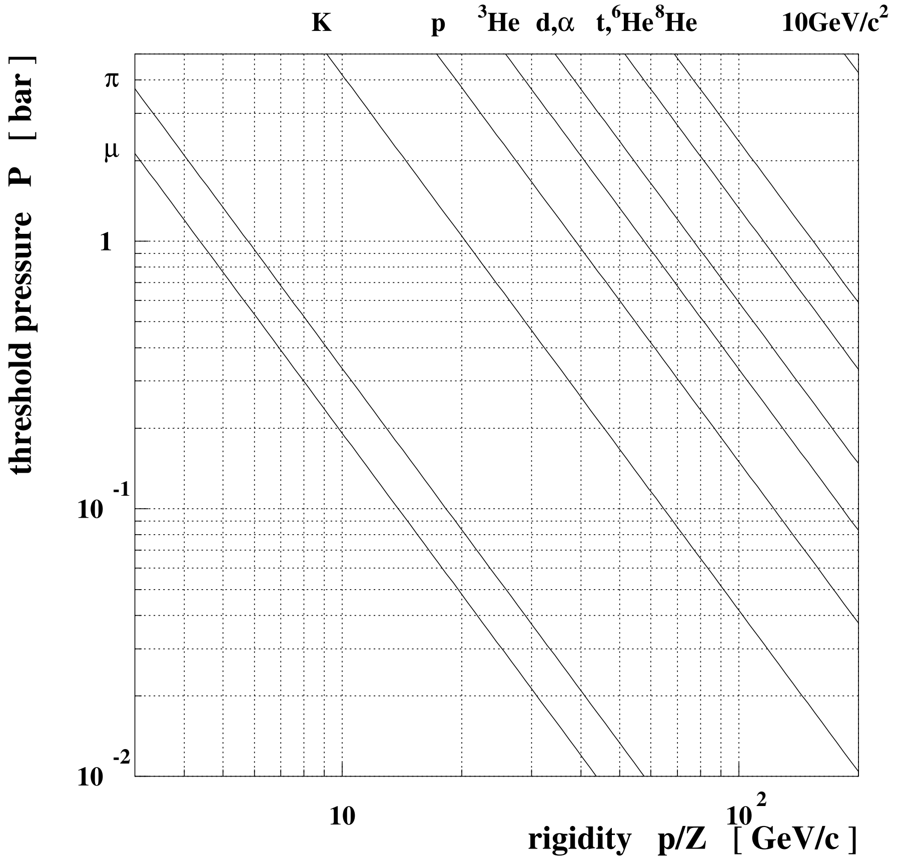

Figure 2.10: Threshold pressures $\mathcal{P}$ *vs.* particle rigidities p/Z for fixed particle values m/Z

$-200\,\text{GeV}/c$. A few different pressure settings between 30 and 300 mbar allow to prove Eq. (2.5) and to determine ϕ_0 of the used Čerenkov counters. To determine the inefficiencies experimentally, one counts those events from which no signal in Č1, but in Č2 is visible, although both counters should be sensitive to the same particle mix, since they are set to equal pressures:

$$\epsilon_{\check{C}1} = \frac{\#\text{ events without signal from Č1, but from Č2}}{\#\text{ events with signal from Č2}} \tag{2.7}$$

Similar the inefficiency of Č2 can be determined by interchanging the roles of Č1 and Č2. Typically a few hundred thousand events have been investigated per setting, while the point at 130 mbar includes about one million events. Fig. 2.11 shows the resulting inefficiency curve for both counters. No inefficient event has been found at 300 mbar out of 160'000 events. That is compatible with the extrapolation of the fit

$$\ln \epsilon - \epsilon_0 = \phi_0 \frac{3\mathcal{P}}{\mathcal{P}_K} \tag{2.8}$$

to the data points of Č1 at low pressures. The parameter ϵ_0 in Eq. (2.8) takes a deviation from Eq. (2.6) into account, which is visible in the extrapolation of the inefficiency fit to $\mathcal{P} \to 0$ with $\epsilon > 1$. The fit yields a slope with $\phi_0 = (1.08 \pm 0.04) \cdot 10^5$ or $108\,\text{cm}^{-1}$ considering the detector length of 10 m. The found values of Č2 give the impression that its efficiency is even better, although its efficiency gain with increasing pressure is smaller.

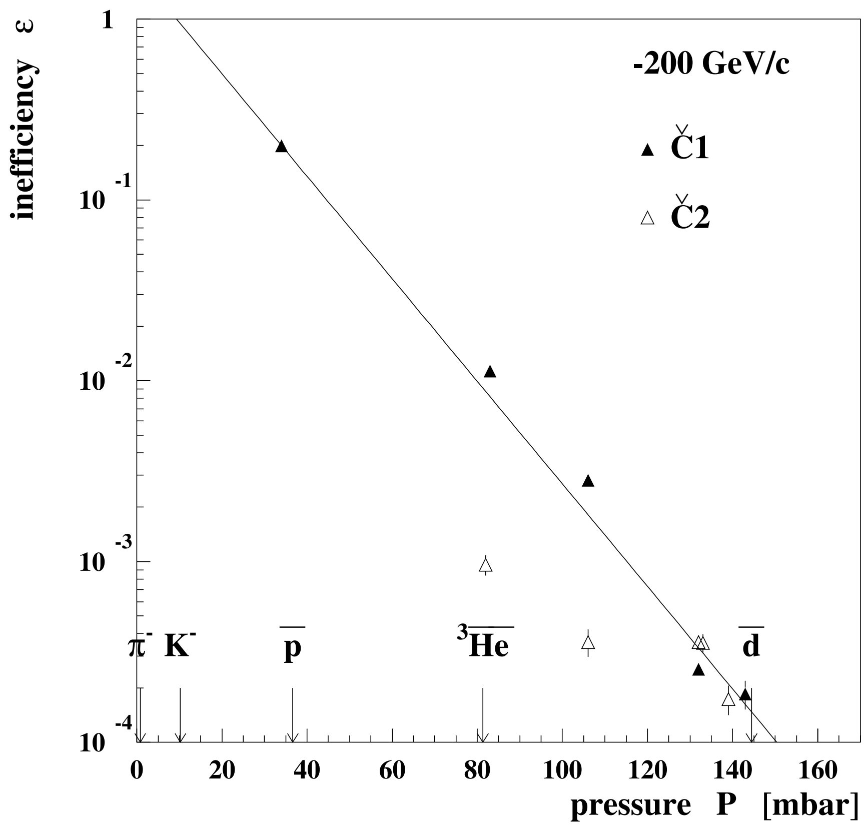

Figure 2.11: Measured inefficiencies of threshold counters Č1 and Č2. The indicated line is a fit to the data of Č1 according to $\ln \epsilon \propto \mathcal{P}$. Indicated are the threshold pressures for the particle species.

2.7.2 CEDAR

A schematic view of the differential Čerenkov counter is displayed in Fig. 2.12.

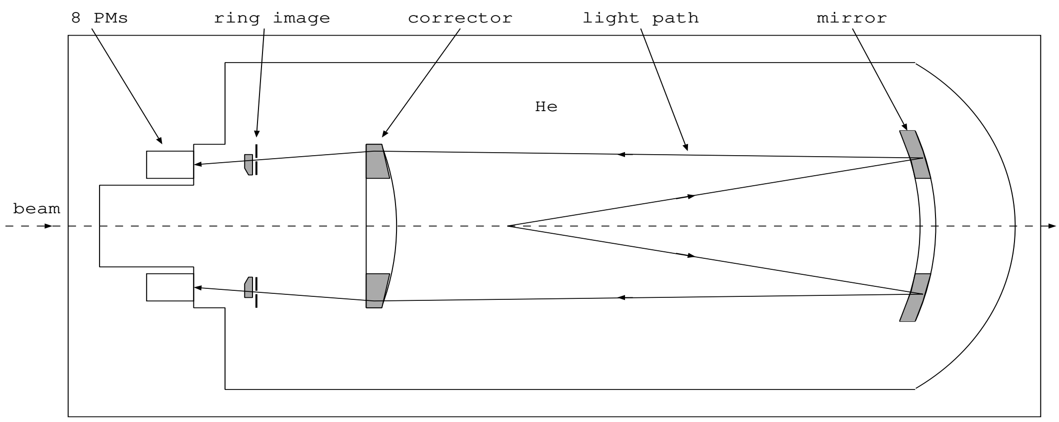

Figure 2.12: A schematic drawing of a CEDAR counter [Bovet82]

It uses helium as a radiator. Typical pressures are 11 to 13 bar. The optical system of a CEDAR focuses the Čerenkov light onto the plane of the diaphragm via a spherical mirror. Chromatic dispersion is reduced by a correcting system. The diaphragm cuts into the light cone of the Čerenkov light. Its opening angle is a function of the particle velocity and for a fixed momentum a specific particle mass can be identified by choosing an appropriate gas pressure, so that the light cone passes through the diaphragm. The choose of the diaphragm opening compromises between the efficiency of particle detection and separation.

Eight photomultipliers are used to detect the light cone. Their signals are discriminated and three different coincidences are derived: logical signals indicate 6-, 7- and 8-fold coincidences between the signal. This information allows to estimate the intrinsic efficiency of the CEDAR counter. For a given photomultiplier the efficiency η of recording the signal is given by

$$\eta = 1 - e^{-\phi} \tag{2.9}$$

where ϕ is the average number of recorded photoelectrons. If eight photomultipliers are watching the same event with similar efficiencies η, then the probabilities of observing the different levels of coincidence are given by

$$\begin{aligned} \eta_8 &= \eta^8 && (2.10)\\ \eta_7 &= \eta_8 + 8\eta^7(1-\eta) && (2.11)\\ \eta_6 &= \eta_7 + 28\eta^6(1-\eta)^2 && (2.12) \end{aligned}$$

Taking a particle beam passing through the CEDAR, which is tuned to tag one particle species, one can measure the intrinsic efficiencies of the CEDAR counter. Assuming that each efficiency level η_i is proportional to the observed amount of coincidences n_i, the three Eqs. (2.10-2.12) can be used to derive the mean efficiency of a photomultiplier in the CEDAR. Three different ratios n_i/n_j are available and they lead to the following efficiency formulae:

$$\begin{aligned} \eta\left(\frac{n_6}{n_7}\right) &= \frac{24 + 4\cdot\frac{n_6}{n_7} - 2\sqrt{4\left(\frac{n_6}{n_7}\right)^2 - \frac{n_6}{n_7} - 3}}{21 + 7\cdot\frac{n_6}{n_7}} && (2.13)\\ \eta\left(\frac{n_6}{n_8}\right) &= \frac{24 - \sqrt{21\cdot\frac{n_6}{n_8} - 12}}{21 - \frac{n_6}{n_8}} && (2.14)\\ \eta\left(\frac{n_7}{n_8}\right) &= \frac{8}{\frac{n_7}{n_8} + 7} && (2.15) \end{aligned}$$

These three values should be equivalent and can be used for a cross check. Typical measured efficiencies η agree within 10% and have been measured to be in the range 0.8 to 0.9, corresponding to about 1.6 to 2.3 photoelectrons per photomultiplier.

However, it should be emphasized that the overall particle detection efficiency also depends on the proper alignment of the CEDAR relative to the particle beam, *i. e.* for a absolute particle yield measurement the fraction of particles which falls into the optical acceptance of the CEDAR has to be derived by an independent measurement. In general this could not be checked in the off-line analysis due to the lack of data. But at one specific setting its tagging of antideuterons at -200 GeV/c could be compared with both threshold Čerenkov counters, with the result that the geometrical inefficiency is negligible (*cf.* section 6.3.2).

2.8 Calorimeter

The calorimeter consists of five individual modules and they are placed in sequence at the very end of the beam line, about 540 m behind the production target. These modules were built by the ZEUS collaboration for investigations about the compensation of hadronic calorimeters [Agostini89]. The NEWMASS collaboration reused these modules. Calibration and performance of the calorimeter has been already investigated earlier [Klingenberg92]. For the present experimental setup the modules have been modified in the read-out part and the granularity has been reduced.

Each of the five modules is horizontally segmented into twelve 5 cm wide scintillator bars. Light produced in three adjacent scintillator strips are guided via common wave length shifters to photomultipliers 56AVP/DVP. Fig. 2.13 shows the construction of a single module.

Figure 2.13: Construction of a calorimeter module [Agostini89]

Depleted uranium is placed in a sandwich structure: in 45 layers 3 mm thick scintillator bars are interlaced by 3.2 mm uranium plates. The fifth module has got a reduced depth. It consists of 30 layers with 5 mm thick scintillator bars 3.2 mm thick uranium plates. Scintillator and absorber plates are separated by steel foils of 0.2 mm thickness in order to reduce the signal induced by the radioactive decay of ^{235}U. All together the five modules cover seven hadronic interaction lengths in longitudinal direction and have got lateral dimensions of $60 \times 60\,\text{cm}^2$.

The read-out electronics consists of individual analog-to-digital converters FERA 4300. Integrators allow to measure the radioactive noise in the calorimeter channels. Typical energy deposits are a few MeV per decay of ^{235}U. This measurement of this signal, we call it **u**ranium **no**ise (UNO), allows to monitor the gain of the photomultipliers.

2.8.1 Calibration of the calorimeter

Each of the 20 calorimeter cells has been calibrated with a 50 GeV/c electron beam. That beam has been steered into the center of each individual cell and the high voltage has been adjusted to a value that the resulting ADC distribution peaks near 1000 ADC counts, allowing a dynamic range up to 100 GeV/c at 2000 ADC counts per cell. After the calibration the absorbed energy in an individual cell of a module is calculated as

$$E_{cell} = \frac{1}{2}\left(\frac{PH_{act}^{left}}{PH_{calib}^{left}}\frac{UNO_{calib}^{left}}{UNO_{act}^{left}} + \frac{PH_{act}^{right}}{PH_{calib}^{right}}\frac{UNO_{calib}^{right}}{UNO_{act}^{right}}\right) \tag{2.16}$$

where PH are the *act*ual and *calib*ration *p*ulse *h*eights, and UNO are the corresponding *u*ranium *no*ise values. All these numbers are pedestal subtracted ADC counts.

The total absorbed energy can be calculated as the sum

$$E = \sum_{cell} E_{cell} \tag{2.17}$$

A higher dynamic range (with less resolution) can be achieved by the reduction of the high voltage. Hereby the actual gain of the individual cells are monitored automatically by the uranium noise ratios. Besides the calibration range up to 100 GeV a second one up to 1000 GeV has been used to measure energies from particles at the high rigidity settings $\geq 100\,\mathrm{GeV}/c$

2.8.2 Performance of the calorimeter

The performance of the calorimeter after the calibration has been checked in both high voltage settings by various beam momenta between 10 and 200 GeV/c. Fig. 2.14 shows the nonlinearity and the resulting e/h ratio, while Fig. 2.15 presents the relative energy resolution for the electromagnetic and hadronic shower components. The relationship between the measured energy E_{calo} and the beam energy E_{beam} can be approximated by the linear relation ship

$$E_{calo,elm} = (0.896 \pm 0.007)E_{beam} + (7.45 \pm 0.71)\,\mathrm{GeV} \tag{2.18}$$

$$E_{calo,had} = (0.812 \pm 0.012)E_{beam} + (9.3 \pm 1.3)\,\mathrm{GeV} \tag{2.19}$$

Here, the points at $E_{beam} = 10\,\mathrm{GeV}$ have not been included into the fit since the nonlinearity has been only observed for large energies $E > 100\,\mathrm{GeV}$. The relative energy resolution can be parameterized as

$$\frac{\sigma_{elm}}{E} = \frac{0.174 \pm 0.019}{\sqrt{E/\,\mathrm{GeV}}} \oplus (0.009 \pm 0.004) \tag{2.20}$$

$$\frac{\sigma_{had}}{E} = \frac{0.357 \pm 0.001}{\sqrt{E/\,\mathrm{GeV}}} \oplus (0.028 \pm 0.002) \tag{2.21}$$

These values are systematically larger than the values published by the ZEUS collaboration [Agostini89]

$$\frac{\sigma_{elm}}{E} = \frac{0.176}{\sqrt{E/\,\mathrm{GeV}}} \oplus 0.004 \tag{2.22}$$

$$\frac{\sigma_{had}}{E} = \frac{0.345}{\sqrt{E/\,\mathrm{GeV}}} \oplus 0.010 \tag{2.23}$$

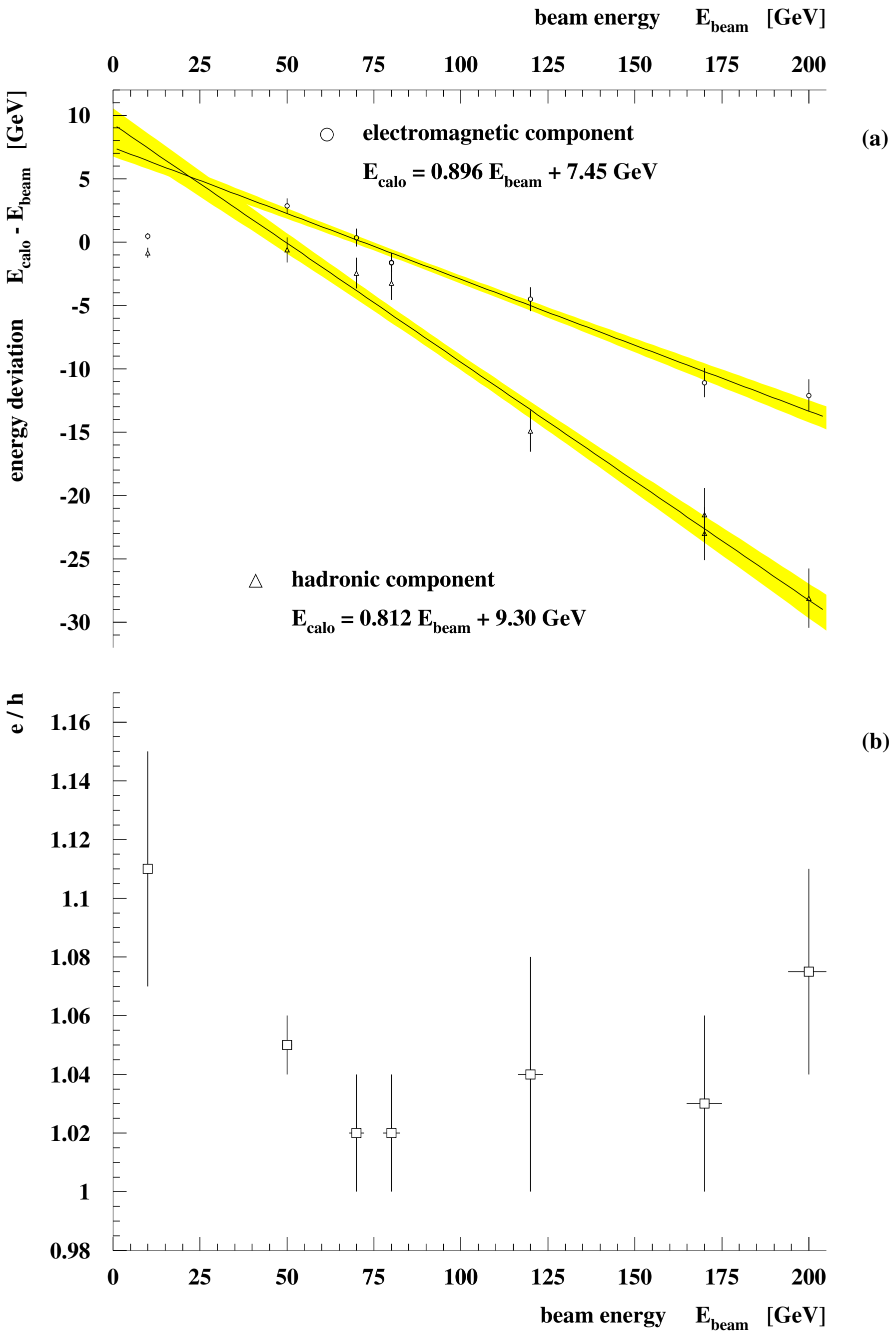

Figure 2.14: (a) Linearity of the calorimeter plotted as the energy difference $E_{calo} - E_{beam}$ *vs.* the beam energy E_{beam}. The solid line represents a linear fit to the data points where the point at 10 GeV has been omitted. The shadowed area represents the 1σ errors of the fit parameters including their correlation coefficients $\rho_{elm} = -0.904$ and $\rho_{had} = -0.878$, respectively.
(b) The measured e/h ratio.

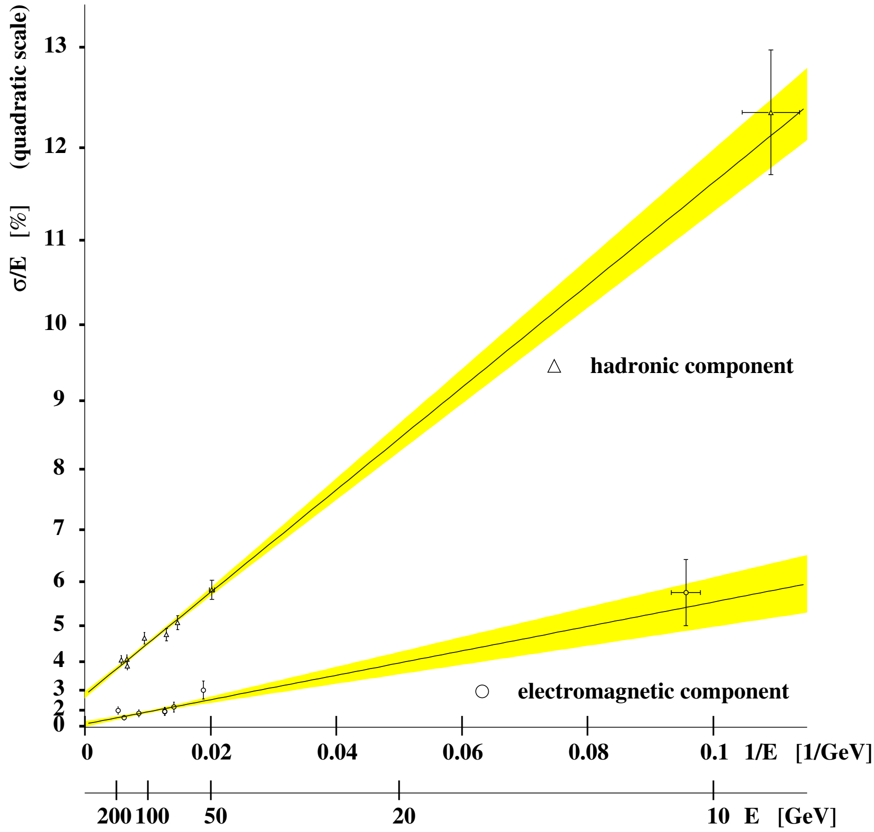

Figure 2.15: The relative energy resolution of the hadron calorimeter in a $(\sigma/E)^2$ *vs.* $1/E$ scale. The solid lines represent the linear fit to the data points for electromagnetic and hadronic showers. The shadowed areas represent the one sigma uncertainty of the fit parameters including their correlation coefficients $\rho_{elm} = -0.878$ and $\rho_{had} = -0.848$, respectively.

But such a difference can be understood, since in the latter case a leakage cut has been applied. Such a cut is for the NA52 purpose not applicable since one does not want to loose efficiency for the search for a rare particle species like strangelets, but uses the calorimeter for a redundancy check only.

Fig. 2.16 shows an example of the particle identification capabilities of the calorimeter using its segmentation. Here, a secondary beam at a laboratory momentum of 100 GeV is taken.

Plotted is the correlation

$$\frac{E1 - E2}{E} \quad vs. \quad \log_{10} \frac{E}{\mathrm{GeV}} \tag{2.24}$$

which is the relative energy difference in the first two modules *vs.* the total absorbed energy. The logarithmic scale of the latter value has been chosen to cover the large observable energy range.

Three different particle species can be distinguished with the calorimeter by the shower profile:

- muons (μ^-) behave similar to minimal ionizing particles and deposit about 0.5 GeV per module, while their total energy loss is around $10^{0.4}$ GeV = 2.5 GeV;

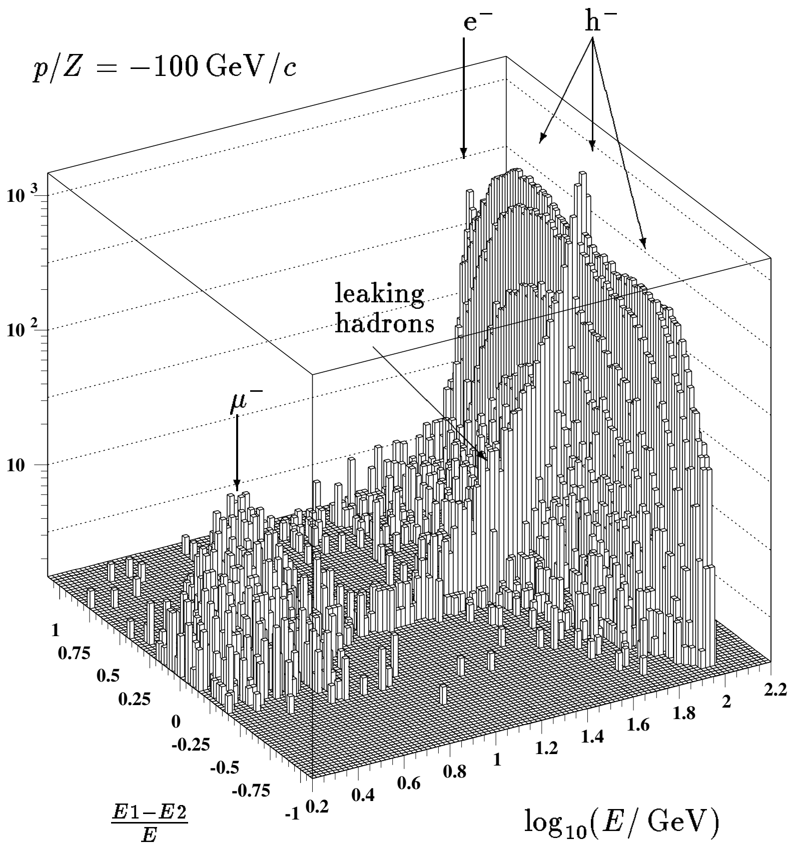

Figure 2.16: Using the calorimeter for particle identification purpose: plotted is the reduced energy difference as seen in the first two modules *vs.* the logarithm of the total absorbed energy. Hadrons can be distinguished from muons and electrons by their shower profiles.

- electrons (e^-) deposit their total energy of 100 GeV already in the first calorimeter module;
- while hadrons (h^-) show large fluctuations in their shower profiles: one group deposits a large fraction already in the first two modules of the calorimeter while the other group behave like minimal ionizing particles in the very beginning and their showering process starts only deeper in the calorimeter. For these events it is more likely that not the whole shower energy can be captured within the remaining three modules. One observes energy leakage.

2.9 Trigger and data acquisition

The read-out electronics is subdivided into two parts and located at separated positions in order to reduce the necessary length of cables and to cope with the timing of the read-out electronics. The first part covers all subdetectors including the quartz counter until TOF3/W3T, the second part covers the CEDAR until the calorimeter. Each read-out section has got its own trigger. It consists of the coincidence between an unsegmented scintillation counter and the logical "or" of the slabs of a TOF plane, *i. e.* B1·TOF2 in the upstream, and B2·TOF4 in the downstream part.

In each trigger a threshold Čerenkov counter can be used in anticoincidence in order to reduce the accepted trigger rate of light and fast particles. In this prescale mode the trigger condition reads $\mathrm{B1}\cdot\mathrm{TOF2}\cdot\overline{\check{\mathrm{C}}1}$ for most of the time. However, for calibration purpose the anticoincidence is switched off at a constant rate to trigger on the natural particle spectrum. Usually this rate was adjusted to 10 ms, so that typically 500 events per spill without the Čerenkov veto could be taken. The actual prescale factor for light particles depends on the particle flux and composition in the beam line, as well as on the the threshold pressure.

A global trigger combines the local up- and downstream parts. It is operated in two modes: Either it is sufficient to get a valid trigger in the upstream trigger, or the particle has to trigger in both parts to be accepted as a valid event.

In each local trigger electronics accepted events start the read-out cycle of the ADCs and the digitization of the wire chamber information. After the conversion is finished (it takes about 10 μs) the information of the ADCs is transfered (100 μs) to a 1 MByte HSM VME memory module and the wire chamber information is stored in a RMH VME memory module. These memory modules allow to store about 2000 events per spill. Spillwise these memory modules are copied to the local memory of an OS/9 data acquisition platform. Spillwise information from scalers are added, which give information about the trigger rates in the various detector systems. Moreover, electronic calibration events are taken in the spill pauses to measure pedestal values and TDC gain factors. A more detailed description can be found in section 4.1, p. 49.

The OS/9 DAQ system of the downstream trigger is operating as the master and joins the event- and spillwise information. Data streams of up to 200 MByte including about 150′000 events and calibration information are stored as *runs* on 8 mm Exabyte tapes.

Parallel running on-line monitor and calibration processes are used to prove the validity of data and functionality of detectors and electronics.

Chapter 3

Acceptance of the beam line H6

The central part of the NA52 detector setup is the H6 beam line. It is a single particle, focusing spectrometer transporting secondary particles from the target to the hadron calorimeter. It can be operated at magnetic rigidities between 5 and 200 GeV/c with a momentum bite of 2.8% accepting particles in a solid angle of 2.5 mrad $\times$ 0.9 mrad $=$ 2.2 μsr.

In this chapter the optics of the beam line is explained, the determination of the acceptance with the aid of a simulation programme TURTLE, the use of the multiwire proportional chambers to reconstruct the phase space of the transported secondary particles. A tentative comparison of a simulated and measured phase space is used to determine the systematic uncertainties of the simulated acceptance. The measurements are based on observed secondaries with 100 and 200 GeV/c momentum produced in Pb$-$Pb interactions.

3.1 Optics of the H6 beam line

The beam line H6 consists primarily of a sequence of three different magnet types, which have analogies in (geometrical) optics:

- Dipoles or bending magnets provide homogeneous fields bending charge particles according to their momentum. They behave like prisms.

- Quadrupoles produce two orthogonal field gradients. They function similar to optical lenses, but they have a focusing effect in one plane and a defocusing in the other.

- Sextupoles consist of three quadratic changing fields in order to correct for chromaticity.

In the vertical plane two bending sections, separated by about 250 m with deflection angles of $+41$ mrad and -41 mrad build up the spectrometer part. The placement of position sensitive detectors opens the possibility to determine the momenta of transported particles.

Three different operation modes are known for the beam line H6:

- the filter mode, mainly used during p – Be runs to produce and transport secondary particles or tertiary electrons and pions produced from a secondary target which is placed 130 m downstream;
- the high resolution mode to determine the momenta of secondaries with high accuracy, but with a rather low acceptance;
- and the high transmission mode, as used in Pb – Pb interactions to obtain the highest acceptance of the beam line for transporting secondary particles.

Basically these three modes are tuned by choosing different focal lengths of the quadrupoles. In this chapter only the high transmission mode is discussed.

The optics of the beam line is described with the aid of the TRANSPORT programme [Brown80]. It uses a geometric description of the beam line items and delivers beam optics matrices, which determine the transportation of a phase space element at the target down to any individual position along the beam line. Each point in phase space is defined by a vector of five elements

$$\Phi = (x, x', y, y', \delta)^T \tag{3.1}$$

Here, x and y are the horizontal and vertical beam position offsets, x' and y' the horizontal and vertical angles with respect to the nominal beam axis, and δ the relative momentum deviation $\delta p/p_0$ with respect to the nominal momentum p_0.

The deterministic description with the aid of the Maxwell equations allows to give exact predictions for the phase space at any given position in the beam line. However, the complexity of the magnetic fields, *e. g.* edge effects like fringe fields, allow only a numerical analysis. TRANSPORT allows to determine the phase space up to a second order Taylor series[1]

$$\Phi_b = R_{a\to b}\Phi_a + \Phi_a R^{2nd}_{a\to b}\Phi_a + O(\Phi_a^3) \tag{3.2}$$

Here, $R_{a\to b}$ is the first order 5×5 matrix while $R^{2nd}_{a\to b}$ is the second order $5 \times 5 \times 5$ tensor, both describing the transportation from the target a to some position b along the beam line. However, in this analysis only the first order elements are used, *i. e.* $R^{2nd} \equiv 0$.

The matrix R consists of twelve independent elements linking two phase space vectors at positions a and b:

$$\begin{pmatrix} x \\ x' \\ y \\ y' \\ \delta \end{pmatrix}_b = \begin{pmatrix} R11 & R12 & 0 & 0 & R16 \\ R21 & R22 & 0 & 0 & R26 \\ 0 & 0 & R33 & R34 & R36 \\ 0 & 0 & R43 & R44 & R46 \\ 0 & 0 & 0 & 0 & 1 \end{pmatrix}_{a\to b} \begin{pmatrix} x \\ x' \\ y \\ y' \\ \delta \end{pmatrix}_a \tag{3.3}$$

The off-diagonal zeros in the upper left 4×4 submatrix represent the fact, that in a high energy particle beam the horizontal and the vertical planes are basically decoupled, only the dispersion (fifth column) leads to a correlation. The fifth row represents the momentum conservation and its independence of beam position and angle.

Those six elements which determine the transverse position of the beam are graphically displayed in Fig. 3.1.

What can we learn from this picture?

[1]A newer version of TRANSPORT includes 3rd order elements, too. [Carey95]

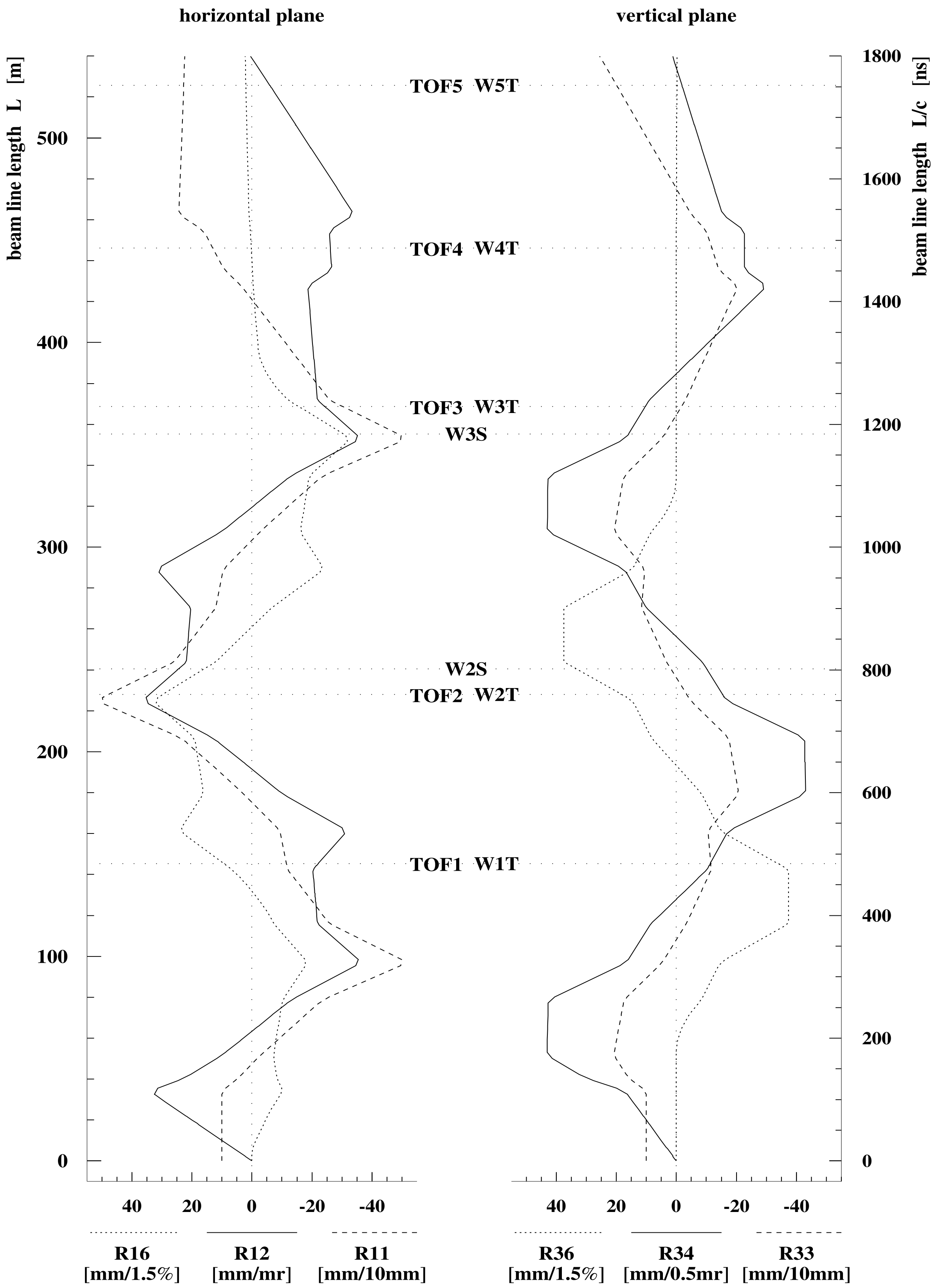

Figure 3.1: The transverse position of a charged particle along the beam line in the horizontal and vertical direction due to a position offset at the target (R11 and R33, dashed lines), due to an angular opening at the target (R12 and R34, continuous lines), and due to a momentum deviation (R16 and R36, dotted lines)

$R11$ and $R33$ (dashed lines) describe the transverse beam size due to a transverse position offset at the target. This is called the magnification of the beam line. The maximum magnification factor is five in the horizontal plane, while it is less than a factor two in the vertical plane. From this one expects a higher sensitivity to particle losses due to horizontal than to vertical beam shifts.

$R12$ and $R34$ (continuous lines) determine the beam dimension due to an angular opening of the beam. Here now the sensitivity of the vertical plane is higher: One expects a higher angular acceptance for particles with a horizontal deflection.

$R16$ and $R36$ (dotted lines) determine the influence of the chromaticity of the transported particles. Their maximal extensions are in the spectrometer section. The first string of vertical bends is located between 50 and 65 m while the second is between 305 and 330 m. Their deflection angles are $+41$ mrad and -41 mrad, respectively. In addition horizontal bends between 115 and 140 m with -24 mrad and between 370 and 395 m with $+43$ mrad also lead to momentum dependent deflections.

The position sensitive detectors – the scintillator hodoscopes TOF1-5 and the multiwire proportional chambers W1-5T and W2-3S — are indicated in Fig. 3.1, too. A special remark may be allowed to the positioning of the spectrometer chambers W2T/S and W3S/T concerning the vertical plane: They are sitting at beam line positions where the beam size is independent of the magnification. Moreover W3S/T are sitting at points where the size is also independent of the momentum. These chambers are measuring only the angular opening of the beam, while W2T/S do a combination of angular opening and momentum measurements. In the horizontal plane, W2T and W3S are sitting at points of maximum momentum dependence.

The use of these wire chambers to reconstruct the phase space at the target is described in section 3.3.

3.2 Simulation of the beam line acceptance

Tracks of individual particles can be simulated with the Monte Carlo programme TURTLE[2] [Brown74], which uses the transport matrices obtained with TRANSPORT. The TURTLE programme allows to determine particle losses due to finite aperture sizes and the angular widening of the beam due to multiple scattering. In the beam line H6 a particle has to pass material which corresponds to 0.25 radiation lengths.

3.2.1 Separated determination of the angular and momentum acceptance

To determine the solid angle acceptance of the beam line, a centered, monochromatic beam with a wide angular opening at the target is tracked through the beam line. The fraction of surviving particles up to TOF3 and TOF5, respectively, is counted in groups of small bins $dx' \times dy'$. On the other hand the momentum acceptance is determined by the aid of a centered, parallel beam. The fraction of transmitted particles is counted in small bins $\delta\delta$. These fractions can be regarded as transmission probabilities which are functions of angles and momentum deviations. The result for a 200 GeV/c beam is shown

[2]TURTLE is an acronym for **T**race **U**nlimited **R**ays **T**hrough **L**umped **E**lements.

in Fig. 3.2. For the angular acceptance lines of 1, 50 and 99% transmission are shown on

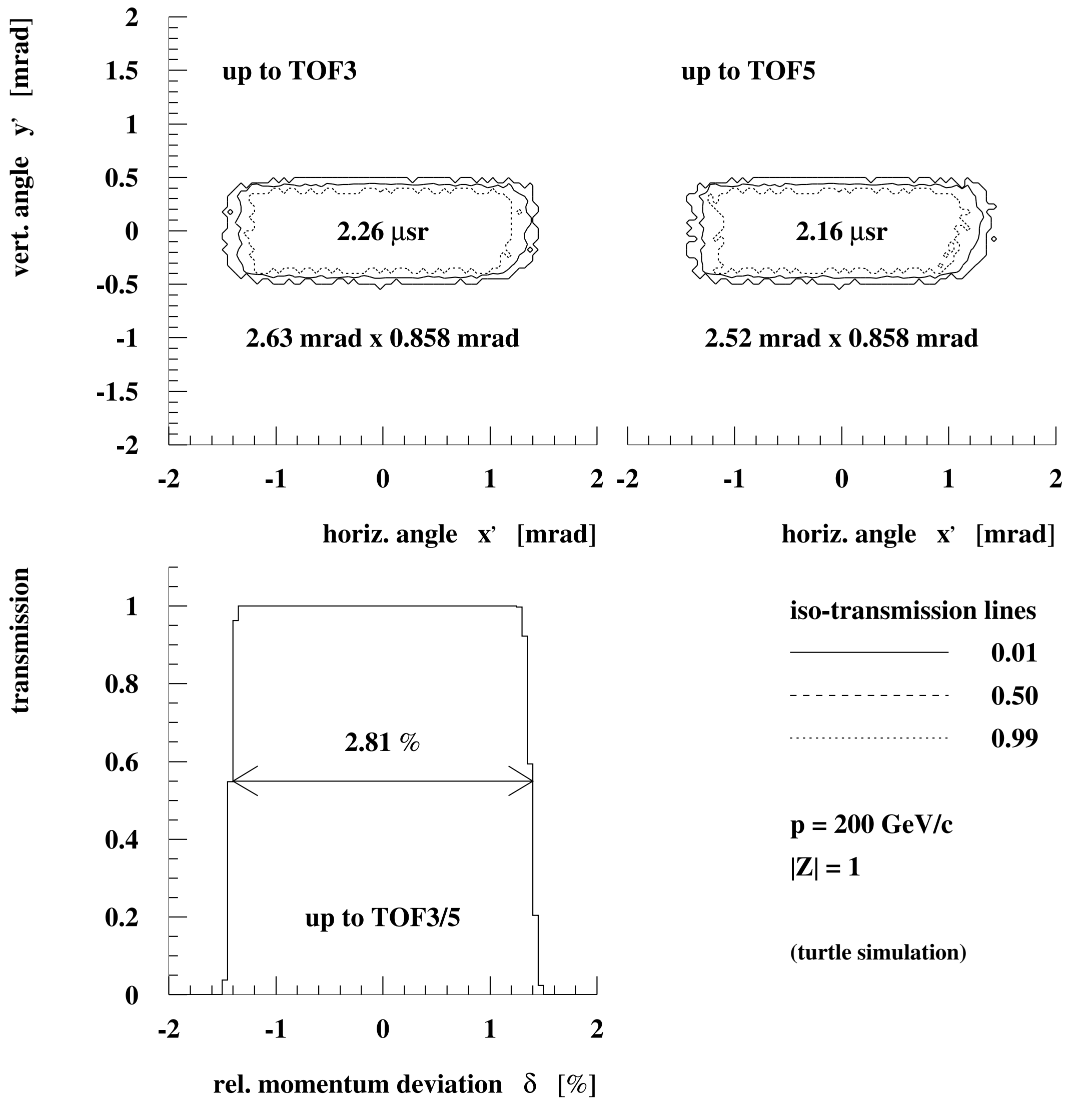

Figure 3.2: Simulation of the angular and momentum acceptance of the H6 beam line for a monochromatic and parallel beam, respectively at $p_{\mathrm{lab}} = 200\,\mathrm{GeV}/c$. The momentum acceptance stays constant between TOF3 and TOF5.

a two dimensional contour map, while for the momentum acceptance the transmission itself is displayed. If there would be no multiple scattering at all, one observes only two transmission regions with an abrupt boarder between 0 and 100%. But multiple scattering of the particles introduced by material along the beam line equal to 0.25 radiation lengths softens the boundaries.

Once the transmission shape is known the acceptance can be calculated. The quantitative numbers of the acceptance are determined as follows: The momentum acceptance for a parallel beam is calculated as an integral over the transmission $T(x', y', \delta)$ at fixed angles

$x' = y' = 0 \quad [T(\delta) \equiv T(x'=0, y'=0, \delta)]$

$$\Delta\delta = \int T(\delta)\,\mathrm{d}\delta \tag{3.4}$$

The solid angle acceptance $\Delta^2\Omega$ at a fixed momentum deviation $\delta = 0$ is the integral over the transmission $T(x', y') \equiv T(x', y', \delta = 0)$

$$\Delta^2\Omega = \int_{-\pi}^{+\pi}\int_{-\pi}^{+\pi} T(x', y') J(x', y') \mathrm{d}x'\mathrm{d}y' \approx \int_{-0.002}^{+0.002}\int_{-0.002}^{+0.002} T(x', y')\mathrm{d}x'\mathrm{d}y' \tag{3.5}$$

The solid angle can be expressed as a simple product of horizontal and vertical angles, since the angles themselves are small.[3] In a further step the solid angle acceptance can be subdivided into separated horizontal and vertical angular acceptances:

$$\Delta x' = \sqrt{\frac{\Delta^2\Omega}{\widetilde{\Delta x'}\widetilde{\Delta y'}}}\widetilde{\Delta x'} \quad , \qquad \Delta y' = \sqrt{\frac{\Delta^2\Omega}{\widetilde{\Delta x'}\widetilde{\Delta y'}}}\widetilde{\Delta y'} \tag{3.8}$$

with the auxiliary values

$$\widetilde{\Delta x'} = \int \frac{\int T^2(x', y')\mathrm{d}x'}{\int T(x', y')\mathrm{d}x'}\mathrm{d}y' \quad , \qquad \widetilde{\Delta y'} = \int \frac{\int T^2(x', y')\mathrm{d}y'}{\int T(x', y')\mathrm{d}y'}\mathrm{d}x' \tag{3.9}$$

The achieved numbers for a simulation with particles at 100 and 200 GeV/c are summarized in Tab. 3.1.

Table 3.1: Simulated separated solid angular and momentum acceptance

	up to TOF3			up to TOF5			
p [GeV/c]	$\Delta x'$ [mrad]	$\Delta y'$ [mrad]	$\Delta^2\Omega$ [μsr]	$\Delta x'$ [mrad]	$\Delta y'$ [mrad]	$\Delta^2\Omega$ [μsr]	$\Delta\delta$ [%]
200	2.63	0.858	2.26	2.52	0.858	2.16	2.81
100	2.61	0.858	2.24	2.45	0.850	2.09	2.81

The losses between TOF3 and TOF5 are 5% at 200 and 7% at 100 GeV/c for the solid angle acceptance, while the momentum acceptance remains constant in all cases. The slight difference of the angular acceptance for the two momenta already reflects the fact, that multiple scattering losses can be observed. They lead to a successive increase of the transverse beam dimensions and the chance to hit an aperture is enhanced.

[3] The transformation between TURTLE (x', y') and the polar angles (θ, ϕ) is

$$\tan^2\theta = \tan^2 x' + \tan^2 y' \quad , \quad \tan\phi = \frac{\tan y'}{\tan x'} \tag{3.6}$$

The exact expression for the functional determinant

$$J(x', y') = \sin\theta \frac{\partial(\theta, \phi)}{\partial(x', y')} = \frac{(1 + \tan^2 x')(1 + \tan^2 y')}{(1 + \tan^2 x' + \tan^2 y')^{\frac{3}{2}}} \tag{3.7}$$

differs less then 10^{-5} from $J(0,0) = 1$ in the interesting area $|x'|, |y'| \leq 2\,\mathrm{mrad}$.

3.2.2 Correlation between angular and momentum acceptance

The separated determination of the solid angular and momentum acceptance reflects a too optimistic picture of the acceptance, since the extreme values of the angular and momentum range cannot be reached independently.

To give a more realistic value of the usable acceptance a combined phase space with finite angular and momentum spread is transmitted through the beam line in the framework of the TURTLE programme. The fraction of particles, distinguished for different phase space points, is counted in small bins $d\delta \times d\theta$, where $\theta \approx \sqrt{x'^2 + y'^2}$ is the polar angle. This combination is appropriate for the study of azimuthal symmetric collisions. Fig. 3.3 gives an example of iso-transmission lines of 1, 50 and 99% for a 100 GeV/c beam until TOF3 and TOF5, respectively.

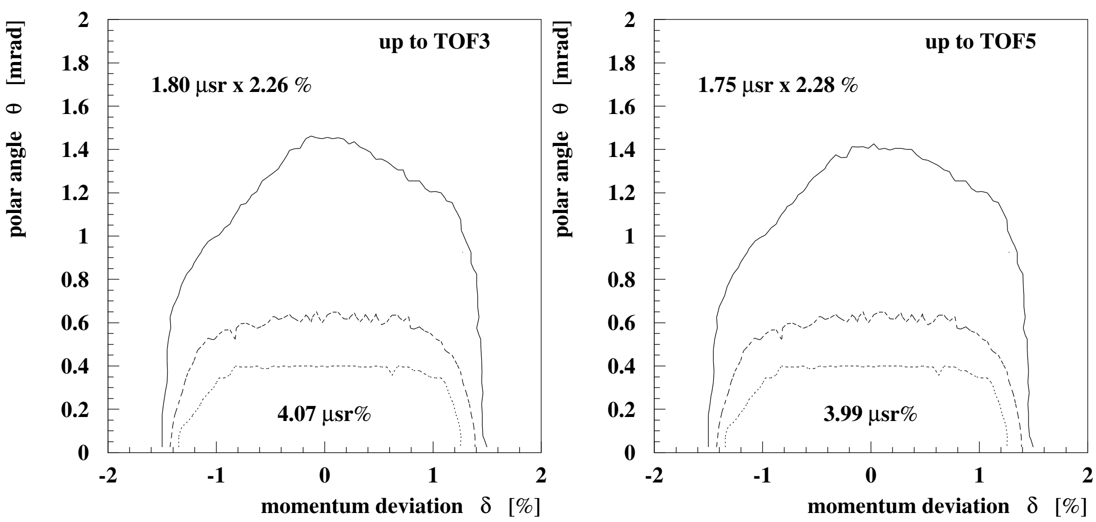

Figure 3.3: Simulation of the combined angular and momentum acceptance of the beam line at $p_{\mathrm{lab}} = 200\,\mathrm{GeV}/c$. The momentum acceptance approximately stays constant between TOF3 and TOF5.

An integrated acceptance can be calculated by summing up the transmission bins

$$\Delta^3\Omega\delta = \int\int T(\delta,\theta)\mathrm{d}\delta \sin\theta \mathrm{d}\theta \tag{3.10}$$

while the effective solid angular and momentum acceptances are determined individually via

$$\Delta^2\Omega = \sqrt{\frac{\Delta^3\Omega\delta}{\Delta^2\widetilde{\Omega}\Delta\widetilde{\delta}}}\Delta^2\widetilde{\Omega} \quad , \qquad \Delta\delta = \sqrt{\frac{\Delta^3\Omega\delta}{\Delta^2\widetilde{\Omega}\Delta\widetilde{\delta}}}\Delta\widetilde{\delta} \tag{3.11}$$

with the auxiliary values

$$\Delta^2\widetilde{\Omega} = \int \frac{\int T^2(\delta,\theta)\sin\theta\mathrm{d}\theta}{\int T(\delta,\theta)\sin\theta\mathrm{d}\theta}\mathrm{d}\delta \quad , \qquad \Delta\widetilde{\delta} = \int \frac{\int T^2(\delta,\theta)\mathrm{d}\delta}{\int T(\delta,\theta)\mathrm{d}\delta}\sin\theta\mathrm{d}\theta \tag{3.12}$$

These values have been obtained for different momenta between 5 and 200 GeV/c. The values are given in Tab. 3.2 and illustrated in Fig. 3.4.

Table 3.2: Momentum dependence of the combined angular and momentum acceptance

	up to TOF3			up to TOF5		
p	$\Delta^2\Omega$	$\Delta\delta$	$\Delta^3\Omega\delta$	$\Delta^2\Omega$	$\Delta\delta$	$\Delta^3\Omega\delta$
[GeV/c]	[μsr]	[%]	[μsr%]	[μsr]	[%]	[μsr%]
200	1.80	2.26	4.07	1.75	2.28	3.99
100	1.78	2.26	4.03	1.71	2.28	3.90
40	1.69	2.25	3.80	1.48	2.25	3.33
20	1.49	2.18	3.25	1.19	1.88	2.24
10	1.13	1.79	2.02	0.74	1.17	0.87
5	0.66	0.85	0.56	0.28	0.36	0.10

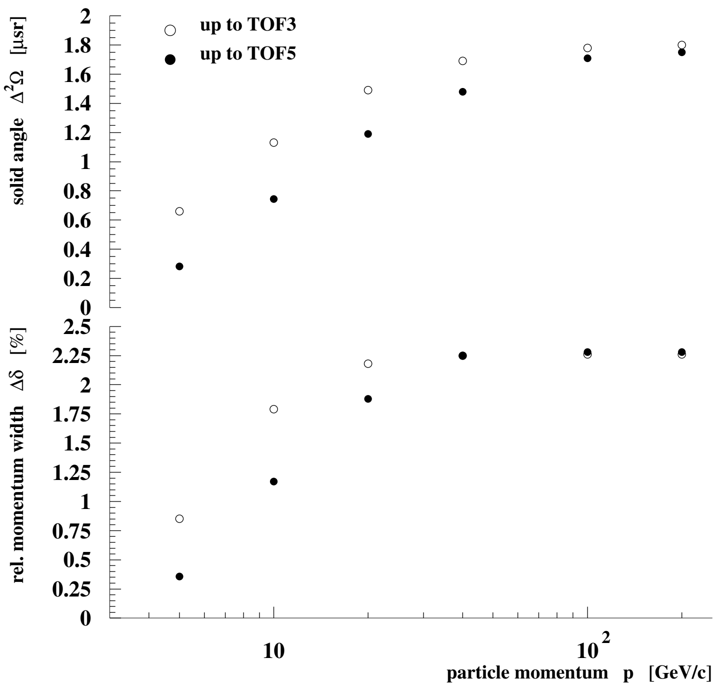

Figure 3.4: Simulated acceptance of the H6 beam line for different particle momenta.

For the high momenta $p \geq 100\,\mathrm{GeV}/c$ the acceptance is saturated, while for low momenta losses due to multiple scattering reduce the usable acceptance of the beam line tremendously.

The combined acceptances for high momenta are about a factor 1.5 smaller than the uncorrelated product for the separated acceptances (*cf.* Tab. 3.1).

3.2.3 Variations of the acceptance with the beam position at the target

As long as the exact position of an individual lead ion at the target is not known, the question arises how the acceptance reduces by varying the origin of the secondary beam with respect to the nominal beam axis. This point stresses mainly the magnification of the beam optics.

The quartz Čerenkov counter in front of the target has a diameter of 13 mm and the used targets are of the same order. Consequences of beam position variations in this area are investigated.

The results for one quadrant with the size of $7\,\mathrm{mm} \times 7\,\mathrm{mm}$ in 1 mm steps are displayed in Fig. 3.5 for a 100 GeV/c beam.

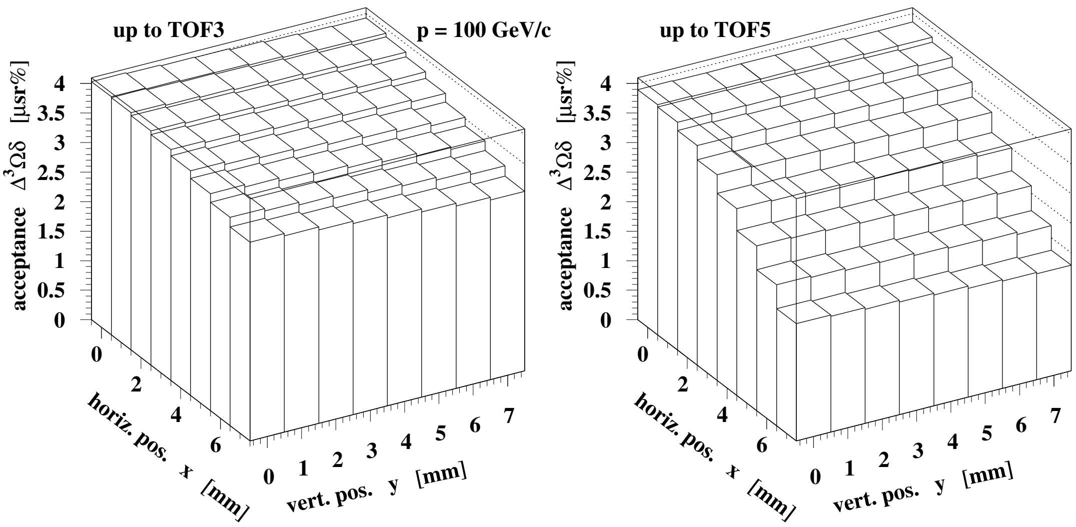

Figure 3.5: Simulated variation of the beam line acceptance with the incident beam position in a quadrant of a $7\,\mathrm{mm} \times 7\,\mathrm{mm}$ extent

It shows, that mainly a horizontal shift reduces the acceptance while it is less sensitive to a vertical offset. A horizontal shift of 5 mm reduces the acceptance until TOF3 by about 10% while the loss until TOF5 is around 30% compared to a centered beam. Such a different behavior between TOF3 and TOF5 can be understood, if one includes the multiple scattering widening of the beam (*cf.* section 3.3.2).

This result should be compared by measurements of the mean beam position.

The beam spot shape has been measured to be roughly Gaussian with widths[4]

$$\mathrm{FWHM}(x) = 1.1\,\mathrm{mm} \quad , \qquad \mathrm{FWHM}(y) = 2.4\,\mathrm{mm} \tag{3.13}$$

by steering the incident beam over the edge of the quartz counter and registering the observed rate drop in this counter.

Moreover the fourfold segmentation of the quartz counter allows to determine mean beam positions by using the symmetry variables

$$S_H = \frac{left - right}{left + right} \quad , \qquad S_V = \frac{up - down}{up + down} \tag{3.14}$$

where $left$, $right$, up and $down$ are the counting rates in two adjacent segments of the quartz counter, as indicated in Fig. 3.6.

[4]private communication from K. Elsener, CERN-SL.

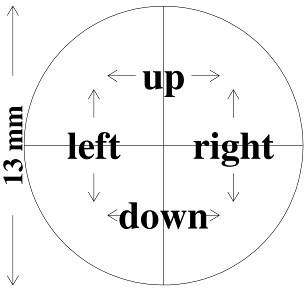

Figure 3.6: Particle rate measurements in two adjacent segments of the quartz counter are used to calculate the symmetry variables S_H and S_V and allow to estimate mean beam impact positions.

S_H and S_V with values near zero indicate a well centered beam. Actually measured symmetry values were mostly varying in the range $0.8 \leq |S_H| \leq 0$ in the horizontal plane, but quite small and stable ($|S_V| < 0.1$) in the vertical plane. The combination of the known beam width and continuously measured symmetry values allows to estimate mean beam impact positions on the quartz counter by

$$\langle x \rangle \sim S_H \cdot \mathrm{FWHM}(x) \quad , \qquad \langle y \rangle \sim S_V \cdot \mathrm{FWHM}(y) \tag{3.15}$$

where the exact relationship is determined by the shape of the beam profile itself. For a symmetry value of $S = 0.8$ a Gaussian beam shape is moved by a distance of about $0.6 \cdot \mathrm{FWHM}$. From the observed numbers one can conclude, that the mean beam positions were varying in the order of a millimeter or even less. However, the position of individual lead ions cannot be determined by this method.

From these calculations and measurements one can draw the conclusion that for the bulk of secondary particles the transmission probability is not reduced by the magnification effect and apertures of the beam line. But if there are offset and misalignments of the incident beam these are most visible in the horizontal plane for particles tracks up to TOF5.

3.3 Track fitting

The implementation of position sensitive detectors along the beam line opens the possibility to measure the actual track of the particle in the beam line, and the known beam optics allows to reconstruct the phase space point of this track at the target.

In this analysis the multiwire proportional chambers W1T, W2T, W2S, W3S and W3T are used for this purpose. While the S-chambers deliver horizontal and vertical coordinates the T-chambers deliver an additional coordinate v, which is rotated by 45^0. This allows to reduce ambiguities in cases of multiple particle hits. Their arrangement is displayed in Fig. 3.7.

In each coordinate 32 channels with a spacing of 3 mm are read out, so that an area of about $100\,\mathrm{cm}^2$ is covered by each of these chambers.

In principle also the position information of the chambers W4T and W5T could be included into the track fitting. But since part of the data has been taken with the trigger condition B1·TOF2, the information of the last two chambers are not available for each event. A comparison between data and simulation would be more difficult.

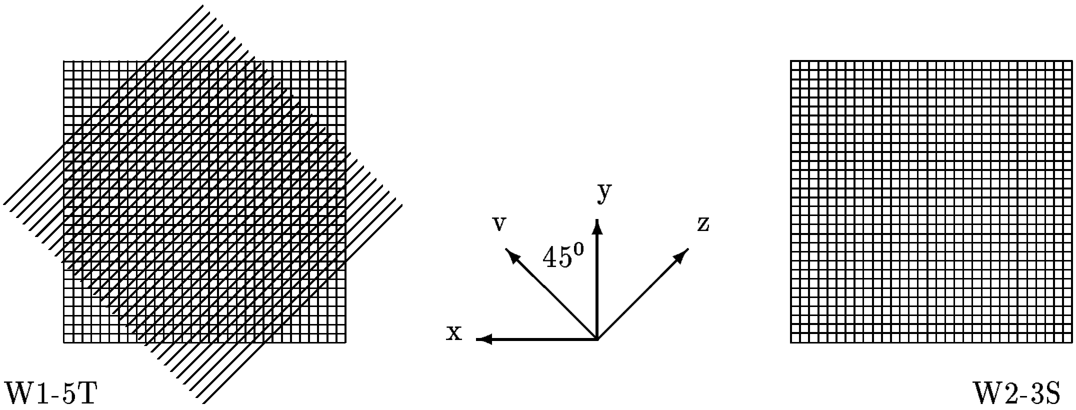

Figure 3.7: The relative positioning of the x-, y- and v-coordinates. v is turned by 45^0 with respect to the y direction. x and y together with the particle direction along z define a right handed coordinate system.

3.3.1 Mathematical procedure of the track fitting

A short description of the track fitting is given.

The basic idea is that the phase space point Φ of the track at the target[5] leads to well defined lateral coordinates C at the positions of the wire chambers

$$C = \mathcal{R}\Phi \tag{3.16}$$

where the vector C consists of the $n_C \leq 13$ lateral coordinates[6] and operator $\mathcal{R}$ is described by the beam optics.[7] In this analysis the problem is linearized and $\mathcal{R}$ simplifies to a $5 \times n_C$ matrix. Eq. (3.16) then is of the form

$$\begin{pmatrix} x_{W1T} \\ y_{W1T} \\ \vdots \\ v_{W3T} \end{pmatrix} = \begin{pmatrix} R11_{W1T} & R12_{W1T} & 0 & 0 & R16_{W1T} \\ 0 & 0 & R33_{W1T} & R34_{W1T} & R36_{W1T} \\ \vdots & \vdots & \vdots & \vdots & \vdots \\ sR11_{W3T} & cR12_{W3T} & sR33_{W3T} & cR34_{W3T} & \begin{array}{c} sR16_{W3T} \\ +cR36_{W3T} \end{array} \end{pmatrix} \begin{pmatrix} x \\ x' \\ y \\ y' \\ \delta \end{pmatrix} \tag{3.17}$$

The elements Rij are the beam optics values as used in Eq. (3.3) or shown in Fig. 3.1 as a function of the longitudinal coordinate along the beam line. The values s and c are the projections of the x and y coordinates onto the v-direction:

$$s = \sin 45^0 = \frac{1}{\sqrt{2}} \quad , \quad c = \cos 45^0 = \frac{1}{\sqrt{2}} \tag{3.18}$$

This approach is formally simpler than a hit and coordinate merging.

If we now do an actual measurement of the set of coordinates C one can predict the phase space Φ by an inversion of Eq. (3.16). However, practically (3.16) is an overdetermined

[5]If not marked specially Φ denotes the phase space at the target, the index a is omitted form here on.

[6]Up to 13 ($= 3 \times 3 + 2 \times 2$) measurement points are possible if all planes of chambers W1T... W3T have been hit. But, if – due to some inefficiency or particle losses – coordinates are missing, still the same method with a reduced size of matrices and vectors can be used.

[7]In order to simplify the reading in this chapter no symbolic distinction between true, measured and estimated values is done, since the different meanings are always obvious.

linear equation, where the coordinates suffer under measurements uncertainties and correlations. One possible method to derive the phase space point is the *method of least squares*, which is applicable for a linear model and Gaussian distributed measurement uncertainties. It can be derived from the maximum likelihood theorem. Here, the goal is to minimize the value

$$\chi^2 = (C - \mathcal{R}\Phi)^T V_C^{-1} (C - \mathcal{R}\Phi) \tag{3.19}$$

including the $n_C \times n_C$ covariance matrix V_C. This matrix accounts for the measurement uncertainties and their correlation. Values of the covariance matrix are derived in section 3.3.2. The necessary condition for a minimum of χ^2 by varying the elements of Φ leads to the *normal equation*

$$(\mathcal{R}^T V_C^{-1} \mathcal{R})\Phi = \mathcal{R}^T V_C^{-1} C \tag{3.20}$$

As long as the placement of the wire chambers allows an independent measurement of all five phase space coordinates, Eq. (3.20) can be solved by a matrix inversion.

3.3.2 The covariance matrix of the measured coordinates and the multiple scattering contributions to the beam optics

The covariance matrix V_C consists of two different parts, which describe geometrical measurement uncertainties and resolution losses due to multiple scattering.

First of all there is a geometrical term, based on the estimated uncertainties of the measured coordinates. These diagonal terms expressed in Gaussian equivalent widths[8]

$$\sigma_x = \sigma_y = \sigma_v = 3\,\mathrm{mm} \left(\int_{-0.5}^{+0.5} x^2 \mathrm{d}x \right)^{\frac{1}{2}} = \frac{3\,\mathrm{mm}}{\sqrt{12}} \equiv \sigma_{ws} \tag{3.21}$$

are corresponding to a flat hit distribution between the 3 mm wire spacing,

The multiple scattering of a particle in the material along the beam line leads to an angular deviation of its track, which is not described in the beam optics, but results in a position smearing of the track. This contribution brings in correlations between the horizontal and vertical plane.

The Coulomb scattering distribution is well represented by the theory of Molière [Molière47]. It is roughly Gaussian for small deflection angles, but at larger angles it behaves like Rutherford scattering, having larger tails than does a Gaussian distribution. In reference [PDG94](sect. 10.6) it is stated that the central 98% of the plane projected angular distribution is approximated by a Gaussian distribution with a width of [9]

$$\sigma'_{X_0} = \frac{0.0136\,\mathrm{GeV}/c}{\beta p/Z} \sqrt{X_0}\,[1 + 0.038 \ln X_0] \tag{3.22}$$

where the traversed material is characterized in (relative) radiation lengths X_0.

[8]Strictly speaking these errors are not Gaussian, but flat distributed. It would mean, that one has to use a more general approach, *e. g.* the *maximum likelihood method*, which would be much more complex and not justified for this purpose here. Reference [Chen94] gives a quantitative comparison of different fit methods for tracking problems.

[9]Further discussions of more precise parameterizations can be found *e. g.* in reference [Lynch91].

Using this for all known materials and all positions along the beam line in conjunction with the beam optics, the elements of the covariance matrix

$$V_C = \begin{pmatrix} \sigma^2_{xx,W1T} & \sigma^2_{xy,W1T} & \sigma^2_{xv,W1T} & 0 & \cdots & 0 \\ \sigma^2_{yx,W1T} & \sigma^2_{yy,W1T} & \sigma^2_{yv,W1T} & 0 & \cdots & 0 \\ \sigma^2_{vx,W1T} & \sigma^2_{vy,W1T} & \sigma^2_{vv,W1T} & 0 & \cdots & 0 \\ 0 & 0 & 0 & \sigma^2_{xx,W2T} & \cdots & 0 \\ \vdots & \vdots & \vdots & \vdots & \ddots & \vdots \\ 0 & 0 & 0 & 0 & \cdots & \sigma^2_{vv,W3T} \end{pmatrix} \tag{3.23}$$

are determined via sums like [Regler78]

$$\sigma^2_{xx,W} = \sigma^2_{ws} + \sum_b^{b<W} \left[R12_{b\to W}\sigma'_{X_0}\right]^2 \tag{3.24}$$

$$\sigma^2_{xy,W} = \sigma^2_{yx,W} = \sum_b^{b<W} R12_{b\to W} R34_{b\to W} {\sigma'_{X_0}}^2 \tag{3.25}$$

$$\sigma^2_{xv,W} = \sigma^2_{vx,W} = \sum_b^{b<W} R12_{X_0\to W}\left[sR12_{b\to W} + cR34_{b\to W}\right]{\sigma'_{X_0}}^2 \tag{3.26}$$

$$\sigma^2_{yy,W} = \sigma^2_{ws} + \sum_b^{b<W} \left[R34_{b\to W}\sigma'_{X_0}\right]^2 \tag{3.27}$$

$$\sigma^2_{yv,W} = \sigma^2_{vy,W} = \sum_b^{b<W} R34_{b\to W}\left[sR12_{b\to W} + cR34_{b\to W}\right]{\sigma'_{X_0}}^2 \tag{3.28}$$

$$\sigma^2_{vv,W} = \sigma^2_{ws} + \sum_b^{b<W} \left[sR12_{b\to W} + cR34_{b\to W}\right]^2{\sigma'_{X_0}}^2 \tag{3.29}$$

The matrix elements $Rij_{b\to W}$, transporting the phase space from a position b with material X_0 to a wire chamber W, can be derived from the matrix product

$$R_{b\to W} = R_{a\to W}R^{-1}_{a\to b} \tag{3.30}$$

The evolution of these multiple scattering contributions to the covariance matrix is visualized in Fig. 3.8. The shape of the covariance evolutions for the two momenta 100 and 200 GeV/c is comparable, but the contribution at 100 GeV/c is about a factor 4 higher, so that wire spacing and multiple scattering already become comparable at W2T, while this crossing point is reached at W3T for the highest momentum. The largest contribution to the multiple scattering arise from the TOF hodoscopes and the Čerenkov counters (with 2.5 to 3%X_0 each). The points of relative minima correspond to a beam focus ($R12$, $R34 \approx 0$), while the maxima correspond to parallel sections ($|R12|$, $|R34|$ large and constant). Furthermore these plots illustrate the acceptance loss between TOF3 and TOF5 due to the beam widening, which becomes severe, if one has in addition magnification contributions (*cf.* section 3.2.3).

The covariance value σ^2_{xy} roughly follows the individual variance values, introducing a high correlation

$$\rho_{xy} = \frac{\sigma^2_{xy}}{\sigma_x\sigma_y} \gtrsim 0.6 \tag{3.31}$$

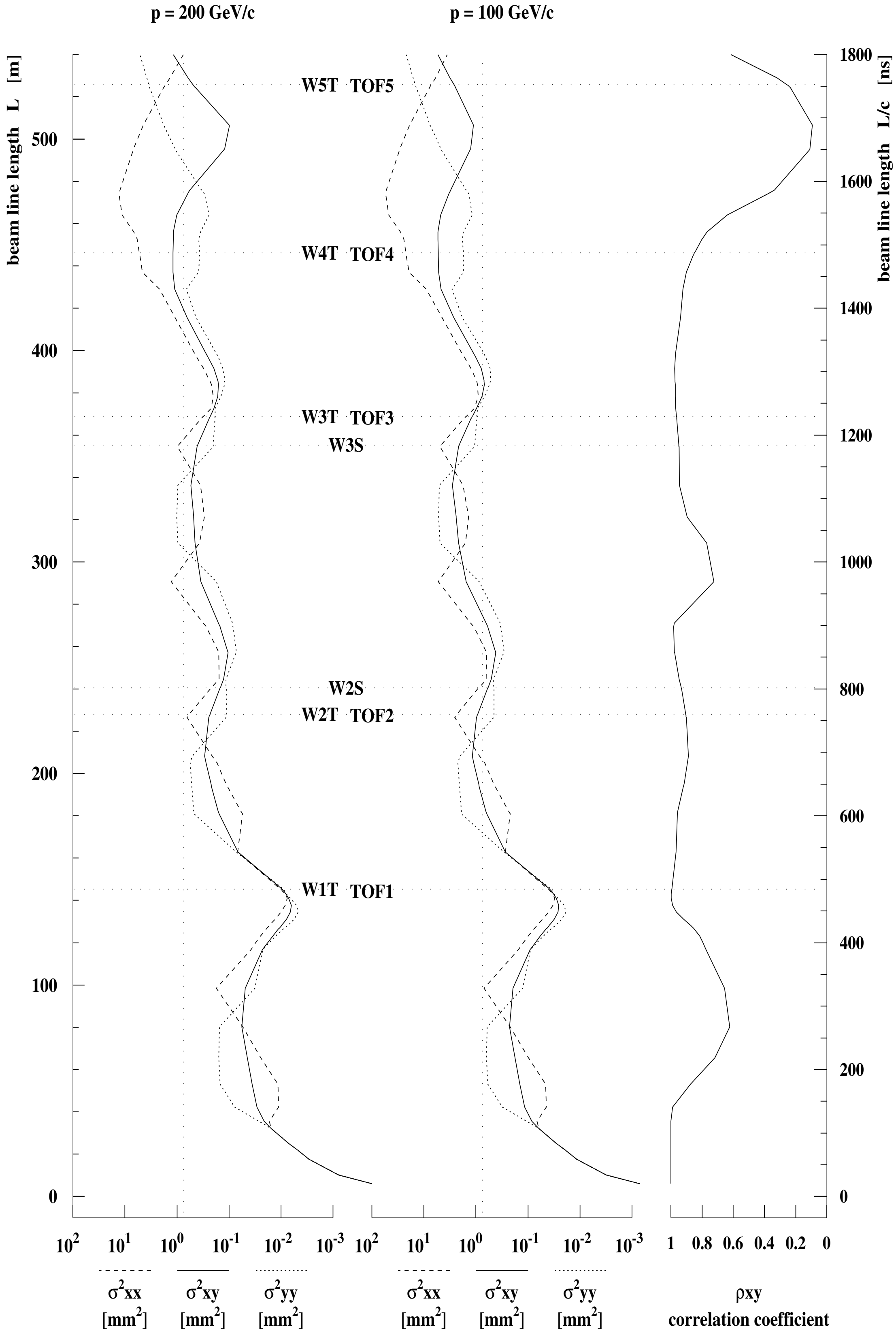

Figure 3.8: Evolution of the covariance matrix elements due to multiple Coulomb scattering effects at 200 GeV/c and 100 GeV/c. The vertical dotted line represents the resolution of the 3 mm wire spacing. The right column shows the relative correlation between the horizontal and vertical plane. It is momentum independent.

between the horizontal and vertical plane for the first 400 m of the beam line. This correlation is momentum independent.

For low momenta the multiple scattering contributions increase tremendously and is expected to be the most important part, even for measurements at the very first chamber W1T. Multiple scattering effects in the target itself have been neglected.

3.3.3 Application of the track fitting

The track fitting described above has been applied to some data samples taken at 100 and 200 GeV/c and a comparison with the TURTLE simulation has been carried out in order to check the actual transported phase space from the target through the beam line.

3.3.3.1 TURTLE simulation of the track fitting

The TURTLE programme uses the formulae[10]

$$\sigma'_{X_0} = \begin{cases} \dfrac{0.0216\,\mathrm{GeV}/c}{p/Z}\sqrt{X_0}\sqrt{-\ln r_2} & \text{if} \quad r_1 > 0.0143 \\ \dfrac{0.0445\,\mathrm{GeV}/c}{p/Z}\sqrt{X_0}\sqrt{r_2 + 10^{-7}} & \text{otherwise} \end{cases} \tag{3.32}$$

for the polar angular widening of the beam due to Coulomb scattering in material with radiation length X_0, where $r_1, r_2 \in (0, 1)$ are flat distributed pseudo random numbers. In 98.57% of the scattering a small angle deviation is taken, while in the remaining 1.43% a wider Rutherford scattering is applied.

In the simulation the transmission of the beam line is probed by particles with a flat momentum and angular distribution at the target. The coordinates of the simulated traces at the wire chamber locations are binned according to the wire spacing and fed into the fit procedure (Eqs. (3.19) and (3.20)) to get the actual transported phase space. In addition the start position of the beam at the target are smeared by small Gaussian distributions with full widths stated in Eq. (3.13), which represent the measured natural widths of the lead ion beam.

The result of the fit for a sample of 100'000 traces is displayed in Fig. 3.9. The indicated widths are *full width one tenth maximum* numbers and represent somehow the transported phase space, if one considers the natural widening of these distributions due to the limited resolution and introduced correlations in these phase space variables. The simulated full width one tenth maximum resolutions for the phase space variables are indicated in Tab. 3.3 and Fig. 3.10 for momenta between 5 and 200 GeV/c. It becomes obvious, that a track reconstruction at low momenta becomes almost meaningless due to multiple scattering.

The hedgehog structure of the vertical angle distribution in Fig. 3.9 is due to the limited spatial resolution of wire chamber W3T which sees the narrowest beam profile of all chambers in vertical direction.

[10] The values of Eqs. (3.22) and (3.32) become comparable if one considers the factor $\sqrt{2}$ for the projection of the polar angle (3.22) onto a transverse plane (3.32).

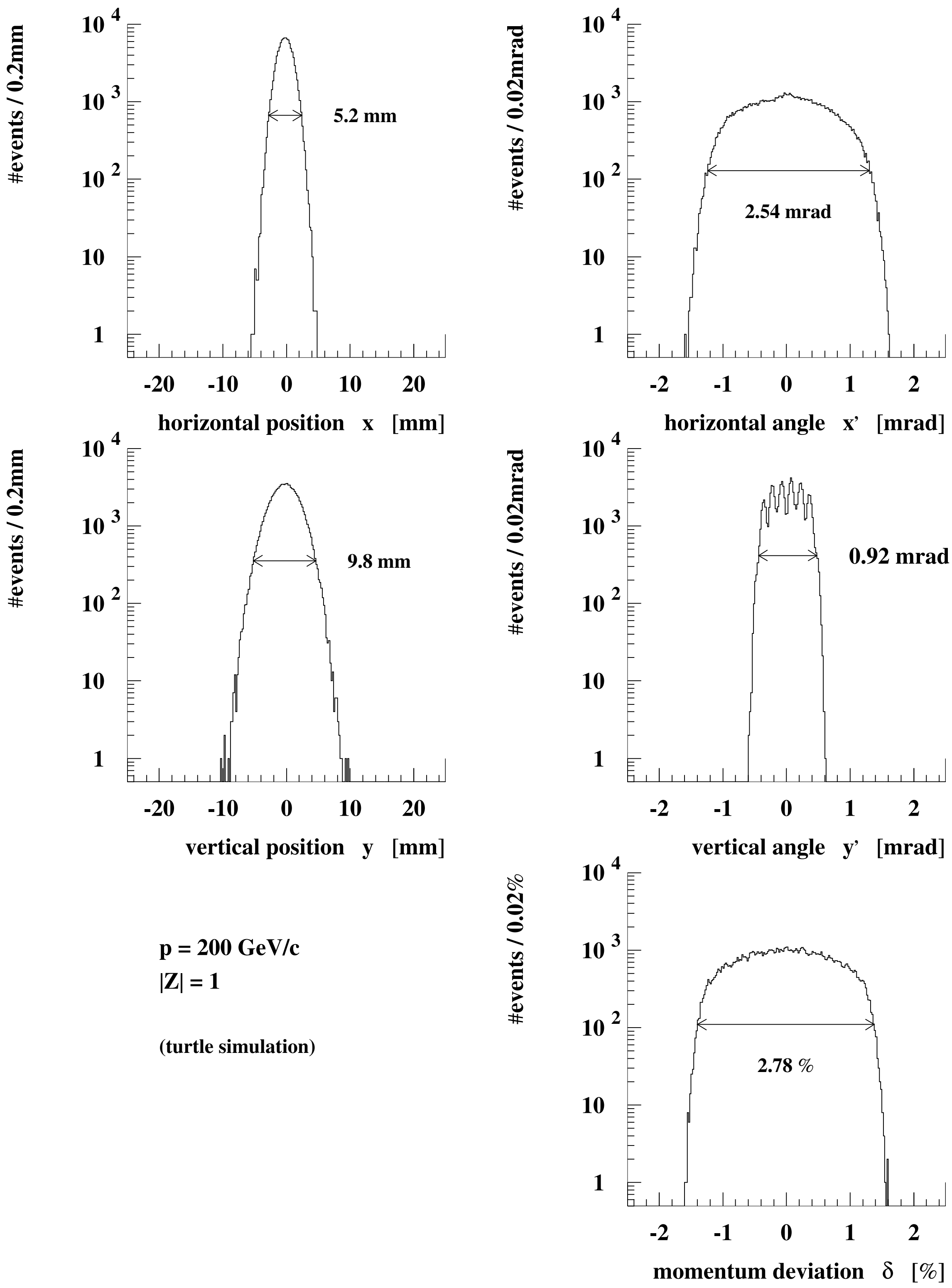

Figure 3.9: Simulation of the track fitting at 200 GeV/c. The shown distributions represent the phase space acceptance of the spectrometer at the target. The indicated numbers are full width one tenth maximum values of the phase space distributions.

Table 3.3: Momentum dependence of the fit resolution

p [GeV/c]	FW$\frac{1}{10}$M(x) [mm]	FW$\frac{1}{10}$M(x') [mrad]	FW$\frac{1}{10}$M(y) [mm]	FW$\frac{1}{10}$M(y') [mrad]	FW$\frac{1}{10}$M(δ) [%]
200	4.9	0.49	9.5	0.31	0.29
100	5.9	0.54	12.	0.37	0.36
40	9.7	0.75	19.	0.60	0.56
20	16.	1.2	34.	1.0	0.90
10	28.	2.1	61.	1.9	1.7
5	43.	3.2	90.	2.6	2.6

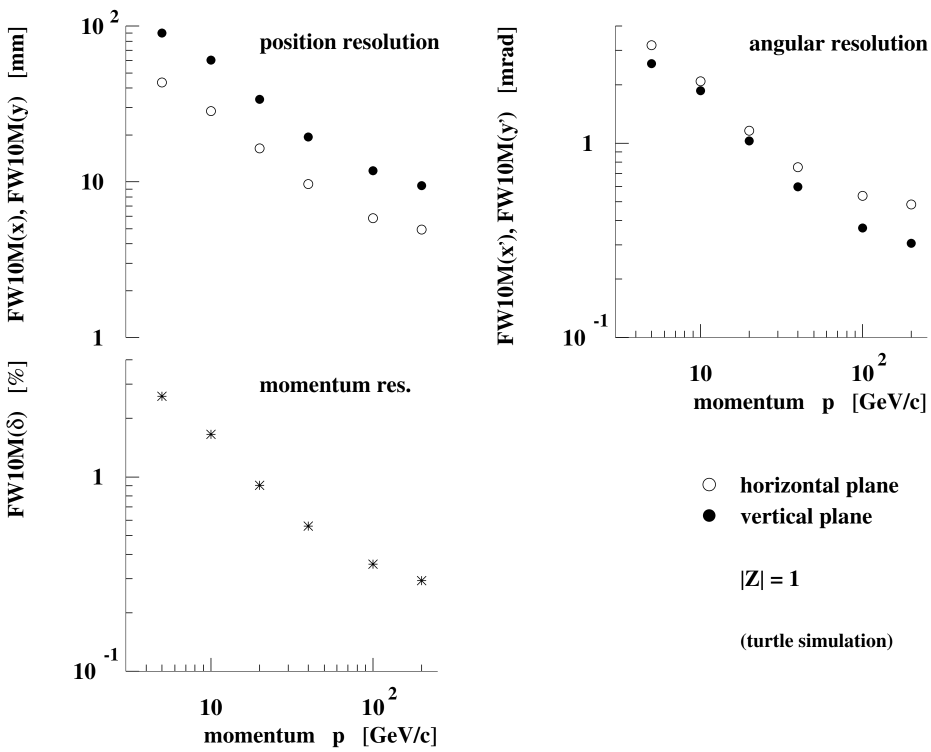

Figure 3.10: Simulated variation of the phase space reconstruction accuracy as a function of the particle momentum.

3.3.3.2 Track fitting on the lead data

The TURTLE simulation can be compared with the results from the measured secondaries in the Pb$-$Pb collisions. Fig. 3.11 shows an example of the rigidity setting $p/Z = -200\,\mathrm{GeV}/c$.

One remarkable point is the relative wide tails starting on the percent level of the phase space width. These might be particles which do not come from the target itself but origin from some secondary source like decaying kaons ($K^\pm \rightarrow \mu^\pm \overset{(-)}{\nu}_\mu$, $K^\pm \rightarrow \pi^\pm\pi^0$) or pions ($\pi^\pm \rightarrow \mu^\pm \overset{(-)}{\nu}_\mu$). Part of the tertiary $\mu^\pm$ or $\pi^\pm$ might still be kept within the acceptance of the beam line. The decay option of the TURTLE programme has not been used in the

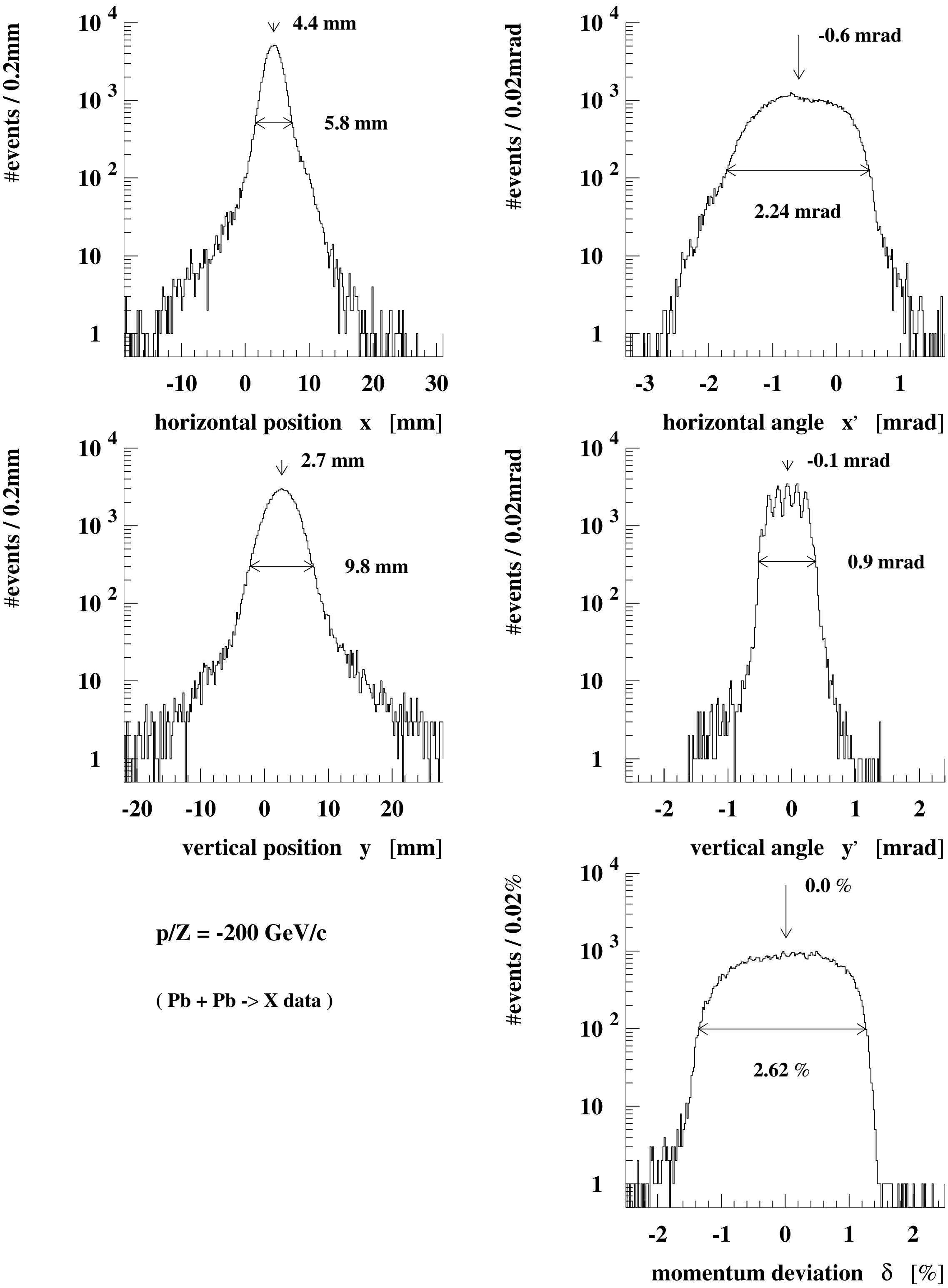

Figure 3.11: Example of the track fitting on $p/Z = -200\,\mathrm{GeV}/c$ data. The shown distributions represent the phase space acceptance of the spectrometer at the target. The indicated numbers are full width one tenth maximum values of the observed distributions.

simulation.

Finally it should be mentioned that an absolute position calibration of the wire chambers is still overdue, which could explain the systematic offsets of the beam positions at the target (Fig. 3.11). Well centered wire chambers have been assumed in the measurement, although a not centered beam by a few millimeters in W1T is visible.[11] However, the widths of the phase space distributions are not affected by this uncertainty.

3.3.3.3 Comparison between simulated and measured distributions of the phase space coordinates at the target

The obtained widths of the phase space distributions at the target and their comparison between simulation and measurements can be regarded as a test for the acceptance determination of the beam line. The comparison is summarized in Tab. 3.4 for some representative data samples probing a small fraction of the data taken.

The widths have been corrected according to the determined fit accuracies (*cf.* Tab. 3.3).

$$\Delta_{10} = \mathrm{FW}\frac{1}{10}\mathrm{M}\Big|_{\substack{\text{reconstructed}\\ \text{phase space}}} \ominus \mathrm{FW}\frac{1}{10}\mathrm{M}\Big|_{\text{fit resolution}} \tag{3.33}$$

Table 3.4: Comparison between measured and simulated phase space widths using the $\mathrm{FW}\frac{1}{10}\mathrm{M}$ values of the phase space based on the track reconstruction. The widths have been corrected for the measurement accuracy.

		up to TOF3				up to TOF5			
	p/Z [GeV/c]	$\Delta_{10}x'$ [mrad]	$\Delta_{10}y'$ [mrad]	$\Delta_{10}\delta$ [%]	$\Delta_{10}^{3}\Omega\delta$ [μsr%]	$\Delta_{10}x'$ [mrad]	$\Delta_{10}y'$ [mrad]	$\Delta_{10}\delta$ [%]	$\Delta_{10}^{3}\Omega\delta$ [μsr%]
abs. values data & simul	+200 (data)	./.	./.	./.	./.	1.93	0.75	2.55	3.69
	−200 (data)	2.19	0.85	2.61	4.86	2.17	0.85	2.60	4.80
	200 (simul)	2.49	0.87	2.76	5.98	2.49	0.87	2.76	5.98
		±0.05	±0.02	±0.05	±0.22	±0.05	±0.01	±0.05	±0.18
	+100 (data)	2.05	0.98	2.45	4.92	1.92	0.92	2.45	4.33
	−100 (data)	2.08	0.94	2.49	4.87	1.85	0.92	2.49	4.24
	100 (simul)	2.52	0.89	2.78	6.23	2.52	0.89	2.78	6.23
		±0.05	±0.02	±0.04	±0.21	±0.05	±0.02	±0.04	±0.21
rel. values data / simul		[%]	[%]	[%]	[%]	[%]	[%]	[%]	[%]
	+200	./.	./.	./.	./.	77	86	92	62
	−200	88	98	95	81	87	98	94	80
	+100	81	110	88	79	76	103	88	70
	−100	83	106	90	78	73	103	90	68

It can be observed that the measured widths are systematically smaller than the simulated widths. A possible interpretations of this result can be given:

- The acceptance of the beam line H6 for secondary particles is about 20−30% smaller than the TURTLE simulation suggests. These differences might be due to higher multiple Coulomb scattering losses than estimated in section 3.3.2, or due to the non-negligible use of a non-nominal beam optics (*cf.* section 3.2.3).

[11] In the meantime a surveying check of the wire chambers showed that W1T is shifted horizontally by 3 mm, private communication from K. Elsener, CERN-SL.

However, it should be emphasized that such a comparison between simulation and measurement involves the choice of the phase space distribution. In this first step flat momentum and angular distributions have been taken. A systematic study is still owing.

3.4 Summary of the acceptance calculation

The effective acceptance of the H6 beam line in the high transmission mode at high momenta using the results of the TURTLE simulation can be summarized in the numbers listed in Tab. 3.5. The mean acceptance in this region is $4.0 \cdot 10^{-8}$.

Table 3.5: Acceptance at high momenta

p [GeV/c]	up to TOF3 $\Delta^3\Omega\delta$ [μsr%]	up to TOF5 $\Delta^3\Omega\delta$ [μsr%]
200	4.07	3.99
100	4.03	3.90

The comparison of the transported phase space in the simulation and in the measurement using the track fitting method leads to the impression that the true acceptance of the beam line might be smaller. The observed discrepancy of 20 to 30% can be treated as an estimate of the systematic uncertainty of the knowledge of the true acceptance.

For particle production studies at low momenta a thorough comparison of simulation and measurements certainly needs further investigations, which go beyond this first, simple approach. Meanwhile these problems are investigated thoroughly by T. Lindén [Lindén96]. The key questions which have to be answered, if the losses due to multiple Coulomb scattering are parameterized appropriately and if an exact knowledge of the geometry and the placement of all beam line elements and detectors can be applied.

Chapter 4

Data processing

Calibration and analysis methods of the stored raw data to obtain the mass and charge of the secondary particles in the beam line H6 are explained in this chapter.

4.1 Calibration of the electronics channels

Besides the knowledge of the beam optics for track fitting purposes and a 'static' calibration of the calorimeter (*cf.* section 2.8, p. 23) a 'dynamic' calibration of all electronics channels is necessary to convert the digitized counts to physical meaningful numbers.

The basic calibration idea is, that the position of a peak in the different ADC, TDC and FPR distributions under various trigger conditions is a useful information to do the conversion to physical units. In detail these are:

- ADC pedestals of all subdetectors have to be known before a proper conversion to pulse heights can be done.
- `mip` positions are found in the ADC spectra of all scintillation counters and can be used to normalize the specific energy loss: After a conversion to `mip` units the numbers are approximately proportional to the square of the charge of a single particle.
- The uranium noise gives information about the current gain of the calorimeter channels. A proper energy measurement can only be done with this information.
- TDC peak positions of fast particles serve as 't_0' values with respect to which a time delay measurement of slower particles is done.
- TDC peak positions obtained from a 100 MHz quartz oscillator allow to calculate the individual conversion factor from TDC counts to time for each TDC channel.
- The position of the trigger particle in the future-past register defines the reference point for earlier and later particles.

The medians and widths of all these peak positions are dynamically calculated based on the raw data in restricted windows of appropriate boarders. Furthermore, the hit rate, *i. e.* the fraction of values which fall into the window, is calculated for verification purposes.

All values are updated eventwise and can be displayed spillwise in order to monitor slight drifts in the gain of the channels.

Fig. 4.1 shows an example of a pulse height distribution in a single channel of a TOF slab and the obtained `mip` peak, Fig. 4.2 shows an example of a time of flight distribution in a single channel of a TOF slab and the obtained t_0 position of fast trigger particles. Usually all these values are relatively constant. Largest fluctuations have been observed in the channels of the quartz counter since the linear gates are quite sensitive to temperature variations. This is shown in Fig. 4.3, monitoring the pedestal peak of one of the ADC channels. Although the peak moves several counts per hour, this update mechanism can keep track of the variations.

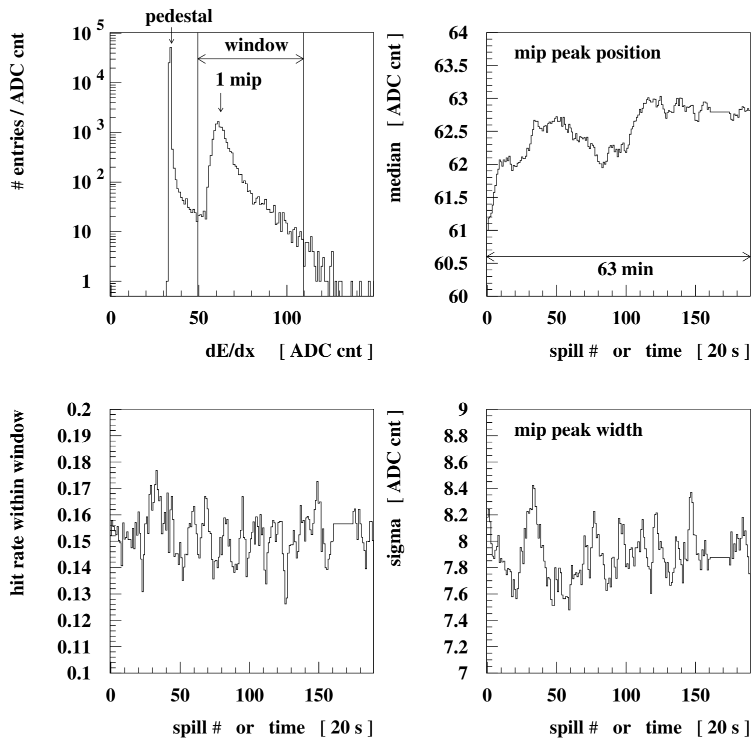

Figure 4.1: The calibration of a `mip` peak (TOF1-4B)

The formulae used to update the mean peak position $\langle cnt \rangle$, its width σ and the hit rate h within the *window* given a new value (`cnt`) are:

$$\langle cnt \rangle_{e+1} = \langle cnt \rangle_e + \begin{cases} 0 & : \ \mathtt{cnt} \notin window \\ \sigma_e \cdot v & : \ \mathtt{cnt} > \langle cnt \rangle \\ -\sigma_e \cdot v & : \ \mathtt{cnt} < \langle cnt \rangle \end{cases} \tag{4.1}$$

$$\sigma_{e+1} = \begin{cases} \sqrt{(1-v) \cdot \sigma_e^2 + v \cdot [\mathtt{cnt} - \langle cnt \rangle_e]^2} & : \ \mathtt{cnt} \in window \\ \sigma_e & : \ \text{otherwise} \end{cases} \tag{4.2}$$

$$h_{e+1} = h_e \cdot (1-v) + \begin{cases} v & : \ \mathtt{cnt} \in window \\ 0 & : \ \text{otherwise} \end{cases} \tag{4.3}$$

with $e =$ event counter

$v = 0.001 \ldots 0.01$ as the update weight

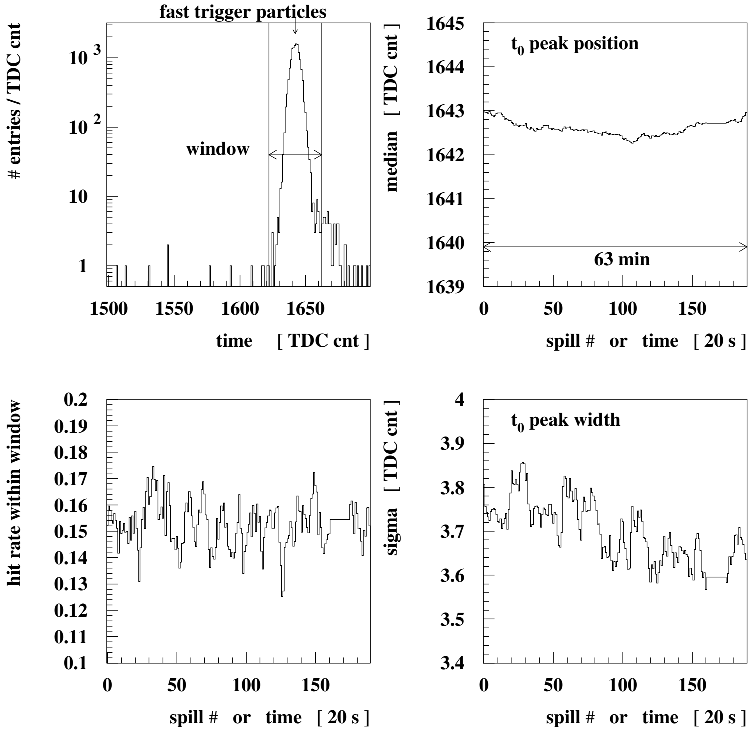

Figure 4.2: The calibration of a t_0 peak (TOF1-4B)

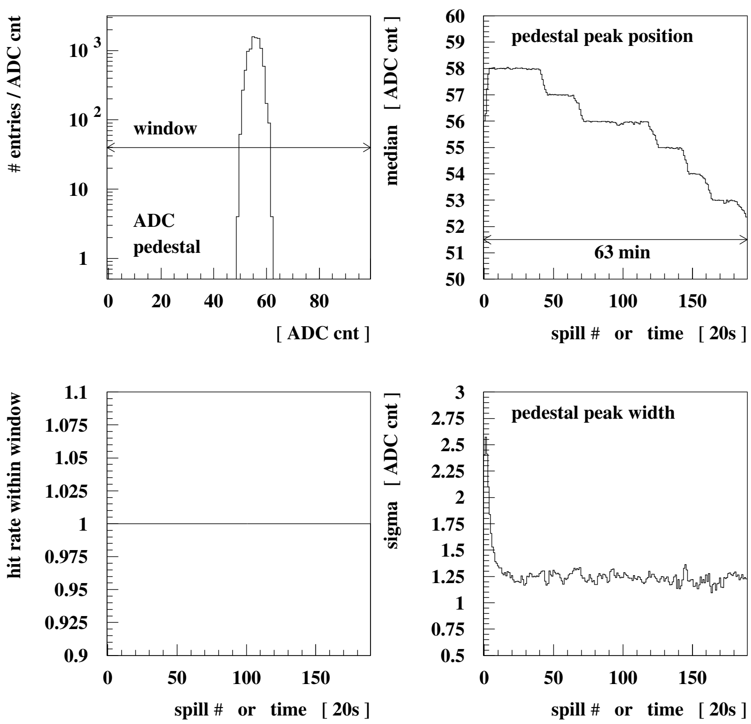

Figure 4.3: The calibration of an ADC pedestal peak (TOF0-1B)

Spill pauses are used to send regularly TDC stops to the individual TDC channels with 10 ns time difference changes in order to check the conversion between TDC counts and seconds. Fig. 4.4 shows an example of accumulated calibration stops in one TDC channel.

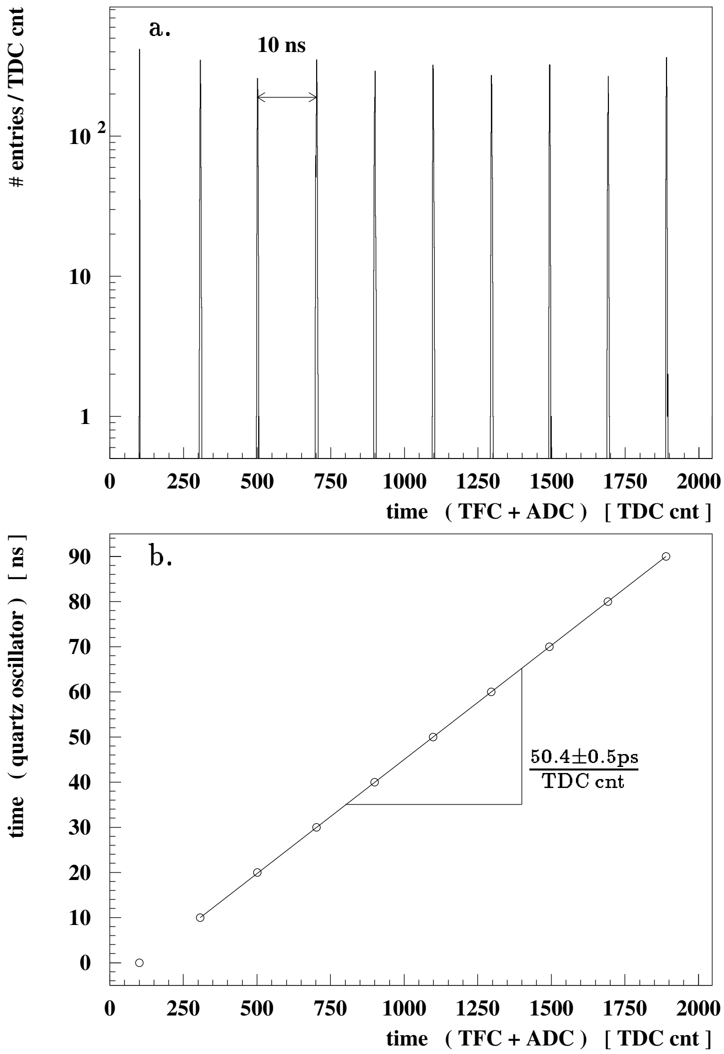

Figure 4.4: The calibration of the conversion factor of a TDC channel (TOF1-4B)

Each of the ten individual peak positions (Fig. 4.4a) is obtained in the same way as for the ADC pedestal peaks. Fig. 4.4b shows the correlation between the TDC peak position and the time delays triggered based on a 100 MHz quartz oscillator. A linear fit to the set of points allows to extract a mean conversion factor (*slope*). In this example one gets 50.3 ± 0.4 ps/ `cnt`. Points below 250 TDC counts have been excluded from the fit, since there the linearity of the TDC is in general not well defined. This limits the usable TDC range to about 80 ns.

The obtained peak positions and gain factors are applied in the following way:

- All energy loss measurements (`cnt`) in the scintillation counters are converted to normalized **mip** values as

$$\frac{\mathrm{d}E/\mathrm{d}x}{\mathtt{mip}} = \frac{\mathtt{cnt} - \langle ped \rangle}{\langle cnt \rangle - \langle ped \rangle} \tag{4.4}$$

- All TDC times (**cnt**) are t_0 ($= \langle cnt \rangle$) subtracted and converted to a time in common units (*e. g.* nanoseconds) as

$$time = (\mathtt{cnt} - \langle cnt \rangle) \cdot slope \tag{4.5}$$

- The energy of each calorimeter channel can be calculated as

$$energy = f_{calib} \cdot \frac{\mathtt{cnt} - \langle ped \rangle}{\langle UNO \rangle - \langle ped \rangle} \tag{4.6}$$

  where f_{calib} is the appropriate calibration factor and $\langle UNO \rangle$ the actual uranium noise value (*cf.*section 2.8).

Based on these calibrated values a reconstruction of the events has been tried to search for strangelet candidates.

4.2 Mass and charge determinations

Each time of flight measurement yields a time delay Δt relative to the known arrival time of an abundant light particle species with mass m_0 (*e. g.* pions), momentum p_0 and velocity β_0. In each event, the available TOF measurements Δt_i are combined to provide a consistent value for

$$\left\langle \frac{\Delta t}{\Delta L} \right\rangle = \frac{1}{c} \left(\frac{1}{\beta} - \frac{1}{\beta_0} \right) \tag{4.7}$$

which depends on the velocities β of the particle. Practically this is realized by a linear least square fit to the data points $(L_i, \Delta t_i)$, where L_i is the distance of the TOF hodoscope from the target. Thereafter, the slope of the fit line represents the mean relative time delay $\langle \Delta t / \Delta L \rangle$ and it determines the mass to charge ratio of the particle via

$$\left(\frac{m}{Z} \right)^2 = \left(\frac{p}{Z} \right)^2 \left[\left(\left\langle \frac{\Delta t}{\Delta L} \right\rangle + \sqrt{\frac{1}{c^2} + \left(\frac{m_0}{p_0} \right)^2} \right)^2 - \frac{1}{c^2} \right] \tag{4.8}$$

The timing of the detector signals and the dynamic range of the TDC modules allow relative slopes $0 < \langle \Delta t / \Delta L \rangle < 0.18/c$, corresponding to $0.85 \lesssim \beta < 1$, if $\beta_0 = 1$. This implies at $p/Z = \pm 100\,\mathrm{GeV}/c$, that the detectable range covers $m/|Z| < 60\,\mathrm{GeV}/c^2$, while at $\pm 200\,\mathrm{GeV}/c$ the $m/|Z|$ range goes up to $120\,\mathrm{GeV}/c^2$.

In the ultrarelativistic limit ($m_0 \ll p_0/c$, $\langle \Delta t / \Delta L \rangle \ll 1/c$) Eq. (4.8) simplifies to

$$\left(\frac{m}{Z} \right)^2 \approx \frac{2}{c} \left(\frac{p}{Z} \right)^2 \left\langle \frac{\Delta t}{\Delta L} \right\rangle \tag{4.9}$$

i. e. the mass to charge ratio of a particle scales with the square root of the slope in the fit.

The consistency of the fit can be checked by calculating its χ^2 value:

$$\frac{\chi^2}{ndf} = \frac{1}{N_{\mathrm{TOF}} - 2} \sum_{i=1}^{N_{\mathrm{TOF}}} \left[\frac{\Delta t_i - \left\langle \frac{\Delta t}{\Delta L} \right\rangle \cdot L_i - \langle \Delta t_0 \rangle}{\sigma_{\Delta t_i}} \right]^2 \tag{4.10}$$

where $\sigma_{\Delta t_i}$ is the time resolution of the corresponding TOF hodoscope, N_{TOF} is the number of involved TOF hits, ndf the number of degrees of freedom $= N_{\mathrm{TOF}} - 2$, $\langle \Delta t_0 \rangle$ is the extrapolation of the mean time delay at the target, derived from the fit procedure. For unbiased measurements with Gaussian resolutions the χ^2 value itself is distributed as chi-squared with mean ndf and variance $2 \cdot ndf$. In the time of flight analysis it was practically found, that values $\chi^2/ndf < 3$ represent consistent fits with a small inefficiency on the percent level.

Fig. 4.5 shows an example of the realization of the linear fit including all TOF hodoscopes for an event taken at $-100\,\mathrm{GeV}/c$.

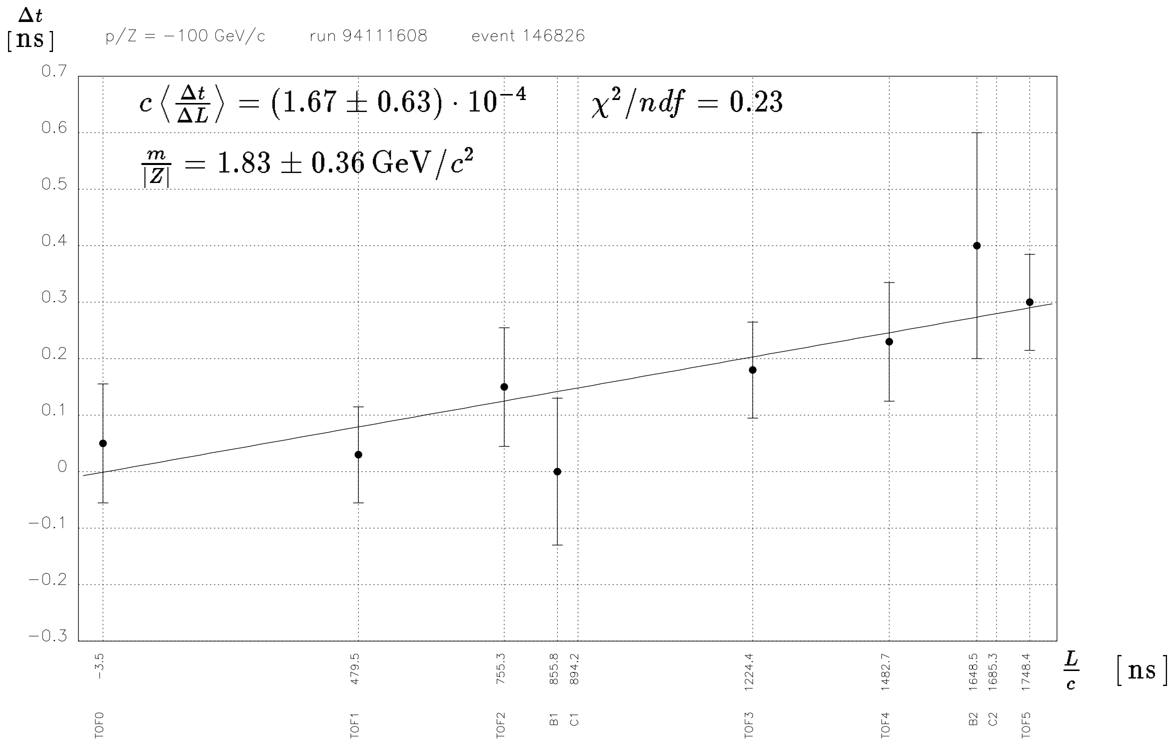

Figure 4.5: Example of a TOF fit resulting from an event at $-100\,\mathrm{GeV}/c$. It can be identified as an antideuteron.

The relative slope is equal to $\langle \Delta t/\Delta L \rangle = (1/c)(1.67 \pm 0.63) \cdot 10^{-4}$ or to a mass to charge ratio of $m/|Z| = (1.83 \pm 0.36)\,\mathrm{GeV}/c^2$. That is compatible with an antideuteron or an antihelium-4. The alternatives can only be decided by looking at the energy loss measurements; in this event this information is compatible with a singly charged particle.

The effective time of flight resolution for TOF0-3 is about 120 ps and 100 ps for TOF0-5.

Combining the energy loss measurements derived from the TOF hodoscopes allows to determine the charge number of the passing particle, since the mean energy loss is proportional to the charge square of the particle:

$$\langle \mathrm{d}E/\mathrm{d}x \rangle \quad \propto \quad Z^2/\beta^2 \tag{4.11}$$

The $\mathrm{d}E/\mathrm{d}x$ measurements usually suffer from two problems. On the one hand Landau fluctuations of the ionization process can lead to rather high values, while on the other hand in case of grazing shots[1] the effective path length in the scintillator is reduced and the $\mathrm{d}E/\mathrm{d}x$ measurement yields smaller values. Several methods have been tried to get rid of these uncertainties. The chosen method is a cluster algorithm: The obtained $\mathrm{d}E/\mathrm{d}x$ values from the TOF hodoscopes are sorted, smallest and highest value are removed from this list and the remaining values are used to calculate their median, which is a good approximation for the most probable value of the measured points. Practical realization of this algorithm will be described by P. Hess [Hess96]. Of course this method works best if one has got a lot measurement points.

Plots of charge distributions are shown later.

Data taken at low rigidities can serve as a check for the principle operation of the particle separation by their time of flight. Fig. 4.6 shows an example of the time of flight fit for particles at a secondary rigidity of $+10\,\mathrm{GeV}/c$.

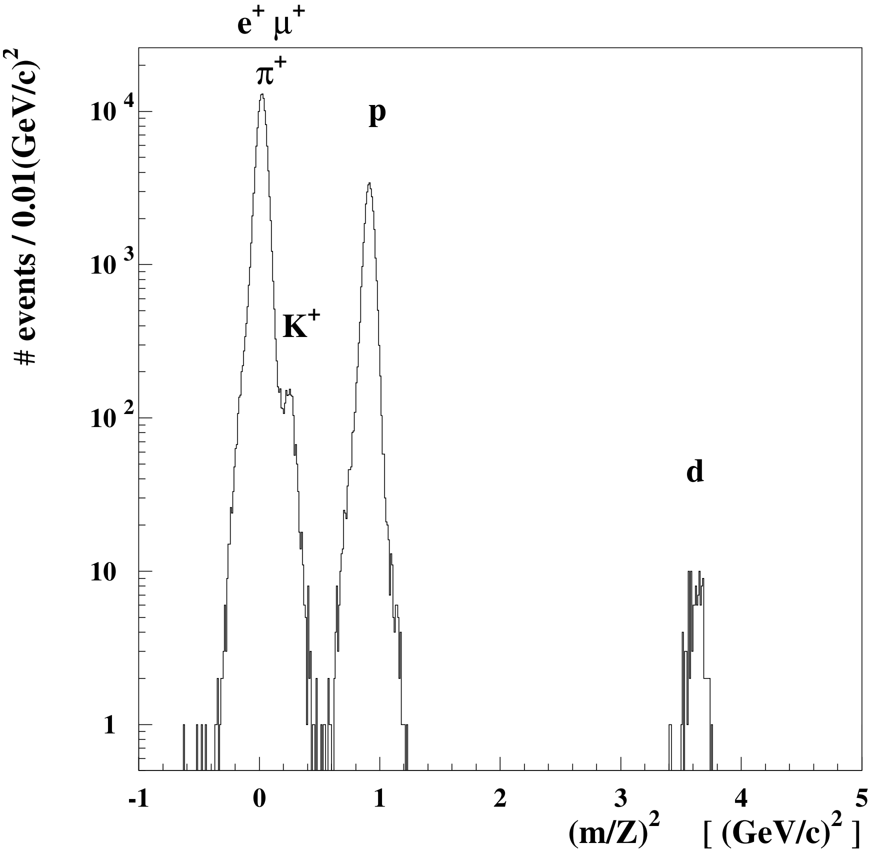

Figure 4.6: $(m/Z)^2$ spectrum which demonstrates the particle identification capabilities with the time of flight measurements, here at a low rigidity $p/Z = +10\,\mathrm{GeV}/c$. The width of the distributions reflect the resolution of the time of flight fit. On the m^2 scale it has a value of $\sigma_{m^2} = 0.04(\,\mathrm{GeV}/c^2)^2$ and the corresponding mass resolutions are $\sigma_\pi = 140\,\mathrm{MeV}/c^2$, $\sigma_\mathrm{K} = 40\,\mathrm{MeV}/c^2$, $\sigma_\mathrm{p} = 20\,\mathrm{MeV}/c^2$, $\sigma_\mathrm{d} = 10\,\mathrm{MeV}/c^2$.

The groups of protons and deuterons are well separated from the lighter particle species.

[1]A term introduced by W. Volken [Volken94].

Furthermore, under these kinematic conditions the K^+ distribution can be distinguished from the abundant light particle group, which contains π^+, e^+ and μ^+. In the shown data sample no particle with charges $Z > 1$ has been found.

At higher rigidities the velocity differences between the particle groups become smaller, the visible mass spectrum broadens and the peaks for the particles shown in Fig. 4.6 melt into one another. At 100 GeV/c and 200 GeV/c, which are the relevant rigidities for the strangelet search, particles with mass to charge ratios larger than about 5 to 10 GeV/c^2 could become separated from the "light" group which contains known particles up to deuterons or helium nuclei.

4.3 Analysis tools

4.3.1 Reconstruction programme

A general purpose programme has been written which implements the calculations discussed for the calibration, energy, mass, charge and track determination for the recorded events.

Central part in this programme is the time of flight fit in order to look for strangelet candidates, *i. e.* events with a high mass to charge ratio. Once interesting events have been found, a closer look at the event topology is done by visualizing the hit pattern in the individual subdetectors.

4.3.2 Event displays

The whole analysis has been done in an iterative way where the reconstruction methods and applied cuts have been improved in a successive way. Individual events, especially those which seem to contain contradictory information or seem to be possible strangelet candidates, have been checked by producing event displays, *i. e.* plotting the whole raw data information of an individual event in a graphical way.

Part of an event display is the time of flight fit, as already presented in Fig. 4.5. Further information about the hits in the future-past registers and the wire chamber complete the picture of an event. A few examples of event displays are shown and discussed in the following chapters (6 and 7) on results.

Chapter 5

Particle rates

The rate of incident lead ions onto the target as seen by the quartz Čerenkov counter is investigated. Consequences of the observed characteristic spill structure are discussed. Furthermore, typical secondary particle rates as seen in the beam line are summarized.

5.1 About the spill structure of the incident lead ions

The incident lead ions are registered with the help of the quartz counter (TOF0). For this purpose the discriminated signals of these counters are fed into CAMAC scalers with 100 MHz bandwidth, which are read spillwise, independent of the event triggers. In addition a second set of scalers allows to count the lead ions during the live time of the DAQ. From this one might conclude the effective live time of the data acquisition system. Typical live times of the DAQ are better than 90%. All hereafter quoted lead ion numbers are derived from the scaler which counts only during the live time of the data acquisition.

The counting rate of the quartz segments are limited by the double pulse resolution of the discriminators. This time was measured in a test setup to be 7 ns (*cf.* section 2.4.2).

A rough estimation about the systematic miscounting of lead ions under consideration of the lead ion rates and its observed variations are given.

5.1.1 The analog read-out

The analog read-out of the quartz Čerenkov counter allows to distinguish between single and multiple lead ions within the same ADC gate of a single quartz segment. Fig. 5.1 shows an example of lead ion multiplicities obtained from the pulse height distribution of the quartz counter.

5.1.2 The future-past register

The future-past register connected to the quartz Čerenkov counter allows to measure properties of the spill structure of the incident lead ions. Fig. 5.2 is the distribution of the slot numbers seen by one quartz counter channel.

The peak corresponds to the lead ion which did an interaction in the target producing a secondary particle triggering in the beam line. The shape of the distribution, *i. e.* the

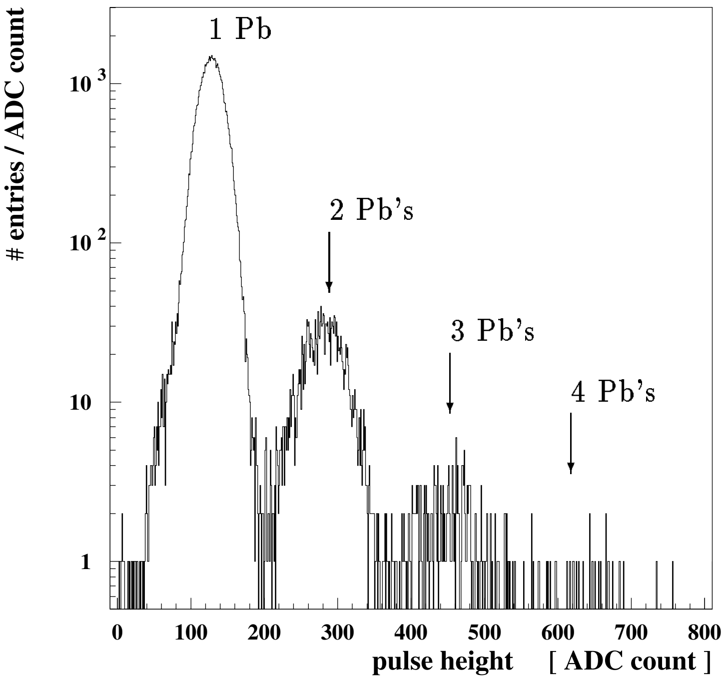

Figure 5.1: Multiplicity distribution of lead ions obtained from the analog signals of the quartz counter segments

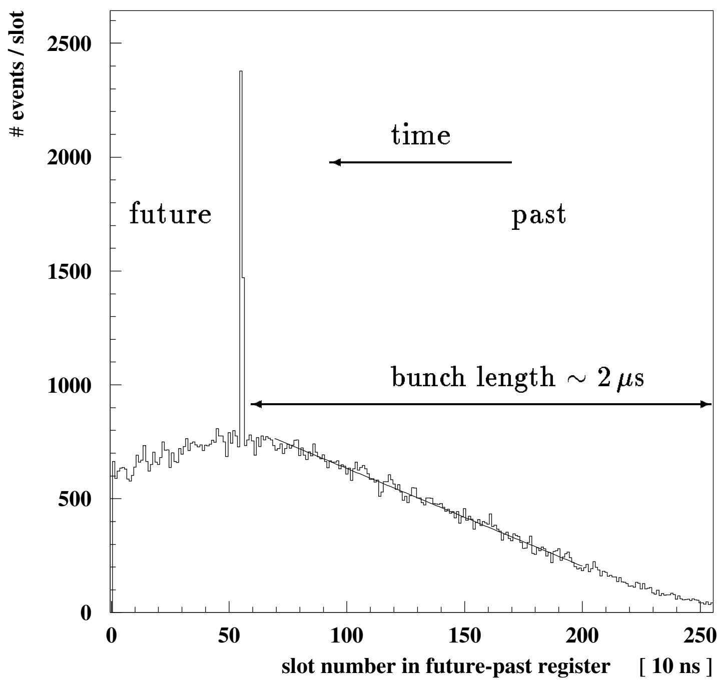

Figure 5.2: Distribution of hits in the future-past register of one channel of the quartz Čerenkov counter

decreasing flanks, can be explained by bunches of lead ions. The time difference between the maximum point and the zero-crossing of the shape defines the bunch length. One can easily see from Fig. 5.2 that this length is $2\,\mu$s. Independent but corresponding observations have been done by measuring the time structure of the anode current of the photomultipliers of the quartz counter[1].

Furthermore, Fig. 5.3 shows the multiplicity distribution of lead ions within $2.55\,\mu s$ using all channels of the future-past register of the quartz counter.

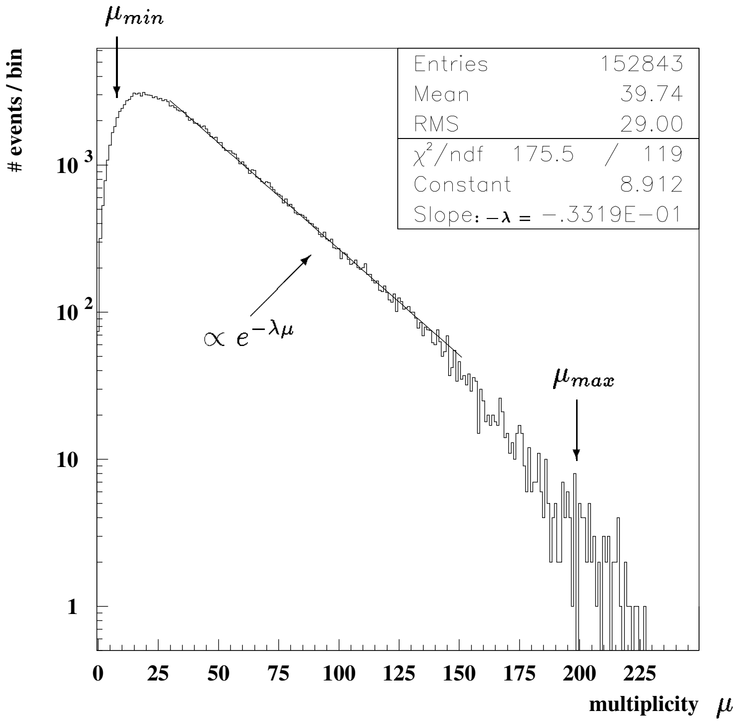

Figure 5.3: Multiplicity distribution of lead ions within $2.55\,\mu$s as registered with the future-past register of the quartz counter, sampled over 150'000 events

5.1.3 A simple spill structure model

To explain the shapes as seen with the future-past registers the following spill structure model has been developed: The lead ions are delivered in bunches à $2\,\mu$s, repeated every $5\,\mu$s. This corresponds to a duty cycle of $2\,\mu\text{s}/5\,\mu\text{s} = 40\%$. Within one bunch the lead ions are distributed according to a Poisson statistics, but from bunch to bunch the mean rate might vary. This mean rate is distributed like an exponential distribution with a lower and upper mean rate limitation.

Within this model the observed multiplicity of lead ions (*cf.* Fig. 5.3) can be expressed as

$$n(r,\lambda) = \int_{\mu_{min}}^{\mu_{max}} e^{-\lambda\mu} \frac{e^{-\mu}\mu^r}{r!} \mathrm{d}\mu \tag{5.1}$$

[1]Private communication from K. Borer, University of Bern

where r is the observed multiplicity, while λ describes the exponential decrease of the mean rate. In the case of $\mu_{min} \to 0$ and $\mu_{max} \to \infty$ the integral 5.1 can be solved analytically and the multiplicity distribution yields a pure exponential

$$n(r, \lambda) \to \exp\left(-(r+1)\ln(\lambda+1)\right) \tag{5.2}$$

The finite value of μ_{min} reflects the observed gap at very low multiplicities of Fig. 5.3 while the finite μ_{max} cuts on very high multiplicities.

Based on this model one can calculate the amount of lead ions which are not resolved by the discriminator due to its limited double pulse resolution. With the pulse height information one can distinguish between single and multiple lead ions (*cf.* Fig. 5.1), but that information is only available for triggered and recorded events which represent a small fraction of the incident lead ions.

A simple simulation using the spill structure with

$$\lambda = 0.033, \quad \mu_{min} = 8, \quad \mu_{max} = 200 \tag{5.3}$$

yields in this example a multiplicity distribution of lead ions within 7 ns as shown in Fig. 5.4. It quantifies the number of not countable lead ions: In each bin with multiplicity

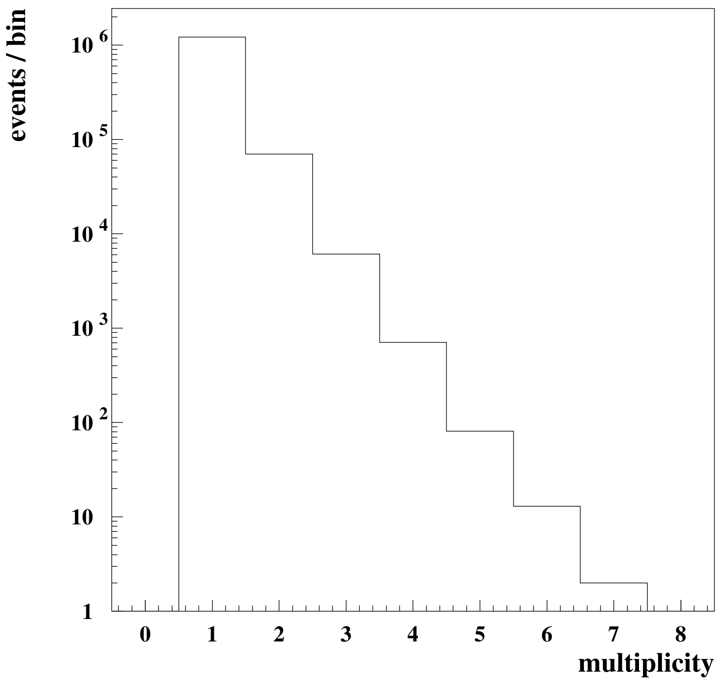

Figure 5.4: Simulation of the multiplicity distribution of lead ions within the double pulse resolution of 7 ns of the quartz counter signals

larger than one only one lead ion is registered by the scalers of the read-out electronics, although several lead ions have traversed "simultaneously" a common segment of the quartz counter. In the shown example 6% of the lead ions are missed. This value is true for mean lead ion rates of about $3 \cdot 10^7$ per spill and it increases to about 10% for the observed mean intensities of $6 \cdot 10^7$ per spill. In some situations the registered maximum multiplicities even increased to 300 lead ions within the window of the future-past register. In those situations the miscounting is 17%.

5.2 Secondary particle rates

The secondary particle rates vary quite characteristically with the chosen beam line rigidity and polarity. Tab. 5.1 summarizes the mean intensities of lead ions and of the secondary particles as observed by the trigger coincidence B1·TOF2.

Table 5.1: Typical particle fluxes, which have been observed during data taking

p/Z [GeV/c]	l_{target} [mm]	$\left\langle \frac{N_{\mathrm{Pb\,ion}}}{\mathrm{spill}} \right\rangle$	$\left\langle \frac{N_{\mathrm{B1 \cdot TOF2}}}{\mathrm{spill}} \right\rangle$	$\frac{\mathrm{particle}}{\mathrm{interaction}}$
-200	40	$4 \cdot 10^7$	$4.5 \cdot 10^2$	$2 \cdot 10^{-5}$
-100	40	$3 \cdot 10^7$	$1 \cdot 10^4$	$5 \cdot 10^{-4}$
$+100$	40	$6 \cdot 10^7$	$2.5 \cdot 10^5$	$7 \cdot 10^{-3}$
$+200$	16	$4 \cdot 10^7$	$5 \cdot 10^5$	$4 \cdot 10^{-2}$

On the one hand the mean lead intensities were varying more than a factor two during the data taking period of three weeks, on the other hand one can clearly observe an increase of the secondary rate with the beam line rigidity.

It should be emphasized that mean numbers per spill are quoted in Tab. 5.1, but instantaneous rates of secondary particles are also subject to the spill fine structure. Thus, peak intensities can be easily an order of magnitude higher.

5.3 Particle multiplicities in the beam line

Although the H6 beam line is a so-called "single particle" focusing spectrometer it can not be excluded to record data from two different particles within the same read-out gates of a single trigger. Usually these two particles origin from two different lead-lead interactions which happened close in time.

Appropriate instruments to count particle multiplicities in the beam line are the segmented TOF planes. Two examples of the observed multiplicities in TOF3 at -100 and $+200\,\mathrm{GeV}/c$ are shown in Fig. 5.5.

The level of multiple hit events in the case of $-100\,\mathrm{GeV}/c$ is about 2% and at $+200\,\mathrm{GeV}/c$ 6%. This can be compared with the expectation values assuming perfect Poisson statistics and an ideal spill without any internal time structure. One would get a double particle contamination of

$$\frac{P(\text{at least two particles within TDC gate})}{P(\text{at least one particle within TDC gate})} = \frac{1 - e^{-\lambda T} - \lambda T e^{-\lambda T}}{1 - e^{-\lambda T}} \approx \frac{\lambda T}{2} \approx 8 \cdot 10^{-5} \quad (5.4)$$

at $\lambda = 1 \cdot 10^{-4}/5\,\mathrm{sec}$, $T = 80\,\mathrm{ns}$ for $p/Z = -100\,\mathrm{GeV}/c$ and $\lambda T/2 = 4 \cdot 10^{-4}$ at $\lambda = 5 \cdot 10^5/5\,\mathrm{sec}$ for $p/Z = +200\,\mathrm{GeV}/c$, which is in both cases two orders of magnitude smaller than the observed values.

Only events with a valid downstream trigger are shown in the distributions of Fig. 5.5. Thus, one can derive from this picture the inefficiency of detecting a particle in a single TOF hodoscope by looking at the fraction of events with zero multiplicity. At both shown

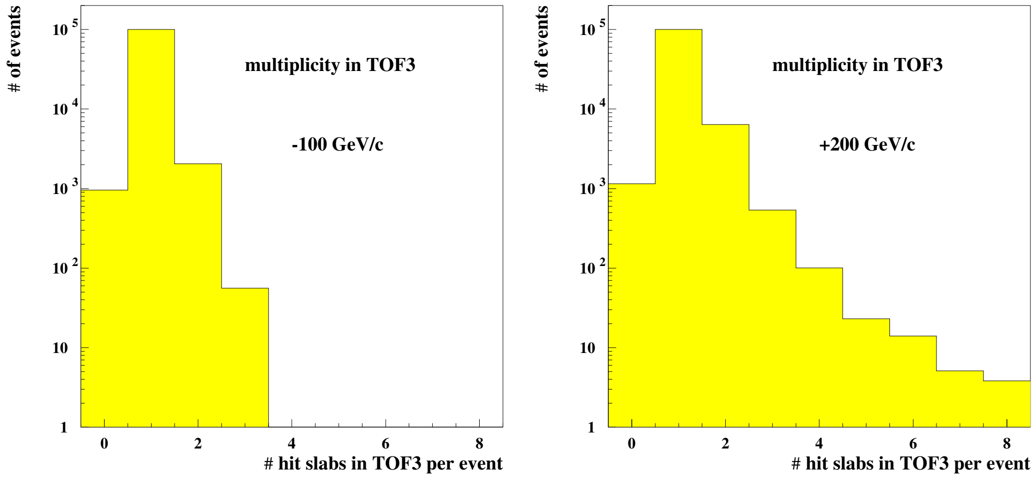

Figure 5.5: Multiplicity distribution in TOF3 at -100 and $+200\,\mathrm{GeV}/c$

rigidities it is consistently 1%. Similar values have been observed in the TOF planes 1 and 5.

The efficiencies of TOF2, TOF4 and of the unsegmented scintillation counters B1 and B2 cannot be derived from the recorded data itself. But one can assume that those inefficiencies are not worse, and therefore the trigger efficiencies B1·TOF2 and B2·TOF4 should be better than 98%.

Chapter 6

Discussion of the data taken at the negative magnetic rigidities $p/Z = -100$ and $-200\,\mathrm{GeV}/c$

The data taken at the two rigidity settings -100 and $-200\,\mathrm{GeV}/c$ allow to give limits on the production of heavy, negatively charged particles. Furthermore different chosen pressure values of the threshold Čerenkov and CEDAR counters allow to determine the particle yields of antinuclei, namely antiprotons and antideuterons at forward rapidities $y_{\mathrm{lab}} = 4.7$ and 5.4.

6.1 Overview of the analyzed settings

A 40 mm lead target, corresponding to one hadronic interaction length, was chosen in all runs.

At $-100\,\mathrm{GeV}/c$ runs were taken under the trigger condition B1·TOF2·$\overline{\check{\mathrm{C}}1}$, *i. e.* only the upstream part was required and fast particles were vetoed with the aid of the first Čerenkov counter. A small fraction of light particles were taken for calibration purposes. The pressure in Č1 was chosen to suppress the recording of particles with a mass to charge ratio smaller than that of $\overline{^{3}\mathrm{He}}$, and the one of the second Čerenkov counter marked particles lighter than antideuterons, while the CEDAR tagged antiprotons.

The data taking period at $-200\,\mathrm{GeV}/c$ can be subdivided into two parts:

In a first period short data samples, each containing data from about 10^{10} Pb$-$Pb interactions, were taken. The up- and downstream part of the spectrometer was included in the trigger, *i. e.* a coincidence between B1, TOF2, B2 and TOF4 was required to trigger an event. Events were not vetoed by the Čerenkov counters. Different pressure value were chosen to tag particles with mass to charge ratios smaller than that of $\overline{\mathrm{p}}$, $\overline{^{3}\mathrm{He}}$, $\overline{\mathrm{d}}/\overline{^{4}\mathrm{He}}$ and $\overline{\mathrm{t}}/\overline{^{6}\mathrm{He}}$, respectively. But due to the low production probability of antinuclei, in this accumulated statistics neither an antideuteron nor any heavier particle could be identified. However, this data could be used to do an efficiency scan of the threshold Čerenkov counters. The results of this technical aspect have already been described in section 2.7.1.

In a second period a much higher statistics ($N_{\mathrm{Pb\,ion}} = 1.9 \cdot 10^{11}$) has been accumulated with the relaxed trigger condition B1·TOF2, which serves as the resource for the strangelet search. In a smaller fraction of this data sample Čerenkov counter Č1 tags particles with mass to charge ratios less than that of $\overline{\mathrm{p}}$, while in a larger fraction the Čerenkov counters discriminate between $\overline{\mathrm{d}}/\overline{^4\mathrm{He}}$ and faster particles. In part of the statistics antideuterons can be cross checked with the aid of the CEDAR.

Tab. 6.1 summarizes the accumulated statistics of the various settings.

Table 6.1: Overview of the settings at the negative rigidities

p/Z	trigger	Čerenkov Č1 [mbar]	Čerenkov Č2 [mbar]	CEDAR tags	$N_{\mathrm{Pb\,ion}}$ [10^{11}]	N_{event} [10^6]
$-100\,\mathrm{GeV}/c$	B1·TOF2·$\overline{\text{Č1}}$	$< \overline{^3\mathrm{He}}$	$< \overline{\mathrm{d}}/\overline{^4\mathrm{He}}$			
		303	496		0.52	0.84
		303	496	$\overline{\mathrm{p}}$	1.20	1.38
					1.72	2.22
$-200\,\mathrm{GeV}/c$	B1·TOF2·B2·TOF4	— $< \overline{^3\mathrm{He}}$ —				
		83	82		0.09	0.07
		— $< \overline{\mathrm{d}}/\overline{^4\mathrm{He}}$ —				
		106	106		0.14	0.10
		143	139		0.24	0.17
		— $< \overline{\mathrm{t}}/\overline{^6\mathrm{He}}$ —				
		308	296		0.23	0.18
	B1·TOF2	$< \overline{\mathrm{p}}$	$< \overline{\mathrm{d}}/\overline{^4\mathrm{He}}$			
		34	133	$\overline{\mathrm{d}}/\overline{^4\mathrm{He}}$	0.34	0.35
		— $< \overline{\mathrm{d}}/\overline{^4\mathrm{He}}$ —				
		132	132		0.33	0.36
		132	132	$\overline{\mathrm{d}}/\overline{^4\mathrm{He}}$	1.28	1.39
					1.60	1.75

6.2 Discussion of the setting $p/Z = -100\,\mathrm{GeV}/c$

The setting at $-100\,\mathrm{GeV}/c$ is taken as an example for the discussion of the analysis method. The $-200\,\mathrm{GeV}/c$ settings are summarized more briefly in section 6.3.

6.2.1 General remarks

The time of flight fit is performed by including the calibrated TDC values obtained from hodoscopes TOF1-5 and the quartz counter TOF0. Each station may contribute up to one measurement point to the fit procedure. In case of multiple hits in one or more TOF stations, the fit is performed with all possible hit combinations. The search for the "right" combination is based on the χ^2 value of the fit. The one with the smallest χ^2 per degree of freedom (χ^2/ndf) is claimed to be the best guess for the event reconstruction. In order to account for accidental hits, at most one TOF station may be removed from the fit to check if the χ^2/ndf value improves.

The trigger mechanism delivers two different event classes:

Most of the time the trigger condition reads B1·TOF2·$\overline{\check{C}1}$, *i. e.* only events which are not vetoed by the first Čerenkov counter are recorded. Events belonging to this group will be called the *strangelet data sample*, since one expects to see heavy particles in this group.

During data taking every 10 ms the active veto of the Čerenkov counter is removed from the trigger. Independently of the Čerenkov signal the trigger condition reads B1·TOF2. Events belonging to this group represent the *natural particle spectrum.*

Characteristics of both data samples are discussed.

6.2.2 Natural particle spectrum

Fig. 6.1a shows the $(m/Z)^2$ distribution obtained on a subsample of the natural particle spectrum.

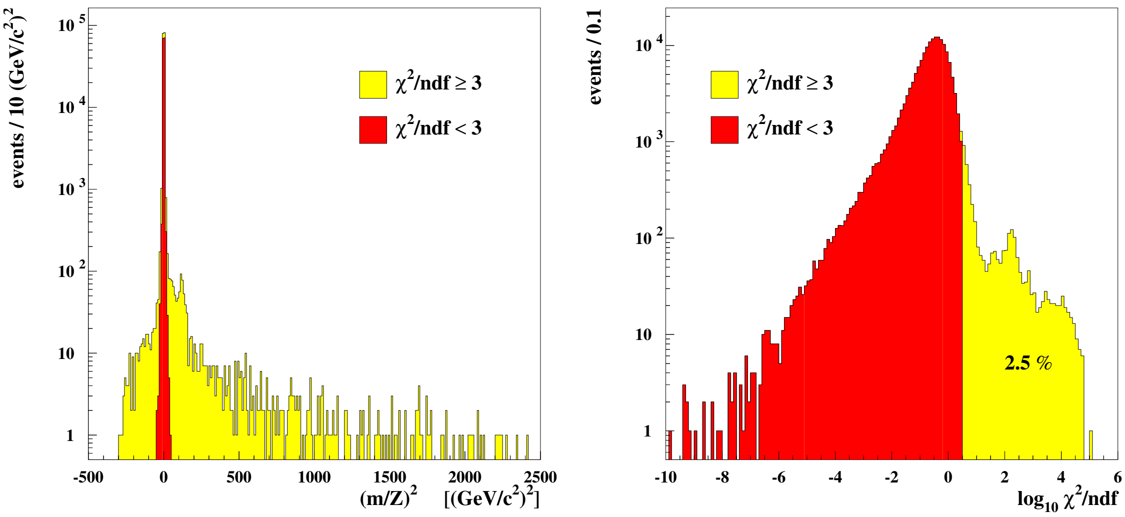

Figure 6.1: $(m/Z)^2$ and corresponding χ^2/ndf distribution at $-100\,\mathrm{GeV}/c$ on the natural particle spectrum, taken with trigger B1·TOF2

One can see rather wide tails up to several thousand $(\mathrm{GeV}/c^2)^2$. Are these reliable mass to charge values?

Fig. 6.1b can answer this question. It shows the corresponding χ^2/ndf distribution with values going up to 10^5. A cut $\chi^2/ndf < 3$, marked with the dark hatch style, removes practically all events with unreasonable high masses. The remaining part in the $(m/Z)^2$ is marked correspondingly.

What is the reason for events with such a poor confidence for the time of flight fit?

Fig. 6.2 shows as an example a time of flight fit result from one event with a $\chi^2 \approx 10^4$.

The found slope includes hits from TOF0, 2, and 5, while TOF1 is missing and TOF4 is omitted by the algorithm, since it would worsen the confidence. The obtained mass to charge value is about $44\,\mathrm{GeV}/c^2$.

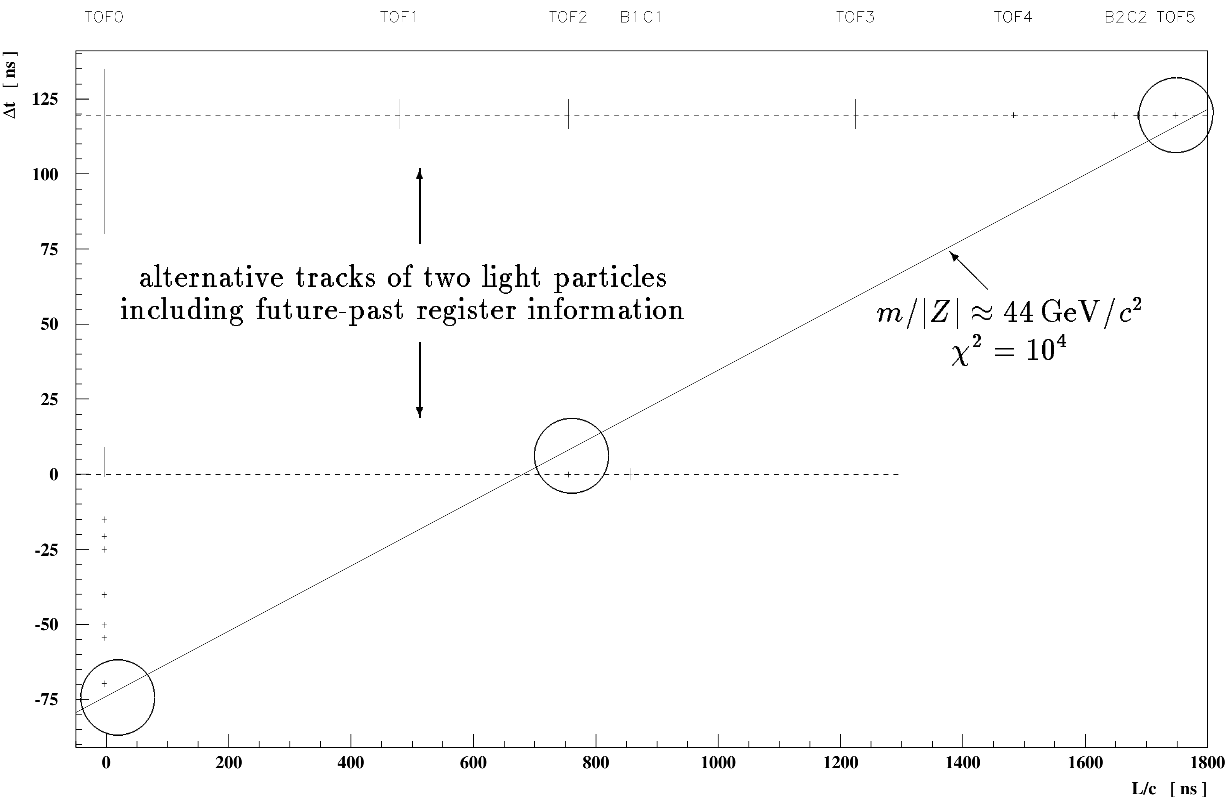

Figure 6.2: A double particle event, identified with a large $\chi^2 = 10^4$ of the fit, which combines information accidentally from both particles

However, inclusion of the hits of the future-past register allows to make an alternative hypothesis for the TOF hits: As shown by the dashed lines one could easily suggest that there were two distinct light particles in the beam line. The first one triggered the coincidence B1·TOF2 and got lost behind B1, while the second one, delayed by 120 ns, gave rise to the downstream trigger B2·TOF4.

More elaborate track finding methods, which would include the information of the future-past registers, could notice also these event topologies. But as long as one is only interested in getting all strangelet candidates, this rudimentary method is adequate enough.

Independent from the time of flight fit reconstruction one can give an estimate about the fraction of events contaminated with double particles in the beam line within 80 ns useful range of the TDCs. In about 2% of the events one finds at least two hits in different slats of a single TOF hodoscope as shown in section 5.2. This value is consistent with the number of events with large χ^2 values.

The cut $\chi^2/ndf < 3$, which keeps more than 97% of the events, determines the reconstruction efficiency.

All the quantitative statements up to now are based on the observation of the natural particle spectrum triggered every 10 ms during the spill time (*cf.* section 2.9). Events from this category build up the reference data sample since the particle composition is unbiased.

6.2.3 Strangelet data sample

Additional triggers are allowed for those events, where the Čerenkov counter Č1 does not give an active veto in the trigger logic, *i. e.* B1·TOF2·$\overline{\check{\mathrm{C}}1}$ is fulfilled looking at the discriminated signals. For ideal spill structures, detectors, discriminators and trigger electronics one would expect to find only antihelium-3 and slower particles in this data sample.

Some characteristics of these events with trigger B1·TOF2·$\overline{\check{\mathrm{C}}1}$ are shown in Fig. 6.3.

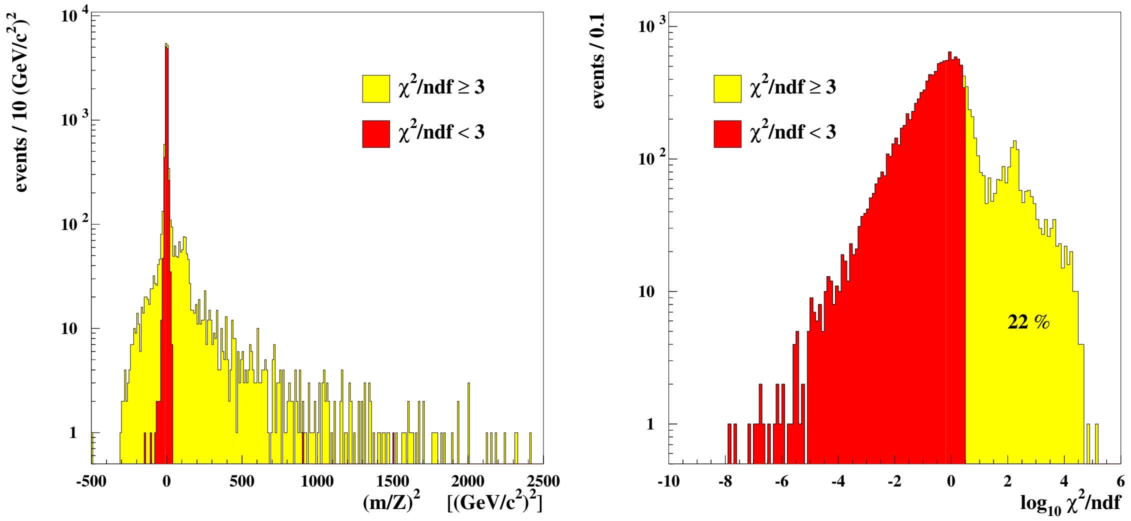

Figure 6.3: $(m/Z)^2$ and corresponding χ^2/ndf distribution at $-100\,\mathrm{GeV}/c$ with trigger B1·TOF2·$\overline{\check{\mathrm{C}}1}$

In comparison to the natural data sample an obvious difference in the *strangelet data sample* is, that the relative fraction of events with an inconsistent time of flight fit is enhanced (22%), most of them pretending high masses.

Independent of this, the fraction of events having two particles in the beam line by looking at the multiplicities in the TOF hodoscopes is also enhanced (14%). On the other hand the fraction of events showing still a TDC stop and/or pulse height in the ADC gate of Čerenkov Č1 is about $3{\cdot}10^{-3}$, which indicate the possibility to have a delayed discriminated signal from the Čerenkov counter, which cannot veto the trigger. Most likely these are two particle events. The second particle, which does not trigger, but still falls into the read-out gates, and contaminates the heavy particle which is below the Čerenkov threshold.

However, the major part of the events taken in the *strangelet data sample* are due to particles which are lost in front of the threshold counter.

6.2.4 Software trigger: inclusion of TOF3

The trigger counters B1·TOF2 are placed in front of the Čerenkov counter Č1. To ensure that the particle passed through the Čerenkov counter, thereafter the event reconstruction has been limited to particles tracks, which reach at least up to TOF3. Under this condition one can use the Čerenkov information to distinguish between fast and slow particles.

By this additional requirement 13% of the recorded events of the natural particle spectrum are rejected, while the events from the *strangelet data sample* are reduced by a factor 500. The lifetime $t_{\rm lab}$ of the particle to be identified is increased from 860 ns (B1) to 1220 ns (TOF3).

6.2.5 $(m/Z)^2$ distributions

The full statistics, including the natural and the *strangelet data sample*, has been reconstructed with the aid of the time of flight fit. Particles have to reach at least TOF3 and consistency in the measurement is required via the cut $\chi^2/ndf < 3$.

The resulting $(m/Z)^2$ distributions are shown in Fig. 6.4.

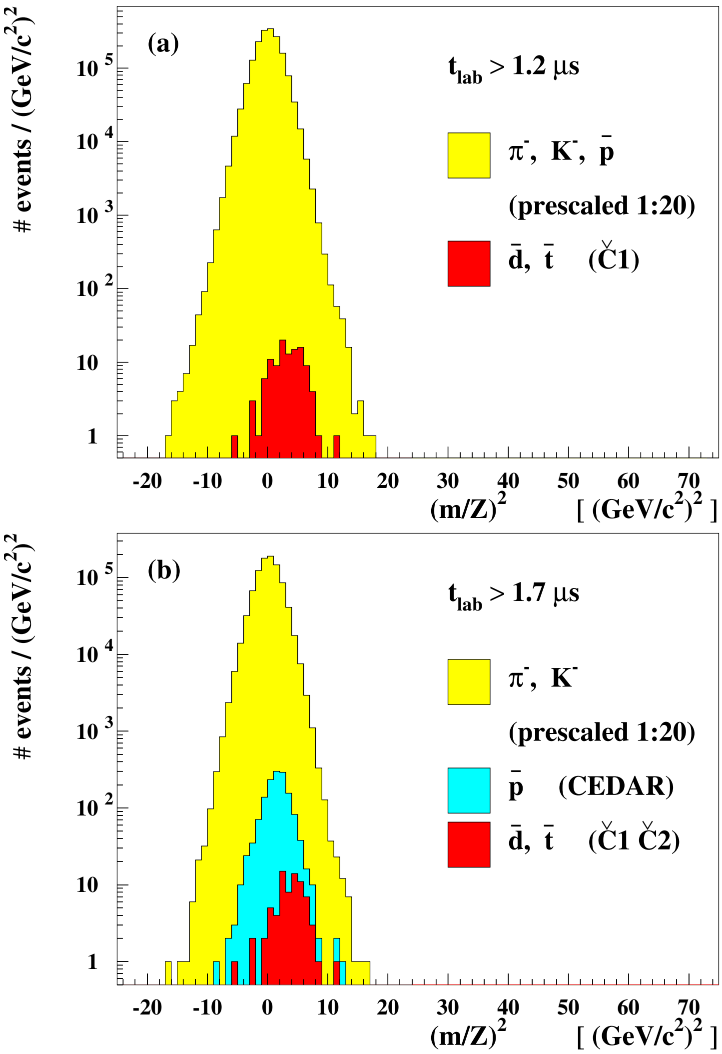

Figure 6.4: $(m/Z)^2$ distributions at $-100\,\mathrm{GeV}/c$; a. events passing at least until TOF3, b. events triggering in addition in the downstream part. Here, the CEDAR tags $\overline{\rm p}$.

In Fig. 6.4a all particles passing at least until TOF3 are shown. The dark hatched distribution shows those events which give no light in Čerenkov counter Č1. Only singly charged

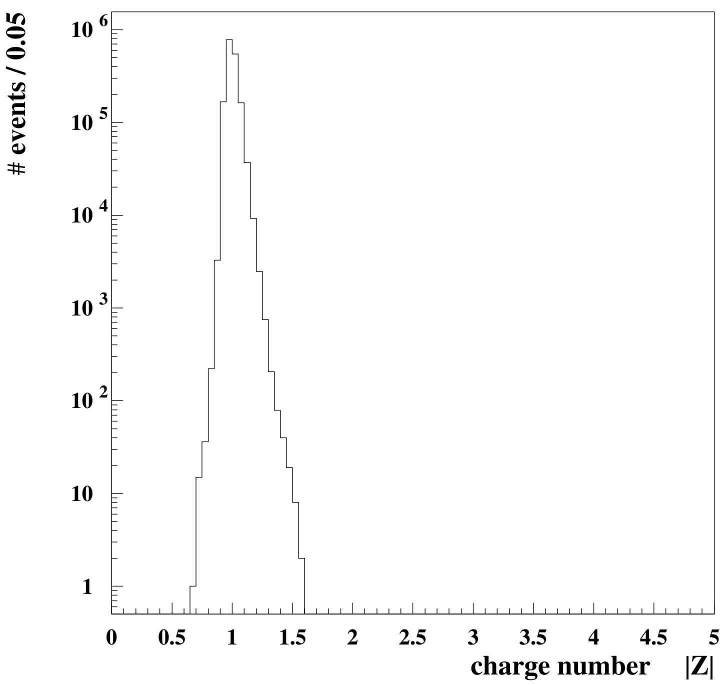

Figure 6.5: Charge distribution $|Z| = \sqrt{\langle \mathrm{d}E/\mathrm{d}x\rangle/\,\mathtt{mip}}$ at $-100\,\mathrm{GeV}/c$. Only singly charged particles have been observed.

particles have been observed, *cf.* Fig. 6.5. The position of the mean value of the m^2 distribution of heavy particle candidates is slightly shifted by $(1.7\,\mathrm{GeV}/c^2)^2$ and indicates the mass of antideuterons. However, some antitritons might be included in this group as well. The light particle group (masses up to antiprotons) peaks near zero and cannot be further distinguished with the help of the time of flight measurement. The recording of particles belonging to this group has been prescaled by a factor 20.

In Fig. 6.4b the subset of events, which trigger in addition in the downstream part of the beam line, are shown. The Čerenkov counter Č2 discriminates between antihelium-3 and antideuterons. Since no doubly charged particle has been observed, Č1 and Č2 together mark antideuterons or heavier particles. In addition the CEDAR is adjusted to tag antiprotons, the third group marked in Fig. 6.4b.

No particle with a mass higher than $4.5\,\mathrm{GeV}/c^2$ has been observed. The largest mass obtained among the events satisfying the Č1-veto is $m = 3.5\,\mathrm{GeV}/c^2$.

6.2.6 Particle yields

The statistics shown is based on $1.7 \cdot 10^{11}$ incident lead ions, corresponding to $1.1 \cdot 10^{11}$ interactions. $2.2 \cdot 10^6$ events have been recorded. The light particle group has been prescaled by a factor 20. 97% of these events could be reconstructed with a consistent time of flight fit. 110 events do not give light in Čerenkov counter Č1 if one looks at the discriminated signal, but 20 of them still give a small pulse height, looking at the ADC register. About one event would be compatible with the inefficiency of that counter, thus, at least 89 events are antideuteron or -triton candidates.

About 70% of the particles also trigger in the downstream part of the beam line. Inclusion of this part adds the information from the second threshold counter Č2 and the CEDAR for additional particle identification. 74 events are showing no light in Č1, nor in Č2, and it is expected that no single event would be compatible with the combined inefficiency of Č1 · Č2.

Antitritons should show up on the m^2 near $7.5(\,\mathrm{GeV}/c^2)^2$, which are most likely covered by the tail of the antideuterons (*cf.* Fig. 6.4). A direct distinction between antideuterons and -triton is impossible. However, it is obvious that the major part consists of antideuterons. The yield of antitritons must be less than 5% of the antideuterons, otherwise one would see a distortion in the m^2 spectrum.

In part of the accumulated statistics ($0.76 \cdot 10^{11}$ interactions) the CEDAR was tuned to tag antiprotons. 1415 events with the 6-fold coincidence were observed at an efficiency of $\eta_{\mathrm{CEDAR}} = 85\%$ by inclusion of the 7- and 8-fold coincidences (*cf.* section 2.7.2).

Considering the trigger (η_{trig}) and reconstruction efficiencies (η_{rec}) and losses due to hadronic interactions (η_{had}) — a short summary is presented in appendix A — the yields of antinuclei can be calculated. In Tab. 6.2 the numbers are summarized.

Table 6.2: Particle yields at $-100\,\mathrm{GeV}/c$

detector	part.	N_{obs}	N_{int} $[10^{11}]$	η_{det}: η_{trig}	η_{rec}	η_{CEDAR}	η_{had}	yield/int. $[10^{-11}]$
up to TOF3	$\overline{\mathrm{d}}$	89	1.09	0.98	0.97		0.70	123 ± 13
up to TOF5	$\overline{\mathrm{d}}$	74	1.09	0.98	0.97		0.56	128 ± 15
ditto	$\overline{\mathrm{p}}$	1415	0.76	0.98	0.97	0.85	0.66	3491 ± 93

Quoted are statistical errors based on an assumed Poisson distribution of the observed number N_{obs}. The two measurements of antideuterons up to TOF3 and TOF5 are not independent, but the observed loss of particles between these two points are compatible with their interaction probability in the beam line. A possible small correction due to antitritons has been neglected. The true antiproton yield might be larger since the geometrical acceptance of the CEDAR in this setting is unknown.

However, it might be worth to quote differential production cross sections for these two particle species. For these the relationship

$$E\frac{\mathrm{d}^3\sigma}{\mathrm{d}p^3} = \frac{E}{p^3} \cdot \frac{1}{\alpha \cdot \eta_{\mathrm{det}}} \cdot \frac{N_{\mathrm{obs}}}{N_{\mathrm{int}}} \cdot \frac{1}{n \cdot l_{\mathrm{target}}} \tag{6.1}$$

is used which includes the integrated acceptance $\alpha = 3.9\,\mu\mathrm{sr}\% = 3.9 \cdot 10^{-8}$ of the beam line derived from the TURTLE simulation and the overall detection efficiency η_{det}. $n \cdot l_{\mathrm{target}}$ are target density and length ($n = 0.033\,\mathrm{barn}^{-1}\,\mathrm{cm}^{-1}$), E/p^3 energy and momentum of the particle. The resulting numbers are shown in Tab. 6.3. Included are statistical and systematic errors.

Three sources for systematic errors are considered: The uncertainty of the (geometrical) acceptance of the detector, an uncertainty of the exact counting of incident lead ions and particle production rates, which do not origin from lead-lead collisions.

The comparison between simulated and measured phase space reconstruction (*cf.* section 3.3.3.3) implies that the actual acceptance α is about $20 - 30\%$ smaller than the

Table 6.3: Invariant production cross sections of $\overline{\mathrm{p}}$ and $\overline{\mathrm{d}}$ at $-100\,\mathrm{GeV}/c$

particle	$E\frac{\mathrm{d}^3\sigma}{\mathrm{d}p^3}\Big\vert_{p_\perp=0}$ $\left[10^{-6}\,\frac{\mathrm{barn}}{\mathrm{GeV}^2}c^3\right]$	y_{lab}
$\overline{\mathrm{p}}$	$680 \pm 20_{(\mathrm{stat.})} \pm 200_{(\mathrm{syst.})}$	5.4
$\overline{\mathrm{d}}$	$24.8 \pm 2.9_{(\mathrm{stat.})} \pm 7.4_{(\mathrm{syst.})}$	4.7

simulated value, thus the cross section might be $20 - 30\%$ larger. On the other hand the counting of the incident lead ions suffers from the limited double pulse resolution of the quartz counter pulses in conjunction with varying spill structures. Based on the simple spill structure model (*cf.* section 5.1) 6 to 17% of the incident lead ions are not registered, thus the true cross section is smaller by this amount. Furthermore, a fraction of observed particles are not produced in lead-lead, but in lead-material interactions, where these materials are air, vacuum windows and detectors near or behind the lead target. A measurement of this *empty target* contribution has been performed at a rigidity of $-10\,\mathrm{GeV}/c$; there the rate of antiprotons without any lead target is about 35% of the observed yield using a 4 mm lead target[1]. Assuming that the particle yields scale identical in the target and *empty target* situation while switching from -10 to $-100\,\mathrm{GeV}/c$ and considering the lead target length differences, the empty target contributions at the high rigidity setting with a 40 mm target should be around

$$35\% \cdot \frac{\exp\left(-40\,\mathrm{mm}/\lambda_{\mathrm{PbPb}}\right)}{\exp\left(-4\,\mathrm{mm}/\lambda_{\mathrm{PbPb}}\right)} = 14\% \qquad (6.2)$$

Thus, the true cross sections $\mathrm{Pb-Pb} \rightarrow \overline{\mathrm{p}}, \overline{\mathrm{d}}$ might be lower by this fraction.

Since none of these contributions has actually been measured for the individual situations the cross section values are embedded within a systematic error of 30%. An acceptance correction for the antiproton measurement with the CEDAR has not been included, since it is difficult to estimate its true value. Considering its antideuteron tagging at $-200\,\mathrm{GeV}/c$ (*cf.* section 6.3.2) and comparing with the threshold counters, it can however be concluded that this acceptance correction is negligibly small.

6.2.7 Releasing the software trigger

Concerning the strangelet search no event has been found with a mass larger than $3.5\,\mathrm{GeV}/c^2$. That limit is based on the upper tails of the m^2 distribution, which has been shown in Fig. 6.4. Those distributions are obtained by restricting the event reconstruction to particles which reach at least TOF3, the time of flight hodoscope located 100 m behind the trigger counter B1.

There were events recorded, where particles do not reach TOF3, but they seem to be lost between B1 and TOF3. Can we find strangelet candidates in that subsample?

One of the best candidates from this group I would like to discuss with the help of the event display, shown in Figs. 6.7 & 6.8, pp. 74-75. In this event only hits up to B1 have

[1]Private communication with Franziskus Stoffel, who is analyzing data taken at low rigidities $\pm 5 \ldots 40\,\mathrm{GeV}/c$ [Stoffel96].

been registered. No signal has been recorded in Čerenkov counter Č1, nor in TOF3. Two lead ions were registered in the ADC gates and TDC range of the quartz counter, while its future-past register gives a wider look into the time (and space) structure of the spill: 51 ions are registered within a visible bunch of 1.6 μs. In TOF1/W1T and TOF2/W2T hits are found from a single secondary particle in the beam line. The two wires in the v-plane of W2T are adjacent. The particle is lost somewhere behind B1. The time of flight fit including the quartz counter and the two TOF hodoscopes yields a mass of 7.4 GeV/c^2 (with $\chi^2 = 10^{-3}$) while the energy loss measurements are compatible with a singly charged particle. No obvious alternative combination of the time information can be found.

The time fit is displaced by about 300 ps to the trigger reference ($\Delta t \equiv 0$ at B1). For a consistent event this line should pass through zero at the position of B1, which is the physical start counter in the trigger. However, the distribution of the offsets of the time of flight fit also has got a finite Gaussian width $\sigma = 130 \pm 5$ ps, as shown in Fig. 6.6, which represents the timing resolution of the start counter B1.

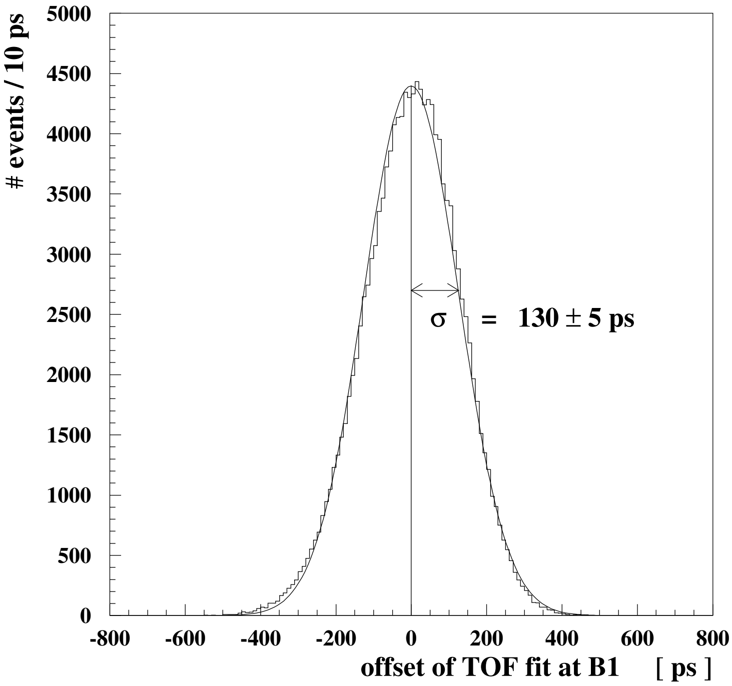

Figure 6.6: Distribution of the offsets of the time of flight fit at start counter B1

There is no hint for any contradiction in the available information from this event, thus one can call it a *strangelet candidate.*

However, a weak point is to decide if one can use the missing Čerenkov signal as an indication for a heavy particle. The exact point where the particle was lost, cannot be determined. But that is crucial to know if one wants to rely on the information of the Čerenkov counter Č1 (besides its natural inefficiency). In this example it might be, that the particle was already lost in front of the Čerenkov counter (at 268 m). B1 (at 257 m) gives the last signal, no hit is visible in W3S (at 354 m) or in any counter placed behind.

A detailed quantitative description of event yields which show a strangelet signature in the detector, although only known light particles are passing through the beam line (*i. e.* simulation of the natural *background* for the strangelet search), is still owing.

But if the shown example is a background event, two explanations can be investigated:

- The trigger had a common jitter of 300 ps $\approx 2.3\sigma$, and the time measurements of TOF0 and TOF1 are displaced.

  In a Gaussian distribution one expects to see offsets of at least 2.3σ (*cf.* jitter of B1) in one out of 100 events and offsets of at least 7σ (*cf.* TOF1) in one out of 10^{12} cases. But it is questionable if the time measurements are obeying Gaussian distributions over twelve orders of magnitude.

or

- There is a hidden second particle in the beam line around 0.7 ns displaced from the first one, although no pulse height information gives really support this hypothesis. The 10 ns resolution of the future-past registers is not sufficient to provide answers in this case. Thus, the second particle is subject to the combined inefficiency of the TOF hodoscopes and wire chambers.

  Assuming that all individual detector inefficiencies are on a percent level (*cf.* section 5.3 for the TOF planes) the combined inefficiency of two TOF counters (TOF1, TOF2) and two wire chambers (W1T, W2T) should not be larger than 10^{-8}.

Therefore, one expects to see such a *background* event in one out of 10^8 to 10^{12} cases. Remarkable is that it has been already observed in the recorded data sample of $2 \cdot 10^6$ events.

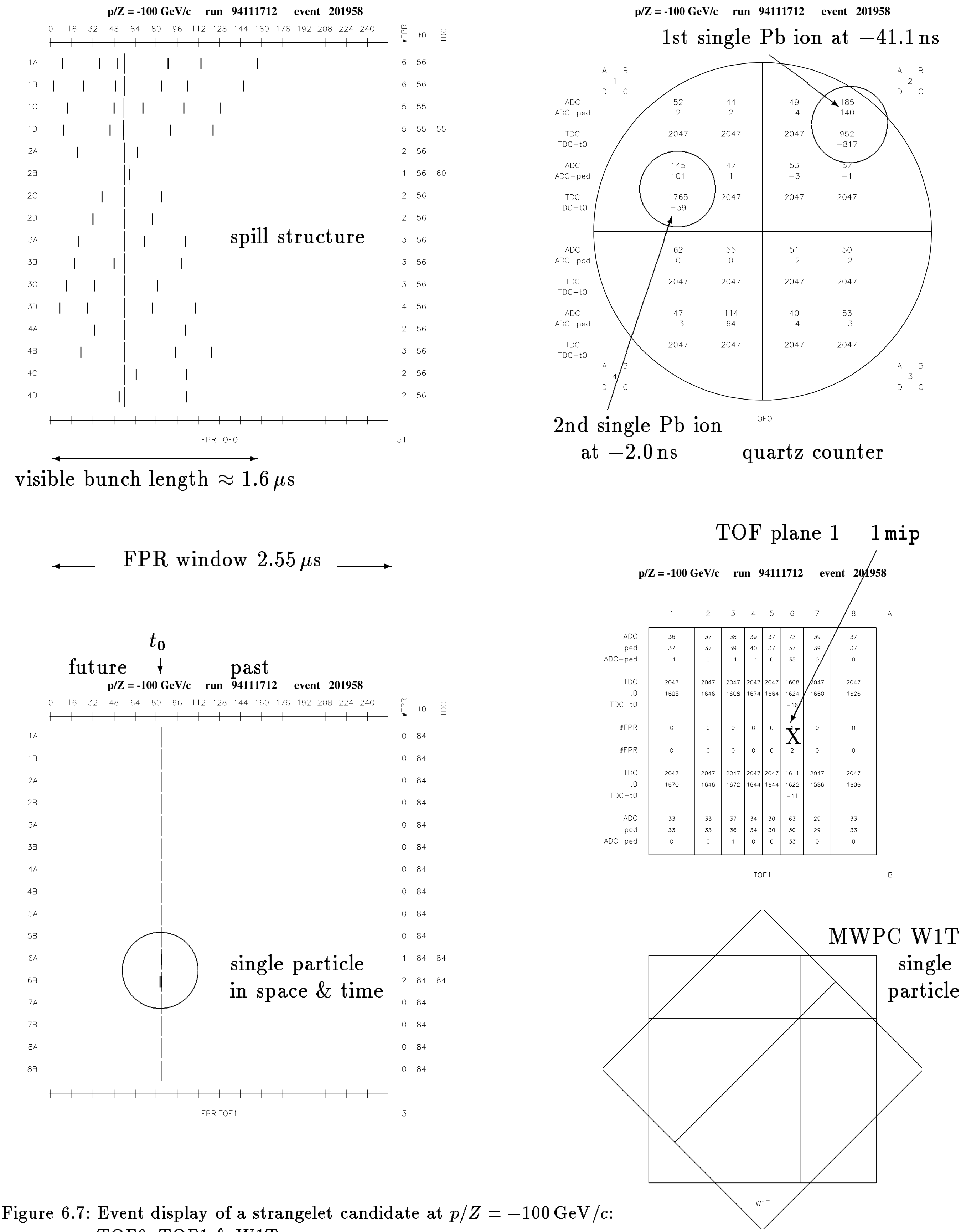

Figure 6.7: Event display of a strangelet candidate at $p/Z = -100\,\mathrm{GeV}/c$: TOF0, TOF1 & W1T

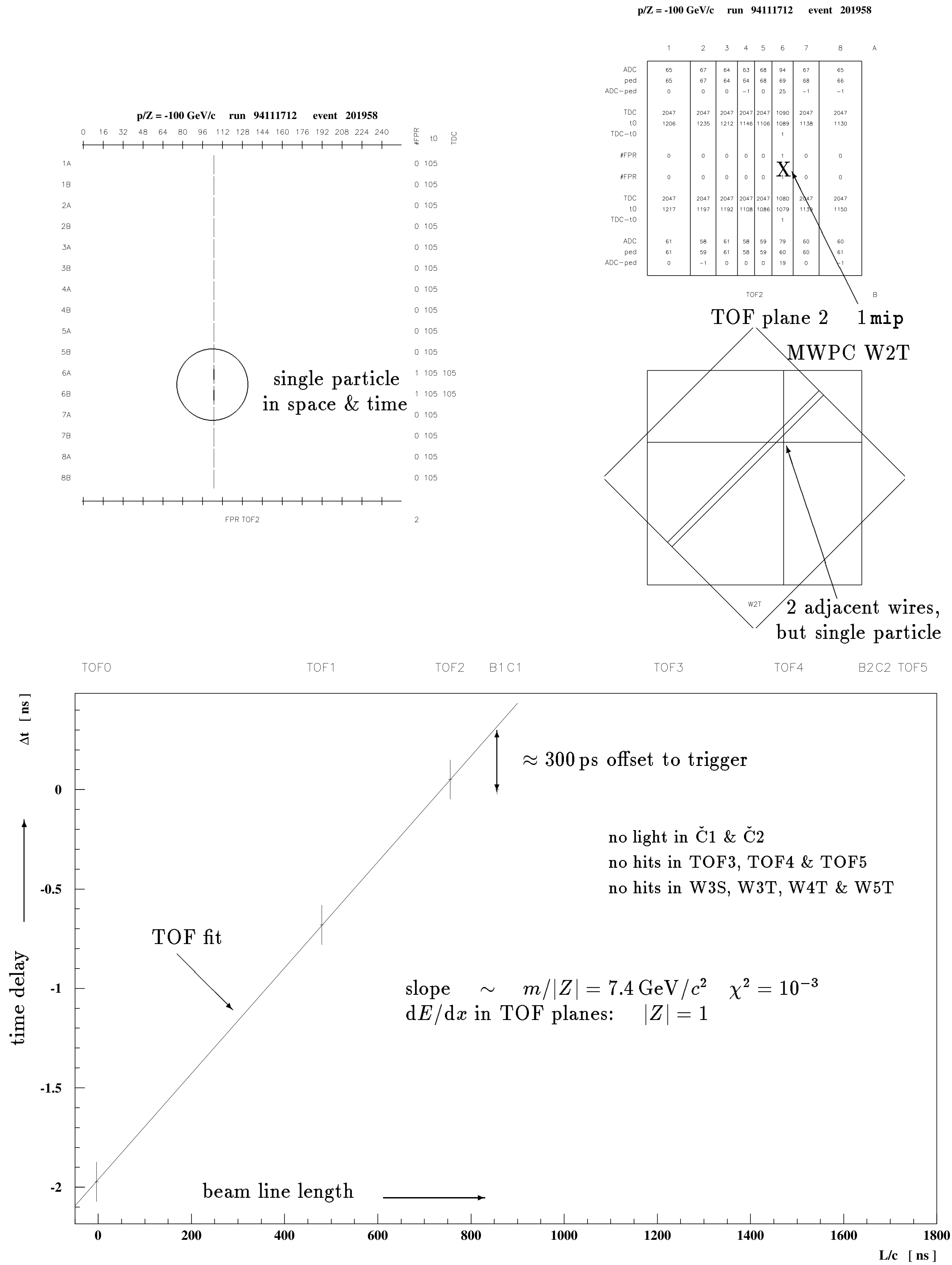

Figure 6.8: Event display of a strangelet candidate at $p/Z = -100\,\mathrm{GeV}/c$: TOF2, W2T & TOF fit

6.3 Rigidity setting $p/Z = -200\,\mathrm{GeV}/c$

Different trigger conditions were chosen for the rigidity setting of $-200\,\mathrm{GeV}/c$ (*cf.* Tab. 6.1). The low particle rates (*cf.* section 5) allowed to record the full particle spectrum without prescaling. Here, the data taken with the trigger B1·TOF2 is discussed.

6.3.1 Antiproton tagging

Data from $0.21 \cdot 10^{11}$ Pb−Pb interactions have been recorded (without any prescaling). The low pressure of 34 mbar in Č1 is intended to separate between antiprotons (and -deuterons) from lighter particles.

Fig. 6.9 shows the corresponding $(m/Z)^2$ and charge distributions for 198'000 particles which travel at least up to TOF3.

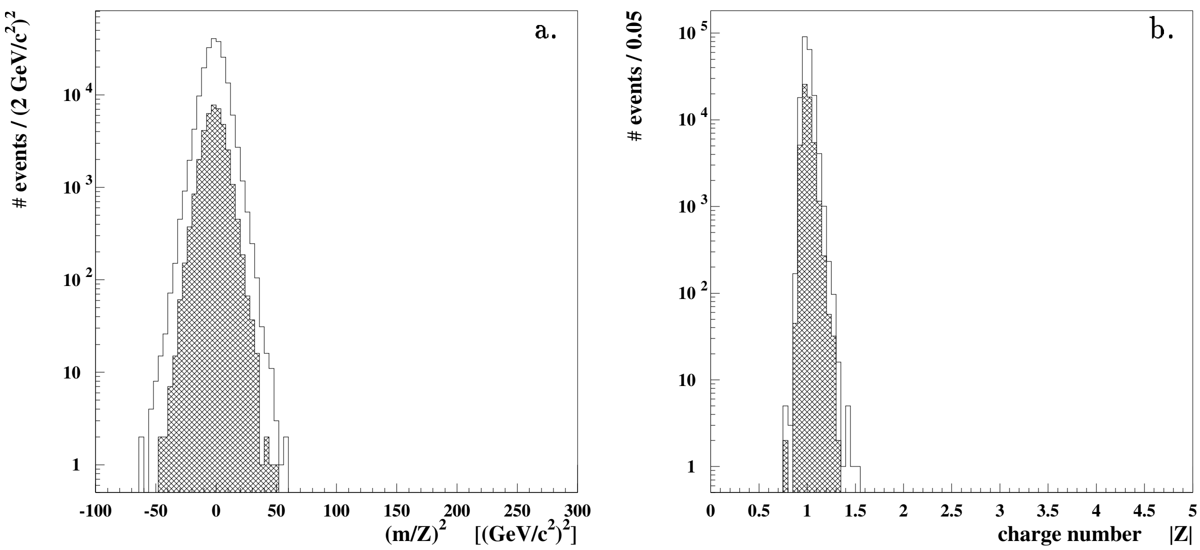

Figure 6.9: Events taken at $p/Z = -200\,\mathrm{GeV}/c$ for antiproton tagging purposes. Hatched or those particles which do not show a signal in Č1.

Only singly charged particles have been found. The upper tail of the mass-squared distribution covers masses up to $8\,\mathrm{GeV}/c^2$.

38′000 events have been observed without a signal from Č1, thus being antiproton candidates. However, a numerical determination of the antiproton (and -deuteron) yield in this data sample suffers from the inefficiency of the Čerenkov counter Č1. This was determined to be 20% (*cf.* section 2.7.1) at the low pressure of 34 mbar. Thus, all observed antiproton candidates are compatible with the inefficiency of the threshold counter and one cannot claim a number of observed antiprotons.

6.3.2 Antideuteron tagging

A larger amount of statistics has been accumulated at a pressure of 130 mbar in Č1 and Č2 which separates antideuterons from lighter particles. In $1.28 \cdot 10^{11}$ incident lead ions $1.32 \cdot 10^6$ events have been recorded without any prescaling. Out of these $1.05 \cdot 10^6$ events

(80%) reach at least TOF3 and most of them ($\eta_{\text{rec}} = 97\%$) yield a consistent time of flight measurement with $\chi^2/ndf < 3$. 95% of those particles reach the end of the beam line until TOF5. From the inefficiency of Č1 ($\epsilon_{\check{C}1} = 2 \cdot 10^{-4}$) one can expect to get about 300 events without detected light in a single Čerenkov counter. 285 in Č1 and 299 events in Č2 show this signature. But six events show in coincidence no light in Č1 · Č2. And one would not expect a simultaneous inefficiency in Č1 and Č2 in this statistics, when assuming full independence of the two threshold counters ($10^6 \cdot (2 \cdot 10^{-4})^2 = 4\%$).

Fig. 6.10 summarize the corresponding distributions.

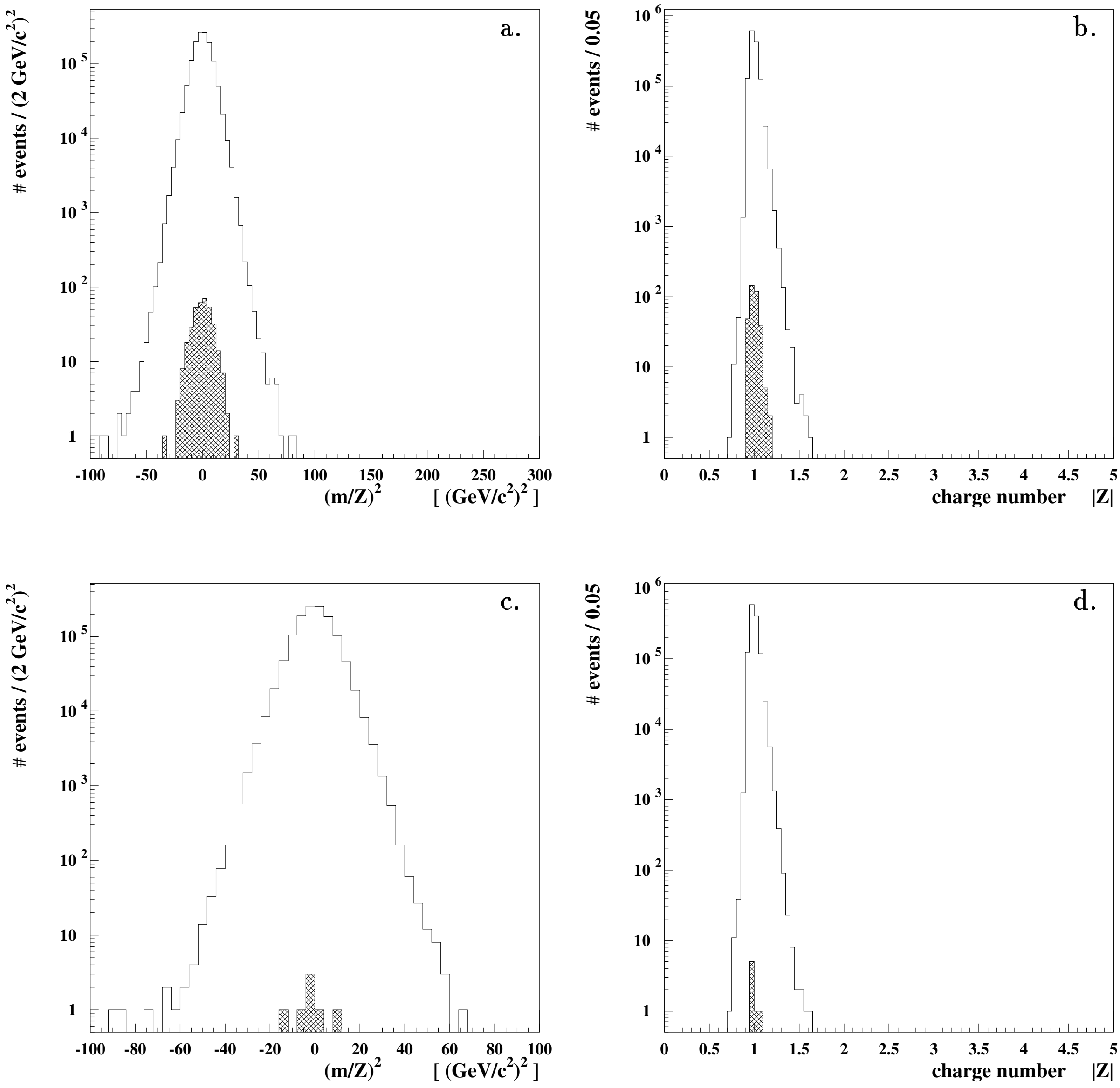

Figure 6.10: Events taken at $p/Z = -200\,\mathrm{GeV}/c$ for antideuteron tagging purposes.
a. $(m/Z)^2$ distribution of events which reach at least TOF3.
Hatched are 356 events with a missing signal of Čerenkov Č1
b. the corresponding charge distribution
c. $(m/Z)^2$ distribution of those particles which reach TOF5.
Hatched are 7 antideuteron candidates based on Č1 · Č2
d. corresponding charge distribution

In addition all six events lead to a 6-fold coincidence in the CEDAR, which was tuned to tag antideuterons in this data sample. From some additional $0.33 \cdot 10^{11}$ incident lead ions the CEDAR information was not available, but another single antideuteron out of $0.36 \cdot 10^{6}$ events could be identified based on the combined threshold counter information. Any doubly charged particle (*e. g.* antihelium-3 or -4) can be excluded, if one looks at the charge number distributions (*cf.* Fig. 6.10b, d).

The summarized antideuteron yield at $-200\,\mathrm{GeV}/c$ can be found in Tab. 6.4.

Table 6.4: Antideuteron yield at $-200\,\mathrm{GeV}/c$

N_{obs}	N_{int} $[10^{11}]$	η_{det} η_{trig}	η_{rec}	η_{had}	yield/int. $[10^{-11}]$
7	1.01	0.98	0.97	0.56	13.0 ± 4.9

$E\frac{\mathrm{d}^3\sigma}{\mathrm{d}p^3}\Big\vert_{p_\perp=0}$ $\left[10^{-6}\,\frac{\mathrm{barn}}{\mathrm{GeV}^2}c^3\right]$	y_{lab}
$0.62 \pm 0.23_{(\mathrm{stat.})} \pm 0.18_{(\mathrm{syst.})}$	5.4

6.3.3 Strangelet limit

Concerning the heavy particle search both Čerenkov counter settings can be added.

In $1.2 \cdot 10^{11}$ Pb−Pb interactions no singly charged event with a consistent mass above $8\,\mathrm{GeV}/c^2$ has been found.

6.4 Conclusions

In the two rigidity settings (-100 and $-200\,\mathrm{GeV}/c$) antiproton and antideuteron production rates at forward rapidities could be evaluated. No doubly charged particle has been found.

The restriction to events which reach at least TOF3 has not revealed any strangelet candidate corresponding to a lifetime limit $t_{\mathrm{lab}} \geq 1.22\,\mu\mathrm{s}$.

At least a *strangelet candidate* with a mass of $7.4\,\mathrm{GeV}/c^2$ was found after releasing the inclusion of TOF3 ($t_{\mathrm{lab}} \geq 0.86\,\mu\mathrm{s}$). But in order to establish such a candidate further investigations of the expected *background* are necessary.

Chapter 7

Discussion of the data taken at the positive magnetic rigidities $p/Z = +100$ and $+200\,\mathrm{GeV}/c$

7.1 Overview of the analyzed settings

The data taken at positive rigidities are characterized by much higher secondary beam fluxes than at negative rigidities. In a comparison of $+100$ *vs.* $-100\,\mathrm{GeV}/c$ the typical flux is ten times higher per interaction while $+200$ *vs.* $-200\,\mathrm{GeV}/c$ show an increase by more than 10^3 per interaction.

Most of the observed positive particles are not created as new particles in the interaction but are fragments, namely protons, deuterons and alphas, of the colliding nuclei. At $100\,\mathrm{GeV}/c$ protons and deuterons have rapidities of 5.4 and 4.7, respectively, while at $200\,\mathrm{GeV}/c$ these values are 6.1 and 5.4 and thus close to the beam rapidity of 5.8.

Due to the high secondary rates, data taking at the positive rigidities could only be done with the prescale mechanism of the trigger logic. Data from both settings ($+100$ and $+200\,\mathrm{GeV}/c$) have been accumulated with threshold Čerenkov counter settings suppressing the recording of particles with a mass to charge ratio smaller than that of ^{8}He. That means, that not only mesons (π^+ and K^+), but also the fragments p, d, ^{4}He and t were rejected. Only a small fraction of them have been registered for calibration purposes.

The data at $+100\,\mathrm{GeV}/c$ has been recorded with the trigger condition $\mathrm{B1}\cdot\mathrm{TOF2}\cdot\overline{\check{\mathrm{C}}1}$ using a 40 mm lead target, while the registered data at $+200\,\mathrm{GeV}/c$ includes the up- and downstream part ($\mathrm{B1}\cdot\mathrm{TOF2}\cdot\overline{\check{\mathrm{C}}1}\cdot\mathrm{B2}\cdot\mathrm{TOF4}\cdot\overline{\check{\mathrm{C}}2}$) obligatorily. Here, a thinner lead target of 16 mm has been used. Tab. 7.1 summarizes numbers of the accumulated statistics for the two settings.

7.2 Rigidity setting $p/Z = +100\,\mathrm{GeV}/c$

For $3.3\cdot 10^{11}$ incident lead ions about $1.5\cdot 10^9$ coincidences in B1·TOF2 have been counted. Only the fraction 1/500 of these triggerable events have been recorded by using the prescale mechanism of the trigger logic including Čerenkov counter Č1. Among these

Table 7.1: Overview of the settings at positive rigidity

p/Z	trigger	Čerenkov Č1 [mbar]	Čerenkov Č2 [mbar]	CEDAR tags	$N_{\mathrm{Pb\,ion}}$ [10^{11}]	N_{event} [10^{6}]
$+100\,\mathrm{GeV}/c$	$\mathrm{B1{\cdot}TOF2{\cdot}\overline{\check{C}1}}$	— < ^{8}He — 2059	1999	d	3.27	6.7
$+200\,\mathrm{GeV}/c$	$\mathrm{B1{\cdot}TOF2{\cdot}\overline{\check{C}1}}$ $\mathrm{{\cdot}B2{\cdot}TOF4{\cdot}\overline{\check{C}2}}$	— < ^{8}He — 500	500	d	3.26	4.2

$3 \cdot 10^6$ recorded events $5 \cdot 10^5$ events have been taken with an active veto in Č1 on the trigger level (*i. e.* the *strangelet data sample*).

In view of the heavy particle search the goal is now to identify the particles which have been recorded in this latter event class. In a first step the time of flight fit reconstruction has been applied. Interesting are those events remaining with a rather large slope ($\propto (m/Z)^2$).

This step yields events which pretend a high mass to charge ratio. One example of such a case is shown in an event display in Figs. 7.1 & 7.2, pp. 81-82. Only the upstream part of the beam line detectors were read out and hits until TOF3/W3T have been recorded. The realized time of flight fit, which considers the TDCs of the TOF counters, suggests a particle with a mass of $44.7\,\mathrm{GeV}/c^2$. But as can be seen from the event display it combines the TDC values of two different particles in the beam line and an even earlier lead ion in TOF0. This combination of hits yields an acceptable small χ^2 value of 2.3. The TDC value of TOF1 is missing. Moreover, in this time of flight fit the line does not pass near by zero, which is per definition the nominal trigger time of B1, but is 10 ns later.

Alternative combinations of the hits are shown with the hashed lines, including the future-past register hits in the TOF hodoscopes 0, 1 and 2. The quartz counter measured six lead ions within the dynamic range of its ADCs and TDCs, while the FPR sees 82 ions within $2\,\mu$s. Most likely the lead ion near $\Delta t = 0$ produced a fast particle, which was missed in TOF1 but triggered B1·TOF2. Somewhere between W2S and W3S this first particle was lost. 50 ns later a further lead ion was registered in the future-past register of the quartz counter. It produced a fast secondary particle seen in the FPR of TOF1 and TOF2 and in the TDC of TOF3. Double hits are clearly identified in the TOF hodoscope 2 as well as in the wire chambers W2T and W2S. Moreover, a TDC stop in the Čerenkov counter Č1 is visible, where its timing fits the second particle.

The contradiction, that this event has been recorded under the trigger condition $\mathrm{B1{\cdot}TOF2{\cdot}\overline{\check{C}1}}$, *i. e.* including an active Čerenkov veto, but still a TDC stop in Č1 is visible, needs some explanation.

The first of the two particles triggers in the coincidence of B1·TOF2 before it is lost most likely in front of Č1, so that its veto capability on the trigger level cannot be used. The

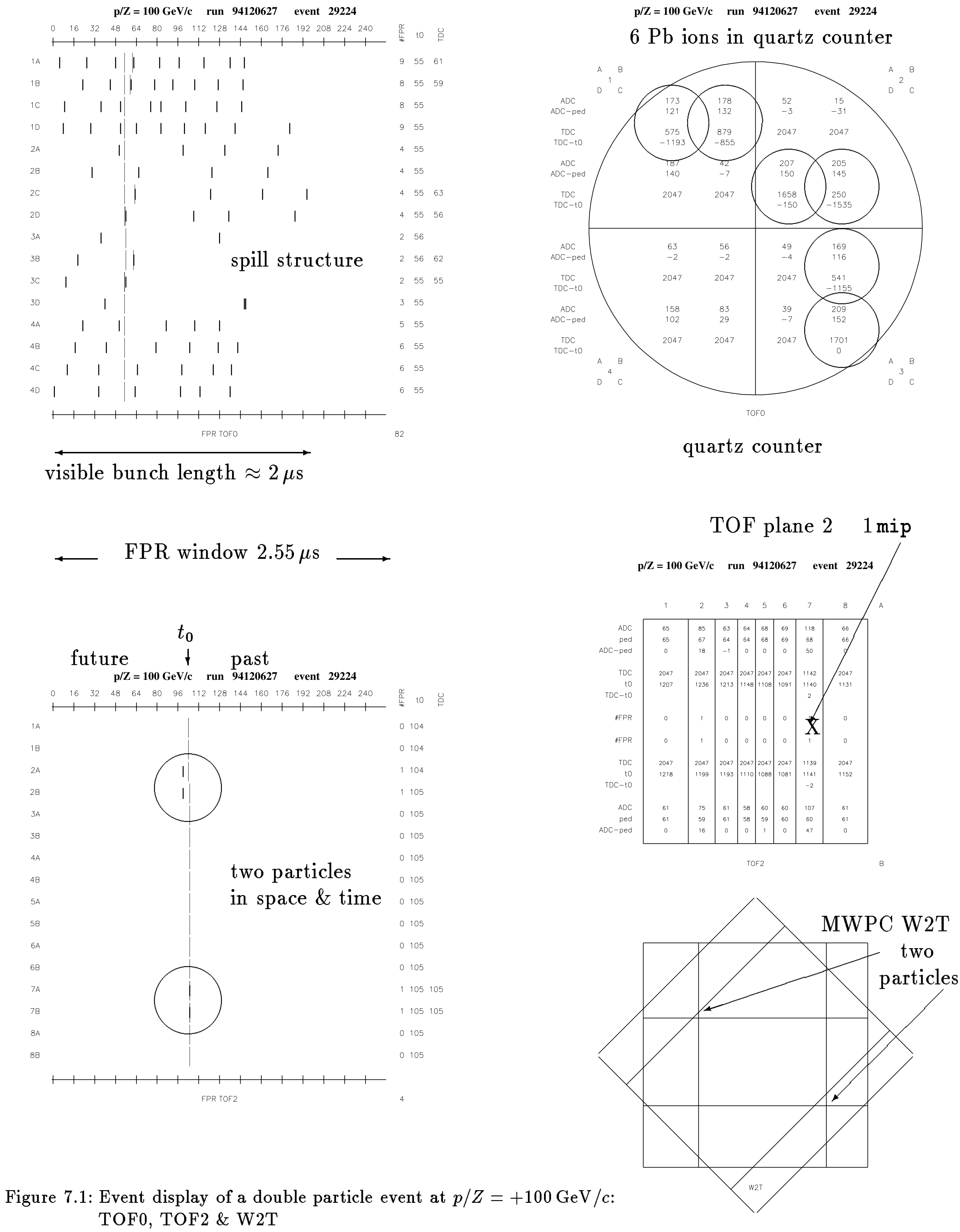

Figure 7.1: Event display of a double particle event at $p/Z = +100\,\mathrm{GeV}/c$: TOF0, TOF2 & W2T

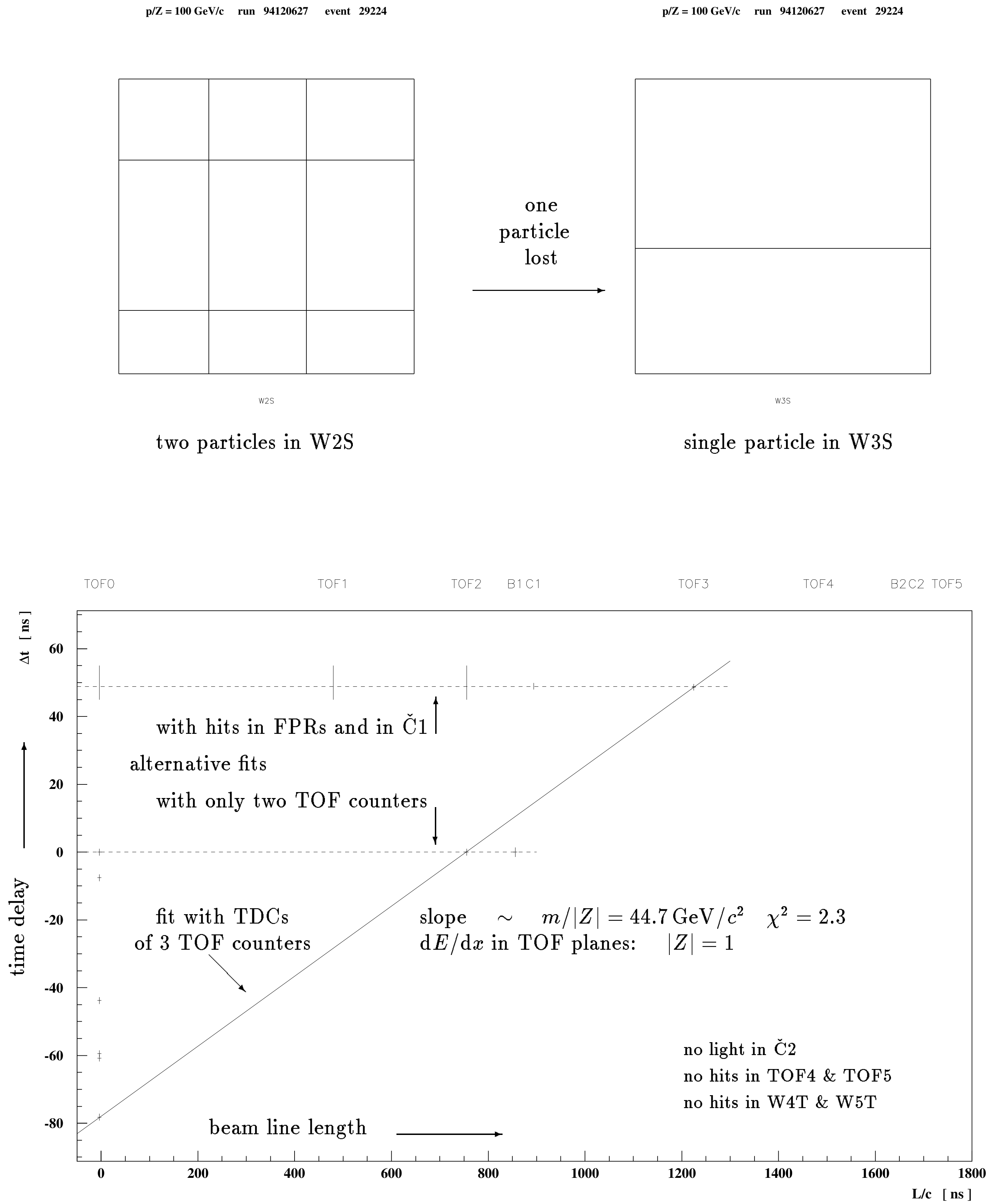

Figure 7.2: Event display of a double particle event at $p/Z = +100\,\mathrm{GeV}/c$: W2S, W3S & time fit

second particle, which comes 50 ns later, falls still into the gates of the ADCs and TDCs of the detector components, including the Čerenkov counter. But its signal is too late for an active veto on the trigger level.

In two steps the reconstruction method can be improved easily to deal with event topologies of this type, where hits from different particles are combined accidentally pretending a slow particle. The first step concerns the time of flight fit itself. In a second step there will be a closer look to the Čerenkov counter.

In the shown example the measurement suffers from the inefficiency of TOF1. A mandatory inclusion of this counter in the reconstruction already improves the rejection of combinations of hits belonging to different particles. The result including this first step is shown in Fig. 7.3.

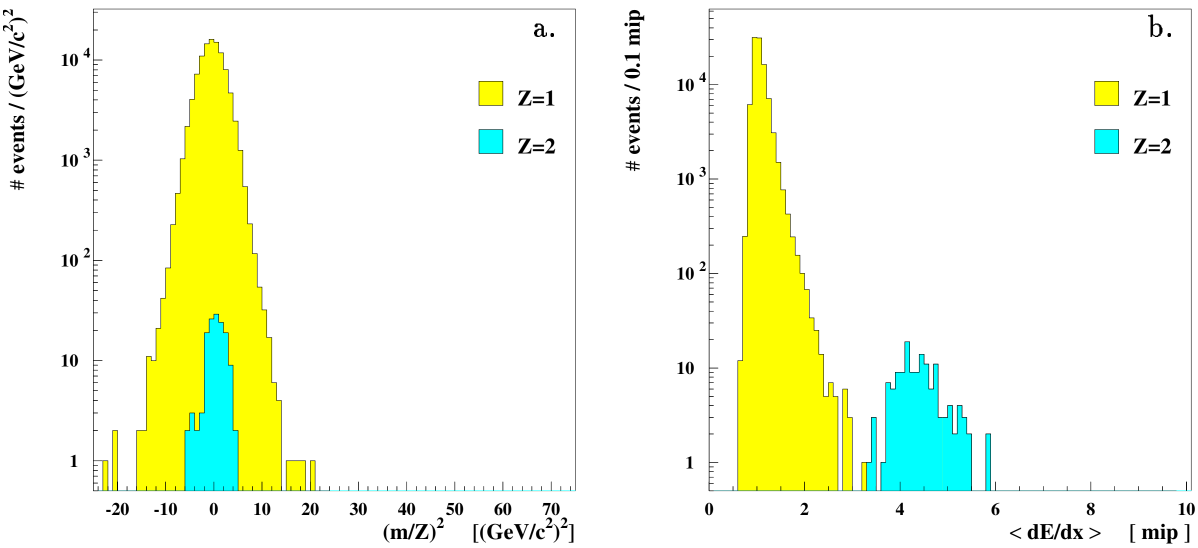

Figure 7.3: $(m/Z)^2$ (a) and $\langle \mathrm{d}E/\mathrm{d}x \rangle$ (b) distributions at $+100\,\mathrm{GeV}/c$ under the trigger condition $\mathrm{B1}\cdot\mathrm{TOF2}\cdot\overline{\check{\mathrm{C}}1}$.

Fig. 7.3(a) shows the $(m/Z)^2$ distribution as a result of consistent time of flight fits ($\chi^2/ndf < 3$) including TOF1, TOF2 and TOF3 and (b) the corresponding energy loss measurement in the TOF hodoscope, reflecting the charge of the traversing particles.

Both, singly and doubly charged particles, which are marked correspondingly in both plots, can be found. In the group of the singly charged particles a few entries in the mass range 4 to $4.5\,\mathrm{GeV}/c^2$ can be found, but stringently these are not heavy particles, because a similar group is also visible on the left side of the distribution pretending particles with a negative mass square. These are neither *tachyons*[1] nor strangelets, but just light particles (*e. g.* protons) which show up in the tails of the mass distribution due the limited resolution of the time of flight measurements.

This resolution defines the lower mass limit of the detector to identify a heavy particle among the abundant light particle species.

The situation is similar in the group of the doubly charged particles. They have got a relative yield 1/800 of the singly charged species. Their observed distribution covers masses up to $4\,\mathrm{GeV}/c^2$. Helium-8, which should show up near $16(\,\mathrm{GeV}/c^2)^2$, or heavier

[1] A hypothetical particle which moves faster than light.

isotopes of the alpha particle can be excluded in this group. Most likely all these events are fast helium-3 or -4 isotopes which are subject to the inefficiency of the Čerenkov counter.

The reconstruction efficiency is about 97% and determined by the inefficiency of TOF1 and the required consistency of the time of flight fit ($\chi^2/ndf < 3$).

As a provisional result, one can already conclude that no heavy particle candidate above $5\,\mathrm{GeV}/c^2$ in the group of singly and doubly charged particles has been found. No event with a charge $Z > 2$ could be identified.

As already discussed above all these events have been recorded with an active Čerenkov veto on the trigger level. Nevertheless, it is not excluded, that still a signal from the Čerenkov counter can be found. This stringent fact is visualized quantitatively in Fig. 7.4(a). It shows the pulse height information obtained from Čerenkov counter Č1.

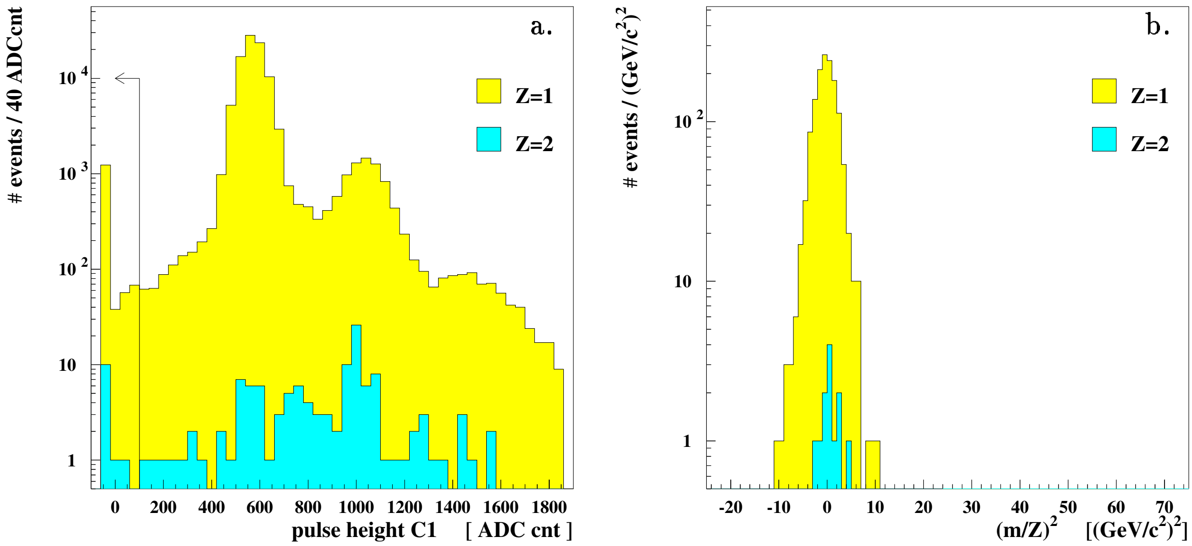

Figure 7.4: Pulse heights in Č1 (a) and remaining $(m/Z)^2$ distribution (b) after the Čerenkov cut pulse heigt Č1 < 100 ADC counts.

Besides a rather small fraction of events showing no light in Č1, *i. e.* where the pulse height is near zero ADC counts, most of the events show a remarkable energy deposition in the Čerenkov counter. The major group can be found near 600 counts, being compatible with a single fast particle. A second group around 1100 counts is compatible with double particle events. A smaller shoulder around 1500 counts can be interpreted as events with multiplicity three. The doubly charged particles are marked correspondingly and their main fraction can be found around 1000 counts. Remarkable is the obvious nonlinearity of the multiplicity *vs.* ADC counts showing some saturation at high pulses and the fact that doubly charged particles show a similar energy deposition like two singly charge particles.

Concerning the strangelet search it is allowed to reject all those events which still show a significant signal in the Čerenkov counter.

The requirement pulse height Č1 < 100 ADC counts as indicated by the vertical line in Fig. 7.4(a) reduces the remaining events by a factor 100. The corresponding $(m/Z)^2$ distribution is shown in Fig. 7.4(b). For singly charged particles the width at the bottom of this distribution covers masses up to $3.5\,\mathrm{GeV}/c^2$, for doubly charged particles the distribution looks narrower, but it has got a similar width in units of mass, if one considers the charge.

Strangelets would have to show up outside of these distributions. Thus, the remaining events shown are light particles which are subject to the inefficiency of the Čerenkov counter Č1. A rough estimate of this inefficiency is

$$\epsilon_{\check{\mathrm{C}}1\,\mathrm{at\,2\,bar}} \approx \frac{\text{remaining events}}{\text{triggerable events}} \approx \frac{1.5 \cdot 10^3}{1.5 \cdot 10^9} = 10^{-6} \tag{7.1}$$

7.3 Rigidity setting $p/Z = +200\,\mathrm{GeV}/c$

A similar treatment can be done with the data taken at $+200\,\mathrm{GeV}/c$. Here, the mandatory inclusion of the up- and downstream trigger for the recording of events provides more measurement tools. From $3.3 \cdot 10^{11}$ incident lead ions $4.1 \cdot 10^9$ and $3.3 \cdot 10^9$ coincidences have been counted in B1·TOF2 and B2·TOF4, respectively. The observed relative flux drop of 20% is larger than the simulated acceptance loss of 2% between TOF3 and TOF5, but this discrepancy becomes smaller if one includes estimations about the absorption of particles due to their hadronic collisions in the beam line material. For protons this additional loss is about 8% and for deuterons about 15%.

A fraction 1/800 of the triggers in (B1·TOF2) · (B2·TOF4) have been written to tape ($4.1 \cdot 10^6$). $5.5 \cdot 10^4$ events have been recorded with an active Čerenkov veto in both counters, Č1 and Č2, thus being the *strangelet data sample*.

Again, this latter group has been investigated using the reconstruction tools. The $(m/Z)^2$ distributions obtained from the time of flight fit, their energy loss obtained from the $\mathrm{d}E/\mathrm{d}x$ measurements in the scintillation counters and the two pulse height distributions in Č1 and Č2 are shown in Fig. 7.5.

Entries are marked accordingly to their charge as obtained from the $\mathrm{d}E/\mathrm{d}x$ measurements. Out of the 6000 identified particles about 10% are doubly charged and one entry is compatible with a $Z = 3$ particle, thus being a lithium isotope. The largest tails of singly charged particles cover masses of up to $7\,\mathrm{GeV}/c$.

Again, concerning the strangelet search, one can reduce this mass limit by the inclusion of the pulse height information in Č1 and Č2.

The Čerenkov light distributions in Č1 and Č2 are displayed in Fig. 7.5(c) and (d), respectively. Qualitatively these distributions have got the same structure as discussed in section 7.2. But the peaks corresponding to single and double multiplicity events have lower positions in units of ADC counts, since the operating pressure is four times smaller compared to the setting at $+100\,\mathrm{GeV}/c$. The restriction to events showing no light neither in Č1 nor in Č2 (pulse height < 50 ADC counts) reduces the number of events by a factor 10. The remaining events are displayed in Fig. 7.6.

The single event with $Z = 3$ disappeared. The mass threshold (*cf.* Fig. 7.6(a)) is reduced to $5.5\,\mathrm{GeV}/c^2$ for singly charged particles while it is about $9\,\mathrm{GeV}/c^2$ for doubly charged particles. The chosen pressure in the Čerenkov counters set mass thresholds at 3.6 and $7.2\,\mathrm{GeV}/c^2$, respectively.

So a few entries in the mass window between 3.6 and $5.5\,\mathrm{GeV}/c^2$ with charge one and between 7.2 and $9\,\mathrm{GeV}/c^2$ with charge two remain without any contradiction in the time of flight and Čerenkov measurement. Thus, a rare observation of particles in these mass ranges cannot be excluded. But looking at the shape of the reconstructed $(m/Z)^2$ distribution it is very likely that these are fast particles being subject to the Čerenkov counter

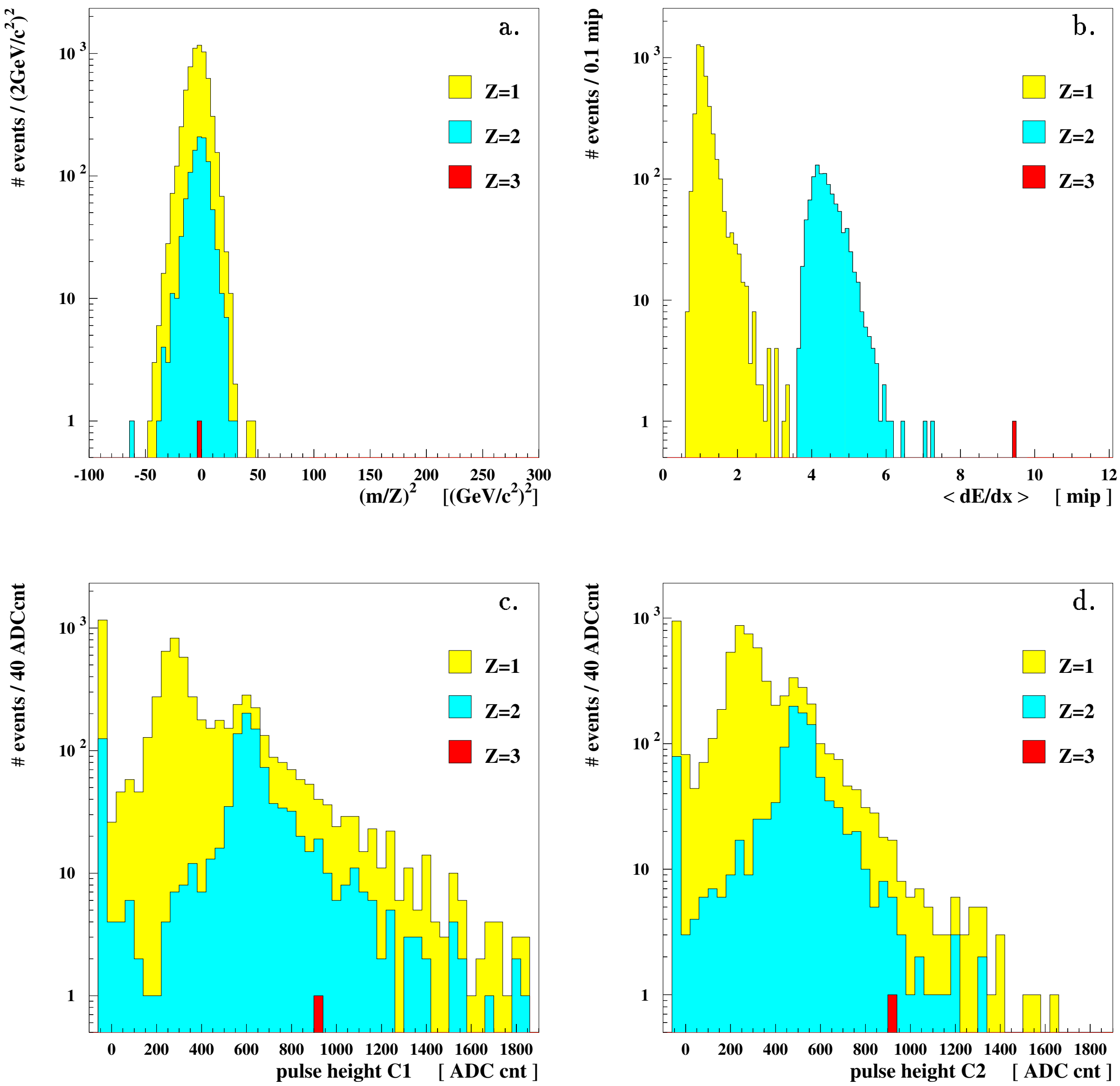

Figure 7.5: Distributions at +200 GeV/c without Čerenkov cut.
(a) The $(m/Z)^2$ distribution.
(b) The $\langle dE/dx \rangle$ distribution yielding singly and doubly charged events and one lithium isotope.
(c) and (d) The pulse height distributions in Č1 and Č2, although an active Čerenkov veto on the trigger level is requested.

efficiency and being in the tail due to the finite resolution of the time of flight measurement.

Thus, all the remaining events have to be interpreted as light particles which are subject to the combined inefficiency of both Čerenkov counters.

A further characteristic of these events is shown in the remaining three plots of Fig. 7.6(b-d). The energy loss measurement in the scintillator counters is compared to the energy measurement with the hadron calorimeter. The bulk of singly charged particles show the nominal energy deposition of 200 GeV in the calorimeter, which corresponds to their momentum of 200 GeV/c. The doubly charged particles have got a momentum, which is

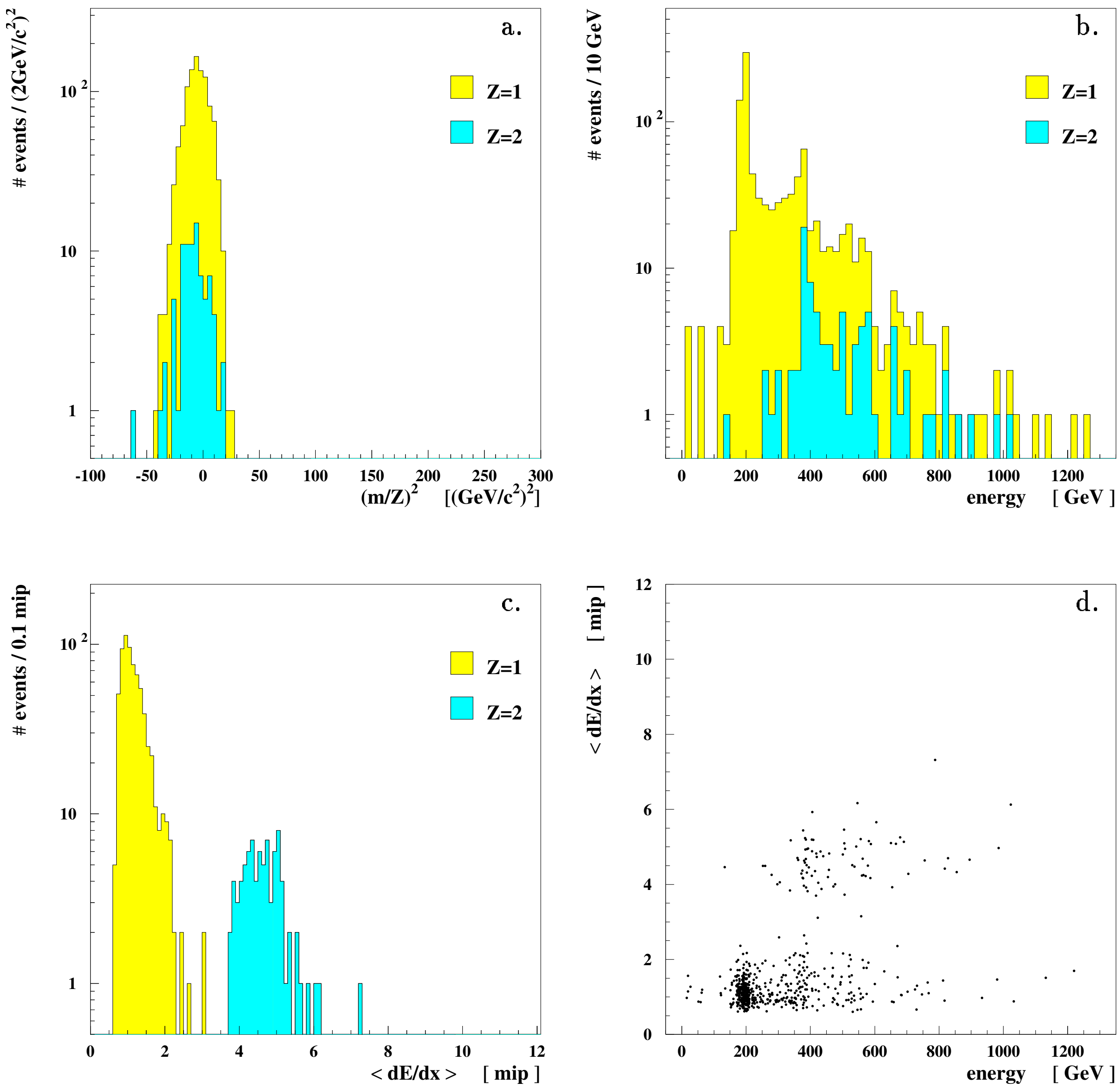

Figure 7.6: Distributions at $+200\,\mathrm{GeV}/c$ after the cut "no light in Č1 and Č2". Singly and doubly charged events are remaining.
(a) $(m/Z)^2$ distribution.
(b) Energy E seen by the hadron calorimeter.
(c) Energy loss measurement $\langle \mathrm{d}E/\mathrm{d}x \rangle$ in the scintillation counters.
(d) Correlation between E and $\langle \mathrm{d}E/\mathrm{d}x \rangle$.

two times higher and consequently the energy measurement yields values around 400 GeV. But further entries can be found were the energy is higher than expected from the charge measurement. All these events can be understood as being contaminated by additional particles, which contribute to the total energy seen by the calorimeter.

Chapter 8

Limits of the strangelet production

The investigated statistics of lead-lead interactions allows to give upper limits of the production of strangelets in Pb – Pb collisions..

8.1 Invariant differential production cross section

Independent of any production model one can give a simple upper limit in terms of the invariant differential production cross section.

Under the differential cross section for strangelets one understands the amount of produced strangelets per momentum bin $\mathrm{d}p$, per solid angle $\mathrm{d}^2\Omega$, per incident lead ion and per target nucleus. By multiplying this expression with E/p^2 of the strangelet we get a differential cross section, which is Lorentz invariant.

$$\frac{E}{p^2}\frac{\mathrm{d}^3\sigma}{\mathrm{d}p\,\mathrm{d}^2\Omega} \equiv E\frac{\mathrm{d}^3\sigma}{\mathrm{d}p^3} \equiv \frac{1}{p_\perp}\frac{\mathrm{d}^3\sigma}{\mathrm{d}y\,\mathrm{d}p_\perp\,\mathrm{d}\phi} = \frac{E}{p^3}\cdot\frac{1}{\alpha\cdot\eta_{\mathrm{det}}}\cdot\frac{N_{\mathrm{obs}}}{N_{\mathrm{int}}}\cdot\frac{1}{n\cdot l_{\mathrm{target}}} \tag{8.1}$$

Here, N_{obs} strangelets per N_{int} lead-lead interactions have been observed within the acceptance α of the beam line, with an overall detection efficiency η_{det}; n and l_{target} are target density and length.

Since N_{obs} is equal to zero, one usually replaces it with the upper limit correspondingly to a certain confidence level. A commonly used value is a 90% confidence level, corresponding to $N_{\mathrm{obs}} < 2.3$. Besides this statistical treatment, the upper limit is also subject to systematic uncertainties like the beam line acceptance and the lead ion counting, which are neglected in this chapter.

The term α reflects the (geometrical) acceptance of the beam line; the term η_{det} counts for the detection efficiency. It includes losses of particles due to physical processes like interactions in the detector material (η_{had}), efficiencies of the detector system itself (η_{trig}), and the reconstruction efficiency (η_{rec}) of the recorded events. Since the hadronic interactions of strangelets are not known the values obtained for protons are chosen tentatively (*cf.* appendix A and [Volken94]). A typical nuclear density is $10^{14}\,\mathrm{g/cm^3}$ or $100\,\mathrm{MeV/fm^3}$ and the radius of nuclei scales like $r = 1.3\,\mathrm{fm}\cdot A^{1/3}$. Strangelets should have larger densities and as a consequence smaller radii. The size of light strangelets might be similar to that of protons and as a consequence they should have similar interaction lengths.

Table 8.1: Strangelet summary

p/Z	N_{int}	α	η_{det}		$E\frac{d^3\sigma}{dp^3}\Big\vert_{p_\perp=0}^{\text{U.L.}(90\%)}$	t_{lab}	m_{limit}	Z
[GeV/c]	[10^{11}]	[10^{-8}]	$\eta_{\text{rec}\cdot\text{trig}}$	η_{had}	$\left[10^{-7}\frac{\text{barn}}{\text{GeV}^2}c^3\right]$	[μs]	[GeV/c^2]	
-100	1.1	4.0	0.95	0.73	5.7	≥ 1.2	4	-1
-200	1.2	4.1	0.95	0.73	1.3	≥ 1.2	8	-1
$+100$	2.1	4.0	0.95	0.73	3.0	≥ 1.2	3	$+1$
					0.7		4	$+2$
$+200$	1.1	4.0	0.90	0.66	1.7	≥ 1.7	6	$+1$
					0.4		9	$+2$

In Tab. 8.1 the achieved upper limits are summarized assuming stable strangelets with the lifetime limit t_{lab} based on the chosen trigger requirement.

The cross sections have been calculated for light strangelets. The invariant cross sections for heavy strangelets increase slightly to higher values according to the scale factor E/p^3. For multiply charged strangelets the cross sections have to be scaled by $1/Z^2$.

If a certain strangelet species would have a mean lifetime $\gamma\tau$ comparable to or even smaller than $t_{\text{lab}} = 1.2\,\mu$s or $1.7\,\mu$s, respectively, one would observe a corresponding smaller fraction and thus, one would have to multiply the upper limits by an additional factor $\exp(t_{\text{lab}}/\gamma\tau)$.

8.2 Total production cross section

A different way to parameterize the achieved result of the experiment is to compare an assumed total production cross section for strangelets with the total inelastic cross section of the colliding nuclei. The quotient of both cross sections is usually called the *sensitivity* for the experiment to observe a rare particle species and defines an upper limit for the production probability.

To calculate the sensitivity one assumes a certain parameterization of the production cross section and asks which fraction of strangelets would then fall into the acceptance of the experiment.

Commonly used production cross sections for heavy particles are described in terms of their transverse momentum and rapidity dependence. It is assumed that the $p_\perp$ dependence is like an exponential while the y dependence is Gaussian around the central rapidity y_{cm} of the colliding nuclei system [Crawford92]

$$\frac{1}{\sigma_{\text{prod}}}\frac{d^2\sigma_{\text{prod}}}{dy\,dp_\perp} = \frac{4p_\perp}{\langle p_\perp\rangle^2}\exp\left(-\frac{2p_\perp}{\langle p_\perp\rangle}\right)\frac{1}{\sqrt{2\pi}\sigma_y}\exp\left(-\frac{(y-y_{\text{cm}})^2}{2\sigma_y^2}\right) \tag{8.2}$$

with $y_{\text{cm}} = 2.9$ for Pb$-$Pb interactions at $p_{\text{lab}} = 158{\cdot}A\,\text{GeV}/c$, $\sigma_y = 0.5$ the width of the rapidity distribution and $\langle p_\perp\rangle = a\sqrt{m}\,\text{GeV}$ the mean transverse momentum, where a is a further variable, here set to 0.1, assuming that strangelets should be produced with a rather low transverse momentum [Pretzl95].

Furthermore, the known transmission[1] $T(y, p_\perp)$ of a particle with rapidity y and transverse momentum $p_\perp$ in the beam line determines the relative fraction of observed particles in the experiment for the assumed production cross section:

$$f_{\langle p_\perp\rangle,\sigma_y}(m) = \int\int T(y,p_\perp)\frac{1}{\sigma_{\text{prod}}}\frac{\mathrm{d}^2\sigma_{\text{prod}}}{\mathrm{d}y\mathrm{d}p_\perp}\mathrm{d}y\mathrm{d}p_\perp \tag{8.3}$$

Thereafter, the sensitivity $S(m)$ for observing a strangelet per interaction can be determined via

$$S(m) = \frac{1}{N_{\text{int}}\cdot f_{\langle p_\perp\rangle,\sigma_y}(m)\cdot\eta_{\text{det}}} = \frac{\sigma_{\text{prod}}}{\sigma_{\text{Pb-Pb}}} \tag{8.4}$$

for the accumulated statistics N_{int} with an achieved detection efficiency η_{det}. Fig. 8.1 shows the resulting sensitivity curves for singly charged strangelets within this production model for the four different rigidity settings.

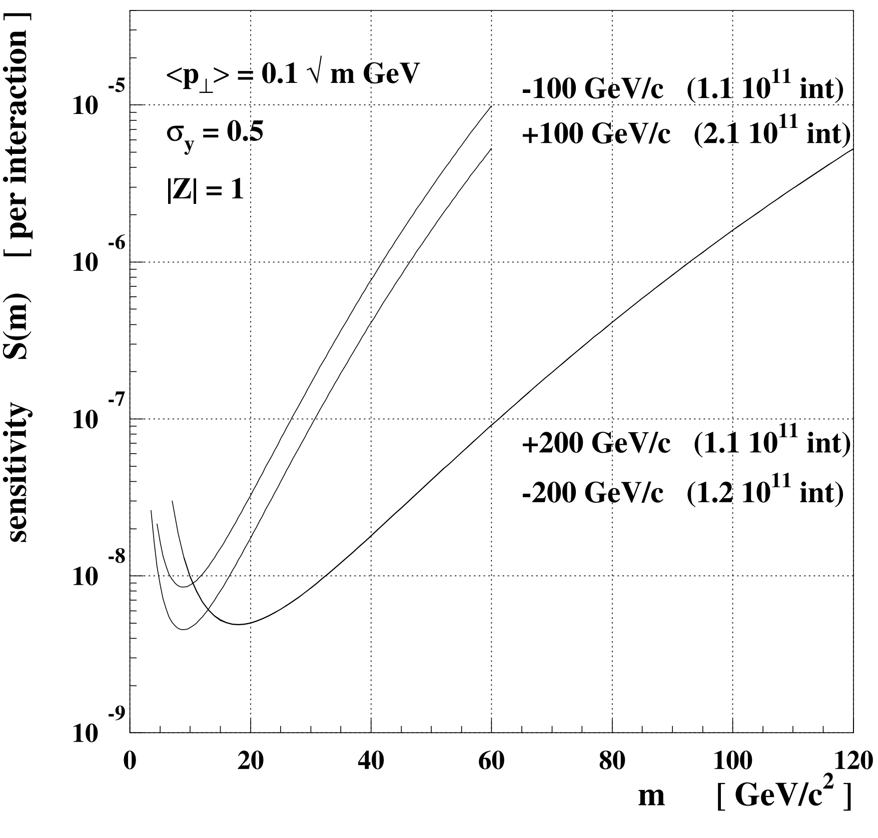

Figure 8.1: Obtained sensitivities for the production of strangelets.

The shape of the curves is determined by the Gaussian rapidity distribution while the absolute values strongly depend on the mean transverse momentum and its model parameter a. A short discussion on the consequences by varying a between 0 and 0.5 follows in section 8.4.

[1]The values of the transmission have been obtained from the TURTLE simulation, as described in section 3.2.2, and transformed from angle and momentum variables to rapidity and transverse momentum.

For charged strangelets $|Z| > 1$ the axis labeling of Fig. 8.1 can be replaced by $m/|Z|$ and $|Z| \cdot$ sensitivity, respectively, without changing significantly the curves themselves. For charges $|Z| > 1$ one should notice that the mass limits $m/|Z|$ become smaller and thus, the sensitivity lines could be extrapolated towards $m/|Z| \to 0$.

8.3 Upper production limit

The data taken in the two different kinematic regions of 100 and 200 GeV/c can be joined to a common upper production limit by adding the individual sensitivities via

$$\frac{1}{\text{upper limit production probability}} = \frac{1}{S_{100\,\mathrm{GeV}/c}} + \frac{1}{S_{200\,\mathrm{GeV}/c}} \tag{8.5}$$

Fig. 8.2 shows the resulting curves for $Z < 0$ and $Z > 0$.

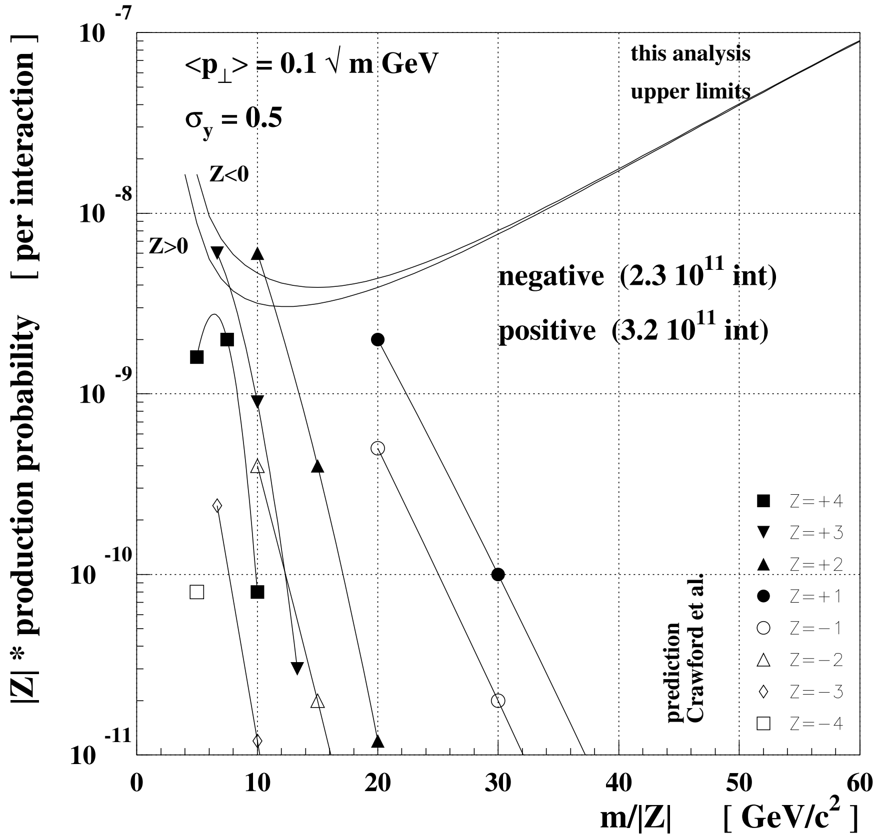

Figure 8.2: Upper limit of the production probability of strangelets achieved by this analysis and comparison with predictions [Crawford93].

For a comparison a few predicted production probabilities for positively and negatively charged strangelets, as given by Crawford *et al.* and discussed in section 1.4, are also marked in Fig. 8.2. Remarkable is that according to the prediction and to the assumed phase space distribution with $a = 0.1$ the sensitivity for detecting a positively, doubly charged strangelet with $m \approx 20\,\mathrm{GeV}/c^2$ (marked as a filled $\triangle$) has already been reached.

8.4 Consequences of variations in $\langle p_\perp \rangle$

As already mentioned above the experimental result in terms of an absolute upper production probability depends on the assumed phase space distribution. Its exact form is unknown. By changing the mean transverse momentum $\langle p_\perp \rangle$ from larger to smaller values one can easily improve the experimental sensitivity. This is shown for three choices of $a = 0.5$, 0.1 and 0 in Fig. 8.3 where the predictions of Crawford *et al.* are marked for comparison.

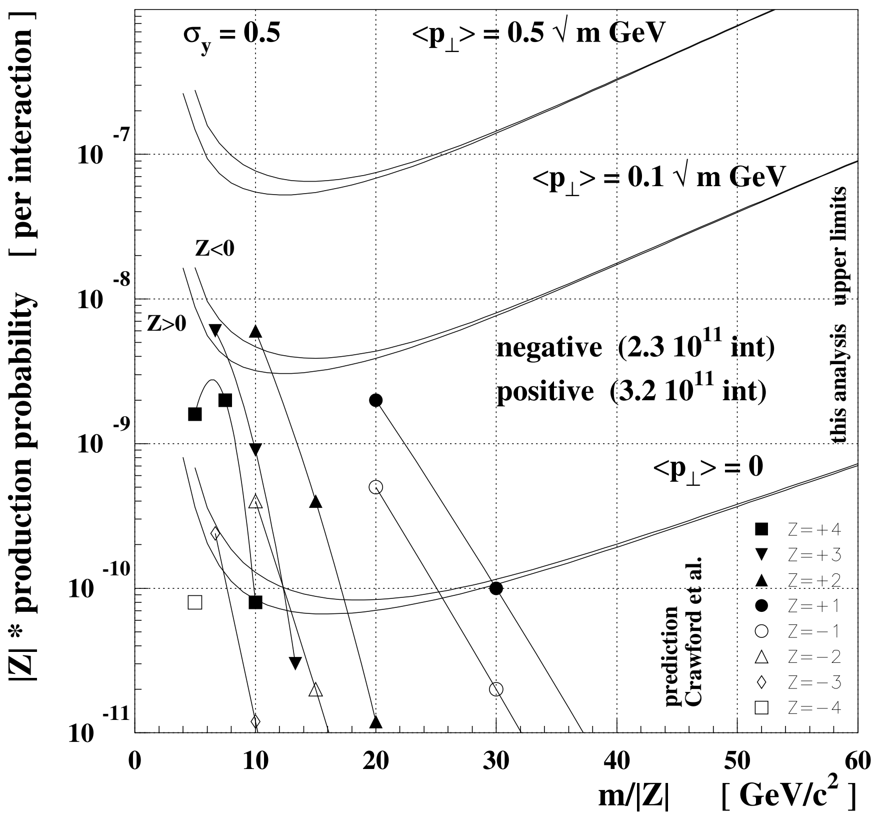

Figure 8.3: The experimental upper limit on the production probability of strangelets for three $\langle p_\perp \rangle$ values.

The increase of the mean transverse momenta with the mass of the particle was observed already on the data of mesons, nucleons and hyperons resulting from p-p collisions and interpreted on the basis of statistical theory of multiple particle production [Imaeda67]. Later the data of oxygen-gold collisions at $200 \cdot A\,\mathrm{GeV}/c$ confirmed that also in heavy ion collisions the mean transverse momenta increase with the mass of the produced particle: *e. g.* $\langle p_\perp \rangle = 0.5\,\mathrm{GeV}/c$ for protons and $0.8\,\mathrm{GeV}/c$ for lambdas [Harris89]. Thus, values $a = 0.5 \ldots 0.7$ are favoured in the parameterization $\langle p_\perp \rangle = a\sqrt{m}\,\mathrm{GeV}$.

In a thermodynamic interpretation the mean transverse momenta scale with the temperature of the system and the production of mesons and baryons takes place at $kT = 100$ to 200 MeV. If one regards strangelets as remnants of a cooled quark-gluon plasma (*cf.* section 1.3.2), it is reasonable to assume lower temperatures and therefore lower transverse momenta likewise.

The lowest limit is $\langle p_\perp \rangle = 0$. At this point the finite angular opening of the beam line spectrometer does not limit the acceptance of strangelets and thus the experiment gets the best sensitivity.

Outlook

Besides the search for strangelets as a signature for a quark-gluon plasma formation, the production rates of antiparticles can be used to investigate the spacetime evolution of the heavy ion interaction [Heinz86, Gavin90].

The presented analysis of data taken at -100 and $-200\,\mathrm{GeV}/c$ delivered quantitative production rates of antiprotons and antideuterons at forward rapidities. Much higher production rates have been found near midrapidity by analyzing low rigidity spectra of -20 and $-40\,\mathrm{GeV}/c$. These have been investigated thoroughly by F. Stoffel [Stoffel96].

The recent result on production rates of antiprotons and antideuterons are displayed as a function of rapidity in Fig. 8.4, which combines the analysis of low and high rigidity settings.

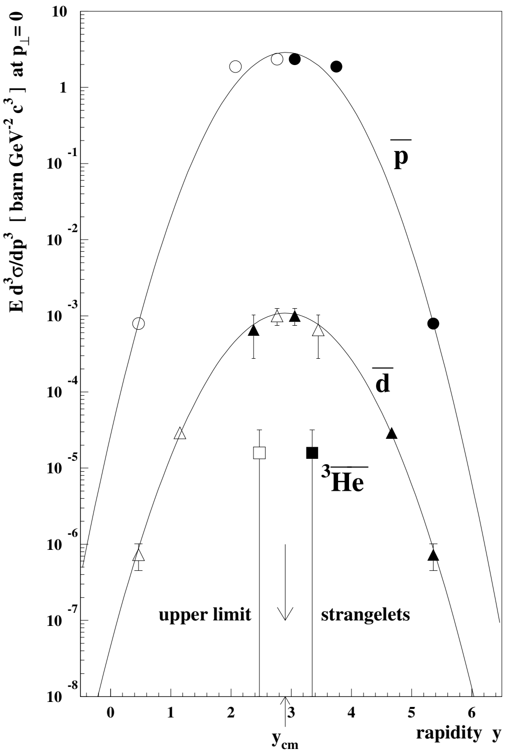

Figure 8.4: Invariant antiparticle production cross sections. The open symbols are data points reflected at midrapidity $y_{\mathrm{cm}} = 2.9$. Only statistical errors are drawn. The lines show fits of Gaussian functions through the measured data points while the mean is fixed to midrapidity. The width of the distribution is in both cases ≈ 0.6 units of rapidity. One antihelium-3 in 10^{10} interactions has been found at $-20\,\mathrm{GeV}/c$.

As a comparison in this diagram the upper limit of the production probability for singly charged strangelets is on a level of $10^{-7}\frac{\mathrm{barn}}{\mathrm{GeV}^2}c^3$.

In the meantime additional data from Pb$-$Pb interactions at $-200\,\mathrm{GeV}/c$ with more than one order of magnitude more statistics has been recorded to continue the strangelet search. Furthermore, it is planned to increase the statistics at the positive polarity in a forthcoming data taking period, too.

Appendix A

Absorption of particles in the target and in the beam line

One necessary correction to the observed raw particle yield is based on the fact, that part of the secondary particles are absorbed in the material present in the beam line, like the detector material. The use of a relative thick production target introduces a reduction of the incident lead ion flux and a finite reabsorption probability of produced secondaries within the target.

The formalism to calculate absorption probabilities, the sources of absorption measurements and resulting estimates relevant for the NA52 setup are summarized.

A.1 Calculation formalism

If y_1 and y_2 are the particle yields of the primary and of one species of a secondary particle, respectively, σ_2 the production cross section for the secondary species, $\sigma_{\overline{1}}$ and $\sigma_{\overline{2}}$ the absorption cross sections, λ_i the corresponding reaction lengths $\lambda_i = 1/(n\sigma_i)$ in the target with atomic density n, and z the depth in the target, the particle yields are related by the following set of linear differential equations

$$\frac{\mathrm{d}y_1}{\mathrm{d}z} = -\frac{y_1}{\lambda_{\overline{1}}} \tag{A.1}$$

$$\frac{\mathrm{d}y_2}{\mathrm{d}z} = \frac{y_1}{\lambda_2} - \frac{y_2}{\lambda_{\overline{2}}} \tag{A.2}$$

where the first equation accounts for the reduction of the primary beam, while the second equation describes *birth* and *death* of the secondary particles within the target.

The solution allows to determine the production cross section σ_2 via

$$\sigma_2 = \frac{y_2(z)}{y_1(0)} \cdot \frac{\sigma_{\overline{1}} - \sigma_{\overline{2}}}{\exp(-n\sigma_{\overline{2}}z) - \exp(-n\sigma_{\overline{1}}z)} \tag{A.3}$$

for an incident particle yield $y_1(0)$ in front of the target and the secondary particle yield $y_2(z)$ behind the target of length z, if one knows the absorption cross sections.

Eq. (A.3) can be compared with the ansatz

$$\sigma_2 = \frac{y_2(z)}{y_1(0) - y_1(z)} \cdot \frac{1}{n \cdot z} \cdot \eta_{\mathrm{had}}^{\mathrm{target}} \tag{A.4}$$

where the secondary particle yield $y_2(z)$ is normalized to the number of primary interactions $y_1(0) - y_1(z) = y_1(0)\,(1 - \exp(-n\sigma_{\bar{1}}z))$ in the target. The hadronic transmission probability for secondaries in the target can be identified as

$$\eta_{\mathrm{had}}^{\mathrm{target}} = \frac{\exp(-n\sigma_{\bar{2}}z) - \exp(-n\sigma_{\bar{1}}z)}{n \cdot z\,(\sigma_{\bar{1}} - \sigma_{\bar{2}})\,(1 - \exp -n\sigma_{\bar{1}}z)} \tag{A.5}$$

A further correction for the calculation of the true cross section is the absorption of secondary particles in the material placed behind the target. Its calculation is straight forward. Here, the transmission is

$$\eta_{\mathrm{had}}^{\mathrm{beam\,line}} = \exp -n\sigma_{\bar{2}}z \tag{A.6}$$

A.2 Cross sections

For the determination of the (absorption) cross sections the data base of the simulation programme GEANT is broached [GEANT93]. For the calculation of the collision cross section of light hadrons π, K and p it uses a parameterization of the form

$$\sigma = \sigma_0 A^{\alpha} \tag{A.7}$$

while the interaction of heavier nuclei like deuterons, tritons, helium-3 and helium-4 are parameterized via

$$\sigma = 49\,\mathrm{mbarn} \cdot \left(A^{\frac{1}{3}} + B^{\frac{1}{3}}\right)^2 \tag{A.8}$$

A and B are the mass numbers of projectile and target, respectively. Such parameterizations are based on absorption measurements for light particles, see [Carroll79], measurements of total cross sections of neutrons, see [Murthy75] and of heavy ions, see [Bamberger88, Barnes88, Anderson89], at high momenta on different targets. The absorption of lead in lead itself is based on the extrapolation of the formula

$$\begin{aligned} \sigma &= \sigma_0 \cdot \left(A^{\frac{1}{3}} + B^{\frac{1}{3}} - \delta\right)^2 \\ \text{with} \quad & \sigma_0 = (75 \pm 15)\,\mathrm{mbarn}, \quad \delta = 1.4 \pm 0.7 \end{aligned} \tag{A.9}$$

which is a fit to data of ^{32}S interactions with various targets between beryllium and lead [Anderson89]. It yields a nuclear interaction length of 4 cm in Pb$-$Pb collisions, a value which is consistently used in this analysis for the transformation of the amount of incident lead ions to the number of interactions.

A.3 Total absorptions

Besides the lead target itself the most important material types contributing to losses due to hadronic interactions in the beam line are the scintillator of the TOF hodoscopes TOF1-5 and trigger counters B1 and B2, 10 m nitrogen gas in the threshold counters at high pressures ($\mathcal{P} \gtrsim 0.5$ bar), 6 m helium gas in the CEDAR (at $\mathcal{P} \gtrsim 11$ bar), 7 m air and numerous vacuum windows. A detailed summing up of all material components yields the collision probabilities for protons, deuterons and light nuclei in the NA52 detector as listed in Tab. A.1.

Table A.1: Collision probabilities in the NA52 detector[1]

particle	$1-\eta_{\mathrm{had}}^{\mathrm{target}}$ l_{target}		$1-\eta_{\mathrm{had}}^{\mathrm{beam\,line}}$ beam line	
	16 mm	40 mm	up to TOF3	up to TOF5
p	0.083	0.219	0.070	0.156
d	0.068	0.183	0.146	0.312
t/^{3}He	0.071	0.192	0.160	0.342
^{4}He	0.074	0.210	0.182	0.380

The interactions of strangelets are not known, therefore the values obtained for protons are taken. For the different target and trigger settings the integrated absorptions are shown in Tab. A.2. $\eta_{\mathrm{had}} = \eta_{\mathrm{had}}^{\mathrm{target}} \cdot \eta_{\mathrm{had}}^{\mathrm{beamline}}$ is the hadronic transmission probability for a particle.

Table A.2: Collision probability for protons[1]

p/Z	l_{target}	beam line	total absorption	η_{had}
+200 GeV/c	16 mm	up to TOF5	$0.083 \oplus 0.156 = 0.226$	0.774
+100 GeV/c	40 mm	up to TOF3	$0.219 \oplus 0.070 = 0.274$	0.726
−200 GeV/c	40 mm	up to TOF3	$0.219 \oplus 0.070 = 0.274$	0.726
−100 GeV/c	40 mm	up to TOF3	$0.219 \oplus 0.070 = 0.274$	0.726

For the settings at negative rigidity the total absorptions of light antinuclei are summarized in Tab. A.3. Always a 40 mm thick lead target is taken.

Table A.3: Collision probability of light (anti)nuclei[1]

particle	beam line			
	up to TOF3		up to TOF5	
	total absorption	η_{had}	total absorption	η_{had}
$\overline{\mathrm{p}}$	$0.219 \oplus 0.070 = 0.274$	0.726	$0.219 \oplus 0.156 = 0.341$	0.659
$\overline{\mathrm{d}}$	$0.183 \oplus 0.146 = 0.302$	0.698	$0.183 \oplus 0.312 = 0.438$	0.562
$\overline{\mathrm{t}}/\overline{^3\mathrm{He}}$	$0.192 \oplus 0.160 = 0.321$	0.679	$0.192 \oplus 0.342 = 0.468$	0.532
$\overline{^4\mathrm{He}}$	$0.210 \oplus 0.182 = 0.354$	0.646	$0.210 \oplus 0.380 = 0.510$	0.490

Practically the numbers have been derived by using the data base of the detector and simulation tool GEANT [GEANT93].

[1]Private communication from F. Stoffel, University of Bern.

Bibliography

[Agostini89] G. D'Agostini *et al.* (The ZEUS Calorimeter Group); Experimental study of uranium plastic scintillator calorimeters ; NIM **A274** 134.

[Anderson89] E. Anderson *et al.*; A measurement of cross sections for ^{32}S interactions with Al, Fe, Cu, Ag and Pb at 200 GeV/c per nucleon; Phys. Lett. **B220** (1989) 328.

[Baltz95] A. J. Baltz *et al.*; Strange cluster formation in relativistic heavy ion collisions; Phys. Lett. **B325** (1994) 7-12.

[Bamberger88] A. Bamberger *et al.*; Charged particle multiplicities and inelastic cross sections in high energy nuclear collisions; Phys. Lett. **B205** (1988) 583.

[Barnes88] P. D. Barnes *et al.*; A measurement of cross sections for ^{16}O Al and ^{16}O Pb interactions at 60 and 200 GeV/c per nucleon; Phys. Lett. **B206** (1988) 146.

[Barrette90] J. Barrette *et al.*; Search for strange quark matter in high-energy heavy-ion collisions; Phys. Lett. **B252** (1990) 550.

[Beavis95] D. Beavis *et al.*; Search for new metastable particles produced in Au+Au Collisions at 10.8$\cdot A$ GeV/c; Phys. Rev. Lett. **75** (1975) 3078.

[Berger87] M. S. Berger and R. L. Jaffe; Radioactivity in strange quark matter; Phys. Rev. **C35** (1987) 213.

[Bjorken79] J. D. Bjorken and L. D. McLerran; Explosive quark matter and the "Centauro" event; Phys. Rev. **D20** (1979) 2353.

[Blas95] F. Blas *et al.*; Acceleration of lead ions in then CERN PS booster and the CERN PS; CERN/PS 95-27 (HI).

[Bodmer71] A. R. Bodmer; Collapsed nuclei; Phys. Rev. **D4** (1971) 1601.

[Borer94] K. Borer *et al.*; Strangelet search in S-W collisions at 200$\cdot A$ GeV/c; Phys. Rev. Lett. **72** (1994) 1415.

[Bovet82] C. Bovet *et al.*; The CEDAR counters for particle identification in the SPS secondary beams: A description and an operation manual; CERN yellow report, CERN 82-13, SPS Division (1982).

[Brown74] K. L. Brown and Ch. Iselin; Decay TURTLE, a computer program for simulating charged particle beam transport systems, including decay calculations; CERN report, CERN-74-2, 5 February 1974.

[Brown80] K. L. Brown, D. C. Carey, Ch. Iselin and F. Rothacker; TRANSPORT, a computer program for designing charged particle beam transport systems; CERN yellow report, CERN 80-04, SPS Division, 18 March 1980.

[Carey95] D. C. Carey, K. L. Brown and F. Rothacker; Third order TRANSPORT, a computer program for designing charged particle beam transport systems; SLAC-R-95-462 (1995).

[Carroll79] A. S. Carroll *et al.*; Absorption cross section of $\pi^{\pm}$, $K^{\pm}$, p and $\overline{p}$ on nuclei between 60 and 280 GeV/c; Phys. Lett **80B** (1979) 319.

[Chen94] T.Y. Chen; Application of maximum likelihood method in reconstruction of charged particle tracks ; High Energy Phys. and Nucl. Phys. **18** (1994) 10.

[Chin79] S. A. Chin and A. K. Kerman; Possible long-lived hyperstrange multiquark droplets; Phys. Rev. Lett. **43** (1979) 1292.

[Crawford91] H. Crawford *et al.*; Search for new negative particles produced in 14.6·A GeV/c Si+A interactions; Nucl. Phys. B (Proc. Suppl.) **24B** (1991) 251.

[Crawford92] H. Crawford, M. Desai and G. Shaw; Production and detection of drops of strange matter; Phys. Rev. **D45** (1992) 857.

[Crawford93] H. Crawford, M. Desai and G. Shaw; Prediction of enhanced production of strange matter at CERN SPS; Phys. Rev. **D48** (1993) 4474.

[DeGrand75] T. DeGrand, R. L. Jaffe, K. Johnson and J. Kiskis; Masses and other parameters of the light hadrons; Phys. Rev. **D12** (1975) 2060.

[Dittus95] F. Dittus *et al.*; First look at NA52 data on Pb-Pb interactions at 158 GeV/c per nucleon; Nucl. Phys. **A590** (1995) 347c.

[Farhi84] E. Farhi and R. L. Jaffe; Strange matter; Phys. Rev. **D30** (1984) 2379.

[Faugier95] A. Faugier *et al.*; The SPS as accelerator of Pb^{82+} ions; 1995 Particle Accelerator Conference, Dallas, USA, 30 April - 5 May 1995.

[Gavin90] S. Gavin, M. Gyulassy, M. Plümer and R. Venugopalan; Antiproton production as a baryonometer in ultrarelativistic heavy ion collisions; Phys. Lett. **B234** (1990) 175.

[GEANT93] GEANT; Detector and simulation tool; CERN program library long write up W5013, Geneva, June 1993.

[Gilson93] E. P. Gilson and R. L. Jaffe; Stability of very small strangelets; Phys. Rev. Lett. **71** (1993) 332.

[Greiner87] C. Greiner, P. Koch, and H. Stöcker; Separation of strangeness from antistrangeness in the phase transition from quark to hadron matter: Possible formation of strange quark matter in heavy-ion collisions; Phys. Rev. Lett. **58** (1987) 1825.

[Greiner88] C. Greiner, D. Rischke, H. Stöcker and P. Koch; Emission of droplets of strange quark matter in RHIC; Z. Phys. **C38** (1988) 283.

[Greiner88a] C. Greiner, D. Rischke, H. Stöcker and P. Koch; Creation of strange-quark-matter droplets as a unique signature for quark-gluon-plasma formation in relativistic heavy-ion collisions; Phys. Rev. **D38** (1988) 2797.

[Greiner91] C. Greiner and H. Stöcker; Distillation and survival of strange-quark-matter droplets in ultrarelativistic heavy-ion collisions; Phys. Rev. **D44** (1991) 3517.

[Gutbrod91] H. Gutbrod and H. Stöcker; The nuclear equation of state; Scientific American, November 1991.

[Harris89] J. W. Harris *et al.*; Recent results from the NA35 collaboration at CERN; Nucl. Phys. **A498** (1989) 133c-150c.

[Hasenroth95] H. D. Hasenroth; The CERN heavy ion acceleration facility; CERN/PS 95-26 (HI).

[Heinz86] U. Heinz, P. R. Subramanian, H. Stöcker and W. Greiner; Formation of anti matter clusters in the hadronic phase transition; J. Phys. **G12** (1986) 1237.

[Hess96] P. Hess; Diploma thesis in preparation; University of Bern, 1996.

[Imaeda67] K. Imaeda; Transverse-momentum distribution of secondaries from high-energy nuclear interactions and interpretation by means of a statistical model; Il Nuovo Cimento **A48** (1967).

[Klingenberg92] R. Klingenberg; Aufbau eines Meßstandes zur Charakterisierung von Siliziumdioden und Analyse von Teststrahldaten eines Uran-Szintillator-Kalorimeters; Diploma thesis, University of Dortmund, 1992.

[Koch91] P. Koch; Weak decays of small meta-stable strangelets; Nucl. Phys. B (Proc. Suppl.) **24B** (1991) 255-259.

[Kumar95] B. S. Kumar; Rapidity distributions of Antiprotons in Si+A and Au+A collisions; Nucl. Phys. **A566** (1994) 439c.

[Lindén96] T. Lindén; Ph.D. thesis in preparation; University of Helsinki, 1996.

[Liu84] H.-C. Liu, and G. L. Shaw; Production and detection of metastable strange-quark droplets in heavy-ion collisions; Phys. Rev. **D30** (1984) 1137.

[Lynch91] G. R. Lynch and O. I. Dahl; Approximations to multiple Coulomb scattering; NIM **B58** (1991) 6.

[Molière47] G. Molière; Theorie der Streuung schneller geladener Teilchen; Teil I: Einzelstreuung am abgeschirmten Coulomb-Feld; Z. Naturforschg. **2a** (1947) 133; Teil II: Mehrfach- und Vielfachstreuung; Z. Naturforschg. **3a** (1948) 78.

[Murthy75] P. V. R. Murthy *et al.*; Neutron total cross sections on nuclei at Fermilab energies; Nucl. Phys. **B92** (1975) 269-308.

[PDG94] Particle Data Group; Review of particle properties; Phys. Rev. **D50** (1994).

[Pretzl95] K. Pretzl *et al.*; Search for strange quark matter in relativistic heavy ion collisions at CERN (NA52); Proceedings of the International Symposium on Strangeness and Quark Matter, Crete, Hellas, Sept. 1-5, 1994, World Scientific 1995, pp. 230-244.

[Regler78] M. Regler; Vielfachstreuung in der Ausgleichsrechnung; Acta Physica Austriaca **49** (1978) 37.

[Rotondo91] F. S. Rotondo *et al.*; Search for strange matter in heavy ion collisions at Brookhaven's AGS; Nucl. Phys. B (Proc. Suppl.) **24B** (1991) 265.

[Rotondo95] F. S. Rotondo; Search for strange quark matter in heavy ion collisions at Brookhaven's AGS; AIP conf. proc. **340** (1995) 16.

[Saito90] T. Saito *et al.*; Is there strange-quark matter in galactic cosmic rays?; Phys. Rev. Lett. **65** (1990) 2094.

[Stefanini91] G. Stefanini; Electro-optic intensity modulators in front ends at future Colliders; presented at the 18th Eloisatron Workshop, Erice, 13-19 Nov. 1991.

[Stoffel92] F. Stoffel; Studie zur Flugzeitmessung mit hadronischen Schauern; Diploma thesis, University of Bern, 1992.

[Stoffel96] F. Stoffel; Ph.D. thesis in preparation; University of Bern, 1996.

[Volken94] W. Volken; Strangelet search in S-W collisions at $200{\cdot}A\,\mathrm{GeV}/c$; Ph.D. thesis, University of Bern, 1994.

[Witten84] E. Witten; Cosmic separation of phases; Phys. Rev. **D84** (1984) 272.

Acknowledgments

I am grateful to all colleagues of the Laboratory for High Energy Physics and all collaborators of the NEWMASS experiment for their kindly support and providing a friendly and stimulating atmosphere.

Especially I would like to thank:

Prof. Klaus Pretzl for offering me the possibility to join the NEWMASS experiment.

Kurt Borer, Emmanual Kling, Giorgio Stefanini, and Francois Vasey for their cooperation and help with the optical transmission system.

Koni Elsener, Jean-Paul Guillaud and Tomas Lindén for their explanations and discussions about the beam line spectrometer.

Dani Frei, Patrick Hess, Edwin Hugentobler, Urs Moser, Werner Volken and Qiuping Zhang for their helpfulness and valuable discussions.

Fido Dittus and Franziskus Stoffel for their creative criticism and friendly team-work.

Curriculum vitae

	Reiner Klingenberg
birthday	July 13th, 1965
birth-place	Bremen, FR Germany
nationality	German
marital status	unmarried
parents	Wilma Klingenberg, née Kuntze Karlheinz Klingenberg
August 1972 – July 1976	primary school Langeloh-Grundschule, Dortmund
August 1976 – May 1985	secondary school Helene-Lange-Gymnasium, Dortmund
May 1985	matriculation (Abitur)
July 1985 – September 1986	military service, Hannover
October 1986 – March 1992	study at the University of Dortmund subject: physics
September 1988	intermediate examination
October 1990 – March 1992	diploma thesis at the chair Experimental Physics IV supervised by Prof. Dr. C. Gößling
March 1992	leaving examination as graduated physicist (Diplom-Physiker)
since April 1992	University of Bern Ph.D. student at the Laboratory for High Energy Physics supervised by Prof. Dr. K. Pretzl